MEASUREMENT AND ANALYSIS OF WIRE SAWING INDUCED RESIDUAL STRESS IN PHOTOVOLTAIC SILICON WAFERS

A Thesis
Presented to
The Academic Faculty

by

Vanessa Pogue

In Partial Fulfillment
of the Requirements for the Degree
Master in Science in the
School of Mechanical Engineering

Georgia Institute of Technology
May 2016

MEASUREMENT AND ANALYSIS OF WIRE SAWING INDUCED RESIDUAL STRESS IN PHOTOVOLTAIC SILICON WAFERS

Approved by:

Dr. Shreyes Melkote, Advisor
School of Mechanical Engineering
Georgia Institute of Technology

Dr. Steven Danyluk
School of Mechanical Engineering
Georgia Institute of Technology

Dr. Ajeet Rohatgi
School of Electrical and Computer Engineering
Georgia Institute of Technology

Date Approved: March 28th, 2016

This thesis is dedicated to my grandfather,
Lee McCulley

ACKNOWLEDGEMENTS

I would first like to express my sincere gratitude to my adviser, Dr. Shreyes Melkote for his continued support of the research necessary for this thesis. I also would like to acknowledge and thank the other members of my committee for their help and commitment: Dr. Steven Danyluk and Dr. Ajeet Rohatgi.

I am indebted to all of my lab and office mates, particularly Arkadeep Kumar for his help with my research and for many excellent conversations over countless topics. Special thanks go to Kevin Skenes and Guru Prasath for passing on their knowledge about the polariscope and photoelasticity project.

In addition, I would like to extend a special recognition to my parents, my friends, and my family for their love and support, and especially to Chris Sanders for scientific discussions, brainstorming and review of my work.

This thesis would not be possible without the financial and in-kind support of this work by the Silicon Solar Consortium (SiSoC), an Industry/University Cooperative Research Center. Surface roughness and 3D surface maps were collected with the help of the Advanced Technology Research Center (ARTC) in Singapore with the assistance and guidance of Dr. David Butler. Photoluminescence (PL) mapping was provided by Dr. Vijay Yelundur at Suniva, Inc in Norcross, Georgia. Additionally, Brian Rounsaville of the University Center of Excellence for Photovoltaic Research and Education (UCEP) in the School of Electrical and Computer Engineering at Georgia Tech was pivotal in providing assistance with the design of cleaning, etching, and high temperature annealing procedures for silicon wafers.

TABLE OF CONTENTS

LIST OF TABLES

Page

LIST OF FIGURES

Page

LIST OF SYMBOLS AND ABBREVIATIONS

Si	silicon
PV	photovoltaic
PL	photoluminescence
LAWS	loose abrasive slurry wire sawing
DWS	diamond wire sawing
CZ	Czochralski
mc-Si	multi-crystalline silicon
mono-Si	mono-crystalline silicon
SiC	silicon carbide
τ_{max}	maximum shear residual stress
HT anneal	high temperature anneal
MPa	megapascal
σ_1, σ_2	largest and smallest in-plane principle stresses
σ_{xx}, σ_{yy}	normal stresses in the x and y direction
τ_{xy}	shear stress in the xy plane
μm	micrometer
mm	millimeter
cm	centimeter
nm	nanometer
μPL	micro-photoluminescence
a.u.	arbitrary units

SUMMARY

Silicon (Si) wafers are used in over ninety percent of solar cells [1] and are the most important material for solar cell production today. As Silicon is a very brittle material, breakage during processing is a significant issue leading to lower production yields and also contributes to a large proportion of the overall solar cell manufacturing cost. The manufacturing process of a Si wafer comprises of first a high temperature heating process to produce a Si ingot from polycrystalline Silicon, which is then cut into bricks and subsequently sawn into wafers using a wire saw. These processes create residual stresses both from the thermal gradient induced by solidification and from either the rolling-indenting or scratching-indenting processes caused by the type of wire saw used. The objective of this research is to study silicon wafer residual stress as a result of the typical industry manufacturing processes and by doing so, better understand the mechanical properties that lead to increased fracture.

Specifically, this thesis aims to quantify the amount of residual stress generated by the solidification/thermal gradient produced during the casting of Si ingots separately from the residual stress generated by the wire sawing process. Samples from industry are used to compare the effects of the manufacturing processes on residual stress in multi-crystalline silicon (mc-Si) wafers including the effects of fixed abrasive diamond wire sawing (DWS) vs. loose abrasive (LAWS) slurry wire sawing used in the wafering process.

Near-infrared birefringence polariscopy and polarized micro-Raman spectroscopy are used to study wafer residual stresses within grains and at grain boundaries in mc-Si as

a function of etch-depth. While near-infrared birefringence polariscopy allows for the measurement of full-field maximum shear stress, micro-Raman spectroscopy provides decomposition of the stress tensor into both principal and shear in-plane stress components. Consequently, regions of high tensile stress, which are detrimental to the mechanical integrity of the wafer, can be easily identified.

The results of the research found that both wire sawing processes produce compressive residual stresses (in the as-cut mc-Si wafer surfaces). LAWS produces larger compressive stresses in the as-cut Si wafer surface layers than DWS. The thermal gradient/solidification residual stresses were found to be tensile in nature. The spatial distribution of the residual stress is studied both within grains and at grain boundaries to provide an understanding of the effect of manufacturing induced residual stress on Si wafer structure.

The two residual stress measurement techniques, near-infrared birefringence polariscopy, and micro-Raman spectroscopy, were compared both in terms of the fundamental physical principles on which they are based, and by the use of experiments. While the two residual stress measurement techniques cannot be compared directly, due to differences in spatial resolution, the results of this study confirmed that, on an order of magnitude basis, the two methods yield similar residual stress values when probing the same region of a wafer.

In addition to the mechanical characterization, the residual stress produced by the thermal gradient/solidification process for multi-crystalline Si wafers was also correlated to electrical performance of mc-Si wafers using photoluminescence. It was determined that a negative correlation exists between the maximum residual shear stress due to

casting/solidification and the photoluminescence of mc-Si wafers. In addition, an increase in tensile stress at the surface of mc-Si wafers as a result of high temperature annealing was found to improve photoluminescence.

CHAPTER 1
INTRODUCTION

1.1 Background: Manufacturing of Photovoltaic Silicon Wafers

Crystalline silicon (Si) continues to be the leading substrate used in solar cells today, comprising close to 85% of the world photovoltaic (PV) market [2]. Approximately 40-60% of the total manufacturing cost for a solar cell can be attributed to the manufacturing and material costs of the Si wafer [3]. Due to the high cost, Si wafers for PV applications are made as thin as possible to minimize material use but still absorb the full spectrum of sunlight radiation through the thickness. Silicon wafers are made to the standard size of 156 mm x 156 mm, with a thickness of approximately 180μm. In addition to its high manufacturing cost, Si is very brittle, and wafers are therefore prone to fracture during handling and processing.

The manufacturing process to create a Si wafer is illustrated schematically in Figure 1.1.

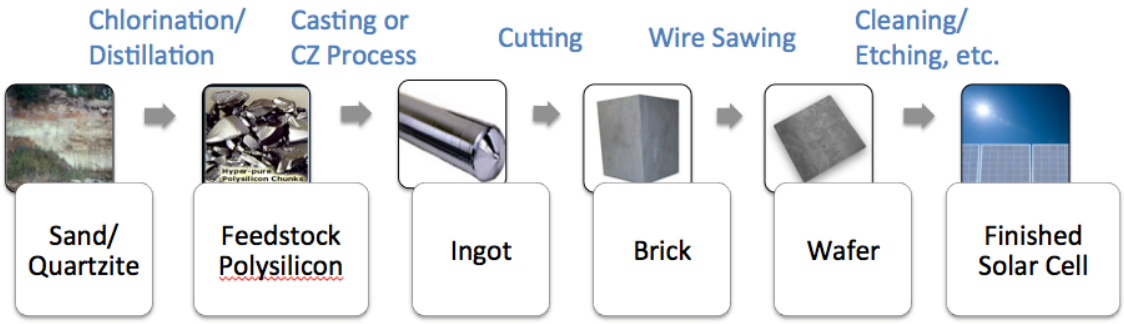

Figure 1.1: Manufacturing process for Si wafer
(Photos courtesy of VacSol GmbH and BYU [4, 5]).

First, polycrystalline Si feedstock is produced from sand, quartzite (SiO_2), and carbon by a high temperature purification process requiring several steps including chlorination and distillation. The feedstock polysilicon is then used to make an ingot. There are two traditional large-scale processes to produce the ingot. The most common process is casting, which is used to produce a multi-crystalline Si (mc-Si) ingot (see Figure 1.2).

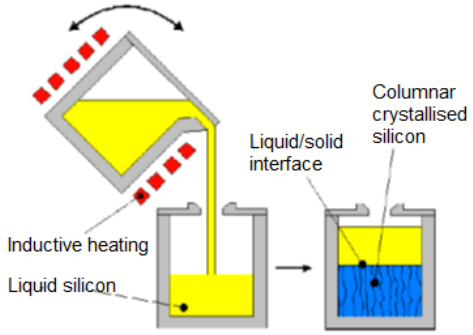

Figure 1.2: Casting of mc-Si ingot [6].

The polycrystalline Si feedstock is heated to 1450 °C and then poured into a crucible for solidification. The melt solidifies and columnar crystallized Si is formed. This method introduces impurities into the melt from contact with the crucible, especially close to the exterior or edges of the ingot. Typical crucible materials consist of fused silica (SiO_2) or graphite with a silicon nitride (Si_3N_4) coating. These materials can introduce elements of oxygen, nitrogen, and carbon. Remnant impurities in the crucible such as iron, chromium, and nickel also diffuse into the melt and solidify [3]. In addition to impurities, the resulting mc-Si ingot has many grain boundaries and dislocations that negatively influence the electrical performance of the finished photovoltaic Si solar cells [7].

The second most prevalent method for producing a Si ingot is the Czochralski (CZ) process, which is used to create a single crystal or mono-crystalline Si (mono-Si) ingot, shown in Figure 1.3.

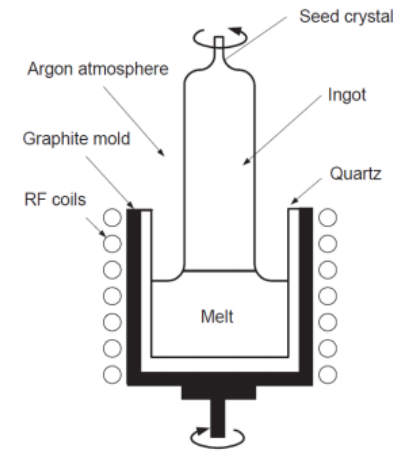

Figure 1.3: Czochralski process to create a Si ingot using a seed crystal [8].

In this case, a crucible is used to heat the polycrystalline Si feedstock and create molten Si. A precisely oriented "seed crystal" is then lowered into the Si melt. The seed crystal is simultaneously rotated and pulled out of the molten Si in an inert gas (Argon) atmosphere to control impurity introduction. By controlling the melt temperature, the pull-rate, and the speed of rotation of the seed crystal, a large single-crystal Si ingot is grown. Mono-Si has no grain boundaries, fewer impurities, and fewer dislocations in its crystal lattice compared to mc-Si. Solar cells made from CZ wafers result in higher electrical energy conversion efficiencies when compared to mc-Si solar cells; however, CZ wafers are on average 25-30% more expensive than mc-Si wafers [2].

Once the ingot is formed, it is cut into 156 mm x 156 mm square bricks, 25-26 cm long, depending on the length of the ingot. The bricks are sawn into approximately 180μm thick wafers using a wire sawing process. The traditional loose abrasive slurry wire sawing process is shown schematically in Figure 1.4.

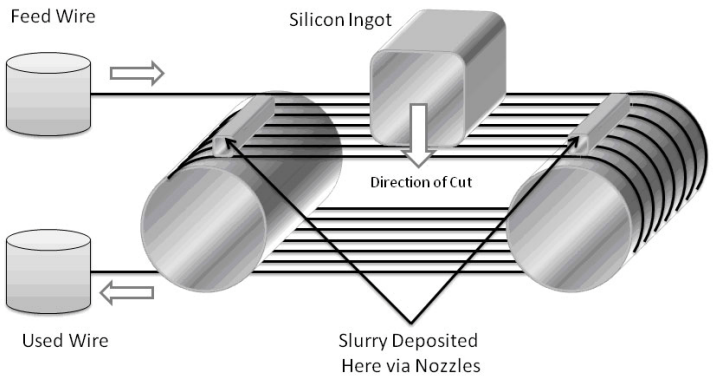

Figure 1.4: Wire sawing process, loose abrasive slurry (LAWS) [9].

A thin, long stainless steel wire, approximately 120-160μm in diameter is wrapped multiple times around either two or four large spools to create a web of cutting wires. The brick is then fed into the fast moving web of wires to yield wafers. Industry uses two different wire sawing methods to cut Si wafers. Traditionally, a loose abrasive slurry wire sawing (LAWS) process is used. In this process, a loose abrasive slurry of silicon carbide (SiC) particles entrained in polyethylene glycol is continually poured onto the wire during sawing. The abrasive grits in the slurry cut the Si via a rolling-indenting material removal process. More recently, there is a growing trend to replace the LAWS process with a more efficient fixed abrasive diamond wire sawing (DWS) process, especially for mono-Si wafers [10]. Instead of pouring a slurry onto the fast moving wire during cutting, diamond grits are fixed to the wire by electroplated nickel. The fixed abrasive method has been shown to yield a two-fold increase in the cutting speeds, decrease the thickness of the saw damage layer, and provide improvements in the loss and recycling of kerf [11-13].

Because the grits are fixed to the wire, the dominant cutting mechanism in DWS is a scratching-indenting process compared to the rolling-indenting process in LAWS.

Following the wire sawing step, the Si wafer is cleaned and the saw damage is removed by a wet chemical etching solution. The solution typically consists of a 20-30% concentration of potassium hydroxide (KOH) or sodium hydroxide (NaOH) [14].

After saw damage removal, the Si wafer is ready for use as the basic substrate for the fabrication of solar cells. Some of the subsequent processing steps to manufacture conventional crystalline silicon solar cells include cleaning, p-n junction formation, front surface passivation and creation of an antireflection coating, front contact formation, and rear structure formation [14, 15].

1.2 Motivation and Problem Statement

The manufacturing processes previously described produce residual stress in Si wafers. Residual stress is defined as the stress remaining in a material after the removal of all externally applied thermal and/or mechanical loads. It can be a consequence of manufacturing, material processing, or load application during service [16]. In the case of Si wafers, manufacturing induced residual stress can lead to early fracture and breakage, adding to the high cost of solar cell production.

The two primary sources of manufacturing induced residual stress in PV Si wafers consist of the casting or CZ process used to produce a Si ingot, and the wire sawing process used to produce the wafers. During solidification of a cast mc-Si ingot or a CZ mono-Si ingot, a thermal gradient is created by the temperature distribution, which results from non-uniform cooling and a non-planar solid-liquid front [17]. In addition, the wire

sawing processes, LAWS or DWS, produce residual stress and damage in the near-surface of the wafers due to mechanical interaction of the abrasive grit and Si.

Understanding manufacturing induced residual stress is imperative to improving wafer mechanical integrity and increasing yields in production. To date, the direct contributions of residual stress produced by the thermal gradient of the solidification process and the wire sawing processes have not been determined. This thesis aims to quantify the residual stress magnitudes, type (tensile vs. compressive), and spatial distributions manifested in the wafer due to thermal gradients during ingot solidification, and due to wire sawing processes, namely, LAWS and DWS.

Many previous studies of the fracture and breakage of Si wafers utilize wafer bending tests and rely on statistics to determine fracture strength [18-21]. These approaches are not able to isolate the source of fracture or examine the internal stress spatial distribution to provide an in-depth scientific understanding of manufacturing-induced residual stress.

Additionally, the impact of manufacturing induced residual stress on the electrical performance of Si wafers has not been adequately clarified. While several studies have been conducted to investigate the correlation between residual stress and electrical properties in the areas of defects, grain boundaries, and recombination centers [22-25], work specifically analyzing casting/solidification induced residual stress and its effect on electrical performance is limited. He [26] found a positive correlation between areas of high residual stress and improved electrical performance in cast, EFG, and ribbon Si wafers. However, the work did not identify the type of stress, tensile or compressive. This thesis aims to expand the understanding of the correlation between residual stress and

electrical performance of mc-Si wafers by isolating compounding variables such as crystalline orientation. This knowledge is needed to improve Si wafer quality and improve Si based solar cell efficiencies.

1.3 Research Objectives

Two specific research objectives are addressed in this thesis. They are:

Research Objective 1

a) To understand and quantify the contribution of residual stress generated in cast mc-Si wafers by the two wire sawing processes: LAWS, and DWS.

b) To understand and quantify the contribution of residual stress produced by the thermal gradient during solidification of a cast mc-Si ingot.

Research Objective 2

To understand the effect of solidification/casting induced residual stress on Si wafer photoluminescence, simultaneously providing results indicative of finished Si cell electrical performance.

1.4 Approach

An experimental approach is used to achieve the stated research objectives. All experiments are carried out using industrially manufactured mc-Si wafers in order to ensure practical value of the knowledge gained in the study. Near-infrared birefringence polariscopy and polarized micro-Raman spectroscopy, respectively, are used to characterize and quantify the residual stress through the wafer thickness and in the wafer surface. Both techniques measure residual stress based on different behaviors of the

physical interaction of light and matter. While near-infrared birefringence polariscopy provides a through-thickness residual stress measurement based on the principles of photoelasticity, polarized micro-Raman spectroscopy, which uses the Raman effect to measure surface stress, lies within the realm of solid-state physics. In addition, wet chemical isotropic etching is used to understand residual stress as a function of Si wafer depth, both at the wafer surface where saw damage is present, and in the bulk of the wafer, where residual stresses are primarily generated by the thermal gradients due to the casting process.

The second research objective, which targets the effect of residual stress on the electrical performance of Si wafers, is addressed through photoluminescence (PL) measurements in addition to the residual stress measurement techniques previously mentioned.

1.5 Thesis Outline

The remainder of this thesis is organized as follows. Chapter 2 presents a comprehensive literature review of prior work to provide a foundation of the current knowledge concerning the research objectives. Chapter 3 explains the fundamental physical principles, experimental set-ups, and methods of the two residual stress measurement techniques used in the thesis, namely, near-infrared birefringence polariscopy and polarized micro-Raman spectroscopy. Chapter 3 concludes by detailing the experimental validation procedure and results for the polarized micro-Raman spectroscopy measurement technique.

Chapters 4 and 5, respectively, describe two experiments, which were designed and carried out to address the specific research objectives. Chapter 4 describes the experimental procedures, discusses the results, and presents the conclusions of the experiments designed to address the first research objective, which aims to isolate and quantify the residual stress in mc-Si wafers due to solidification during casting and due to wire sawing. Chapter 5 describes the experimental method, discusses the results, and presents conclusions for the experiment designed to address the second research objective, which is to evaluate the effect of manufacturing induced residual stress on the electrical performance of mc-Si wafers, simultaneously providing results indicative of finished cell performance. Finally, the conclusions of this thesis and recommendations for further study are given in Chapter 6.

CHAPTER 2
LITERATURE REVIEW

Chapter 1 provided a summary of the manufacturing process used to fabricate multi-crystalline and mono-crystalline Si ingots, and subsequently wafers. Additionally, Chapter 1 described the background, motivation, and the research objectives of the thesis. This chapter presents a targeted literature review of prior work concerning the research objectives. The chapter is divided into several sections, which include the mechanical characterization of wire sawing induced damage in crystalline Si wafers, characterization of residual stress produced by the thermal gradient from the solidification/casting process, and the current understanding of the relationship between residual stress and electrical performance of crystalline Si wafers used as substrates for solar cells.

2.1 Characterization of Saw Damage

While the saw damage layer in mc-Si wafers has been studied through the use of both mechanical and electrical property characterization, residual stress measurements specific to saw damage are lacking. The Loose Abrasive Wire Sawing (LAWS) and Diamond Wire Sawing (DWS) processes introduce micro-cracks, pits, spalling, and surface roughness in crystalline Si wafers. DWS is quickly being adopted for the cutting of mono-Si wafers due to the benefits it offers in manufacturing efficiency and cost reduction. Difficulties in the acidic texturing of mc-Si wafers have however prevented DWS from being widely used for the production of mc-Si wafers [1, 27]. Therefore, the

characterization of both LAWS and DWS sawing processes is relevant today and of interest to the photovoltaic manufacturing community.

Numerous experiments have been conducted to investigate sawing process induced damage (or saw damage) by examining the resulting wafer surface morphology, micro-cracks, wafer fracture strength, wafer surface roughness, and the wafer thickness for crystalline Si wafers produced by LAWS and DWS [19, 21, 28-34]. Scanning electron microscope (SEM) images of mc-Si wafer surfaces produced by LAWS and DWS are shown in Figure 2.1.

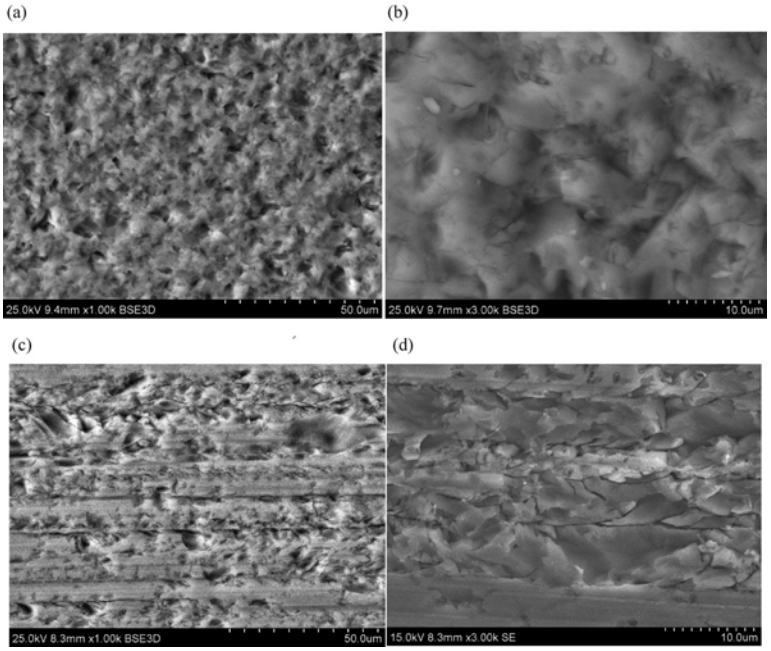

Figure 2.1: SEM images of mc-Si wafer surfaces sawn by (a,b) LAWS and (c,d) DWS. (a,c) low magnification, (b,d) high magnification [21].

Figure 2.1 shows the characteristic surfaces of the two wire sawing processes. Figure 2.1(a) and Figure 2.1(b) show the characteristic non-directional pitted surfaces of LAWS wafers while Figure 2.1(c) and Figure 2.1(d) show the wire striation lines prevalent on the surfaces of DWS wafers.

Wu et al. [34] performed a detailed study to compare the fracture strengths of LAWS and DWS wafers. The study reported the density of micro-cracks (the number of micro-cracks per mm) in DWS wafers to be 15-20 mm^{-1}, which is larger than the density of micro-cracks in LAWS wafers, which was reported to be 5-8 mm^{-1}. While the mean or 'expected crack length' for DWS wafers was smaller than the expected crack length for LAWS wafers, the maximum micro-crack length measured in both DWS and LAWS wafers was 5μm - 10μm depending on the location measured. DWS wafers were found to have fracture strength (in four point bending) equal-to or superior to LAWS wafers. However, Wu et al. did not consider the relative direction of the applied bending stress in four-point bending to the direction of DWS wire saw marks, a variable which was found to cause large deviations in the fracture strength of DWS wafers in subsequent studies [21, 30].

Using four-point bending, the fracture strength of DWS wafers has been reported to be greater than the fracture strength of LAWS when stress is applied perpendicular to the wire sawing direction, but lower than the fracture strength of LAWS wafers when stress is applied parallel to the sawing direction [21, 30].

Yang et al. [21] found the fracture strength of LAWS wafers to be dependent on the location of wafer relative to where the wire enters the Si brick and where it exits the Si brick. LAWS causes differences in the wafer thickness from wire-entry to wire-exit while DWS produces a more uniform thickness throughout the wafer [21]. The variations in thickness of LAWS wafers are believed to be caused by a decrease in the abrasive grit size from wire-entry to wire-exit, which occurs as the abrasive grit breaks down during the sawing process [21, 35]. DWS fracture strength has been shown to be highly

dependent on the direction of bending stress applied in four-point bending relative to the direction of the wire saw used to slice the wafers (or wire striations). Table 2.1 shows fracture strength results of DWS and LAWS wafers recorded from multiple sources.

Table 2.1: Characteristic fracture strength measurements using the Weibull modulus.

Sawing Process	Wafer Location in Si Brick	Bending Direction Relative to Saw Marks	Characteristic Strength (MPa)	Weibull Modulus	Reference
LAWS	Interior	Parallel	141	8.4	[21]
LAWS	Interior	Perpendicular	157	7.7	[21]
DWS	Interior	Parallel	113	12.1	[21]
DWS	Interior	Perpendicular	237	3.5	[21]
LAWS	n/a	n/a	136-160	n/a	[34]
DWS	n/a	n/a	136-221	n/a	[34]
DWS	n/a	Parallel	~120	n/a	[30]
DWS	n/a	Perpendicular	~200	n/a	[30]
LAWS	n/a	Parallel	~200	n/a	[30]
LAWS	n/a	Perpendicular	~200	n/a	[30]

(n/a: not reported)

Studies that specifically seek to measure the residual stress in Si wafers due to wire-sawing are limited. Popovich et al. [36] used micro-Raman spectroscopy to measure the residual stress in the saw damage layer of mc-Si LAWS wafers. The stress in the saw damage layer was reported to be compressive in nature, and found to be equal to 500 MPa using a biaxial stress assumption.

Wurzner et al. [37] performed scribing on mono-Si using single diamond particle tips to investigate the cutting mechanism in DWS. Raman spectroscopy peak shift measurements revealed the stress state created by DWS scribe tests to also be compressive, however the stress magnitudes were not determined.

Yang et al. [38] used the same near-infrared birefringence polariscope used for the experiments conducted in this thesis to investigate residual stress in DWS mc-Si wafers before and after wet chemical etching using HF/HNO_3, which removed 5μm of the wafer surface. Their results showed that after etching, both the maximum and average maximum residual shear stress, τ_{max}, in the wafers decreased and the fracture strength improved. Based on the reports of micro-crack lengths previously mentioned [21, 30, 34], it has been determined that micro-cracks in DWS wafers can extend to lengths greater than 5μm, and therefore the saw damage layer was not completely removed in this experiment. Consequently, the results did not ascertain the effect of DWS on residual stress and fracture strength.

In addition to the previously mentioned mechanical characterization of the saw damage layer, Figure 2.2 shows the minority carrier lifetime plotted as a function of etch depth as reported by Watanabe et al. [13] for LAWS (loose-abrasive) and DWS (fixed-abrasive) sawn wafers.

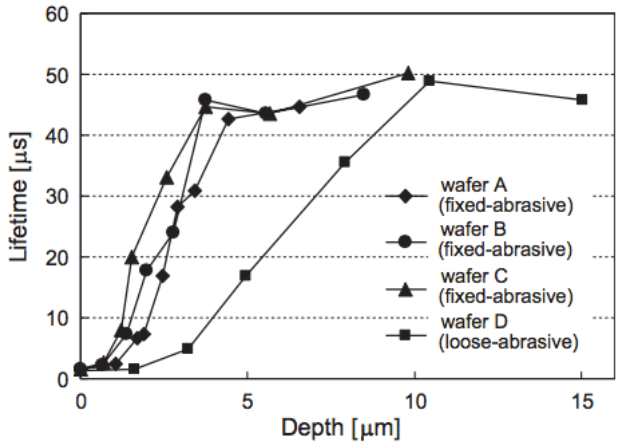

Figure 2.2: The relationship between the etching depth of one side of wafers and the minority carrier lifetime [13].

DWS was found to produce less saw damage, as shown by the drastic improvement in minority carrier lifetime after 5μm saw damage removal. The LAWS wafer however did not exhibit an increase in minority carrier lifetime until 10μm of Si was removed by etching.

2.2 Characterization of Thermal Gradient Induced Residual Stress

Experimental measurements of the thermal gradient induced residual stress are currently limited due to measurement difficulties [39]. The residual stress produced by the thermal gradient induced during casting and solidification of Si ingots has primarily been investigated through the use of numerical modeling of the solidification process for casting mc-Si ingots [17, 39, 40]. Oswald et al. [39] used numerical modeling and simulation and showed the stress state at the center of an mc-Si cast ingot to be tensile. Oswald et al. deduced their finding based on the exterior of the ingot solidifying first during casting, creating solid material around the center of the ingot. Due to the thermal volumetric expansion of Silicon, when the center of the ingot solidifies, tensile stresses result within the ingot. Huang et al. [17] determined that the stress at the center of an mc-Si cast ingot was greater than 100 MPa and decreased as one moves axially from the center (highest stress) to the edges of the crucible (lowest stress). The magnitude of stress at any location is dependent on the casting process used and the accompanying thermal gradients.

In mc-Si wafers, experimental studies have been conducted to compare residual stress in the center of grains versus at grain boundaries [24, 25, 28, 41]. Differences in the stresses at the center of the grains and at grain boundaries have been found to be in the

range of tens of MPa [24]. Popovich et al. [36] used micro-Raman spectroscopy to measure the stress at the center of grains and at grain boundaries under an applied tensile load. Residual stresses at the grain boundaries were found to be 50-70 MPa higher than the residual stress within the grain under tensile load. Popovich et al. concluded from this finding that the grain boundaries are the most probable sources of mechanical strength degradation in mc-Si wafers.

2.3 Effect of Residual Stress on the Electrical Performance of Solar cells

Stress as a parameter for electrical activity has been previously studied in relationship to the band gap energy for semiconductor materials [23, 42-44]. The band gap energy is the difference in energy states between the valence band and the conductance band, or the states in which an electron is bound to an atom and when it is free to conduct throughout the crystal. The band gap energy of a semiconductor material is one of the most critical electrical parameters for solar cell performance, along with the number of free carriers available for conduction, and the generation or recombination rate of free carriers in response to energy or light incident on the substrate [45].

A number of studies have been performed to examine how applied stress affects electrical activity in semiconductor Si, without considering the effect of crystal structure i.e. mono-Si versus mc-Si. The band gap energy dependence on applied stress in Si was first experimentally determined in 1958 by Gundel et al. [46] for hydrostatic compressive stress, and later in 1962 for uniaxial compressive stress by Rindner [42]. It is well understood that applied stress directly changes the band gap energy of Si and this change is highly reversible if the applied stress is removed. In the case of uniaxial compressive

stress, the change in band gap energy is dependent on the direction of stress applied relative to the Si crystal lattice orientation. These experimental findings were theoretically proven by Goroff et al. in 1963 [43], and by Wortman et al. in 1964 [44].

While the effect of applied stress on electrical activity in Si has been examined, the quantitative effect of residual stress induced during industrial manufacturing of wafers has not been studied sufficiently. Chen et al. (2008) [22] used both electron beam induced current (EBIC) mapping and a scanning infrared polariscope to examine electrical activity and residual strain, respectively, at large and small angle grain boundaries in mc-Si. However, no relationship between electrical activity and residual strain was found to exist. Another recent publication [24] attempted to compare the results of micro-Raman spectroscopy, electron backscatter diffraction (EBSD), and EBIC in areas of grain boundaries exhibiting stress fields and again found no correlation between recombination activity and residual stress. The latter findings were later hypothesized by Gundel et al. [23] to be due to the limited spatial resolution of the different measurement methods used. Gundel et al. simultaneously studied stress and defect luminescence using micro-photoluminescence (μPL) spectroscopy. Using μPL to map areas surrounding metal precipitates in Si wafers, both tensile and compressive stress fields were identified, and the residual stress and μPL response were simultaneously measured at the same locations. A positive correlation was found between tensile stress and increased recombination activity surrounding metal precipitates, regardless of the type of metal precipitate. Conversely, compressive stress was found to decrease the recombination activity surrounding the metal precipitates. These findings were attributed to the piezo-resistivity of Si. Compressive stress decreased carrier

mobility while tensile stress increased carrier mobility. In the regions containing metal precipitates, the increased mobility caused by tensile stress surrounding recombination centers facilitated the movement of carriers to the recombination center, and is therefore assumed to be detrimental to the electrical performance of a finished cell in these regions. Likewise, compressive stress hindered recombination in areas surrounding the precipitates. This was an important finding as its impact could potentially lead to improvement in finished solar cell efficiency if the stress fields and stress type in the Si wafer can be controlled.

Additionally, Sarau et al. [47] conducted a point-by-point correlation of micro-Raman (to measure stress) and EBIC measurements (to determine electrical activity) in areas containing dislocations, grain boundaries, and impurities. The findings indicated that internal stresses of several tens of MPa do not influence the minority carrier recombination in block-cast and EFG mc-Si.

Residual stress is typically studied in local areas surrounding recombination centers and defects that could lead to Shockley-Read-Hall (SRH) recombination. In addition, previous studies tend to only use micro-Raman spectroscopy, which is only able to examine the stress state in the Si wafer surface, and not in the bulk. He [26] used near-infrared birefringence polariscopy and PL to study through-thickness residual stress and electrical performance in cast, EFG, and ribbon Si wafers. He found a positive correlation between the spatial distribution of areas with high residual maximum shear stress and improved electrical performance. However, the work did not examine the stress type (tensile vs. compressive) or attempt to alter the stress state of the samples.

2.4 Summary

It is clear from the literature survey that:

1. Both the mechanical integrity and the electrical performance have been investigated in the saw damage layers of Si wafers produced by DWS and LAWS. However, to date, no studies have been published which explicitly study and quantify the residual stress generated by each wire sawing process in industrially manufactured Si wafers.
2. Several numerical modeling and simulation studies have been completed to quantify the residual stress induced by the thermal gradients present during solidification of mc-Si ingots. In addition, specific regions in the wafers such as within grains and near grain boundaries in mc-Si wafers have been investigated. However, to date, there is limited published work that attempts to specifically characterize and quantify the residual stress generated by the thermal gradients during casting and solidification of mc-Si ingots, in comparison to the manufacturing induced residual stress resulting from wire sawing processes.
3. The correlation between residual stress and electrical performance is still not adequately understood. To date, no studies have been conducted with the goal of altering the residual stress state of a mc-Si wafer through annealing to examine the impact of residual stress on electrical performance, independent of differences in crystalline orientation.

The above limitations of prior work provide the motivation and justification for the work reported in this thesis. The remainder of this thesis describes research whose goal is to gain fundamental understanding of residual stress in cast mc-Si wafers. The

thesis focuses on characterizing and quantifying the residual stress produced by individual crystalline Si wafer manufacturing processes such wire sawing and casting/solidification. In addition, the effect of solidification induced residual stress on the electrical performance of Si wafers is investigated.

CHAPTER 3
RESIDUAL STRESS MEASUREMENT

Chapter 1 provided the necessary background, explained the research objectives, and provided a brief summary of the experimental approach for this thesis. The approach was based on the use of two measurement methods, near-infrared birefringence polariscopy and polarized micro-Raman spectroscopy.

This chapter first provides a description of the basic fundamental physical principles behind each measurement method. Subsequent sections explain the experimental set-up, methods, and the analysis used for each technique. The results of validation experiments are also presented for the polarized micro-Raman spectroscopy measurement procedure, which was validated both for its determination of crystalline orientation and the measurement of stress in mc-Si wafers.

3.1 Near-infrared Birefringence Polariscopy

The near-infrared birefringent polariscope is based on the principles of photoelasticity, which is a well-developed experimental method for analyzing the stress or strain fields in materials.

3.1.1 Fundamental Physical Principles

Maxwell's electromagnetic theory was pivotal in the understanding of light, the reason being that the theory allowed light to propagate through space unsupported by any known matter. The theory's foundation predicts the presence of two vector fields, an electric vector field **E**, and a magnetic vector field, **B**, which are perpendicular to each other, as shown in Figure 3.1.

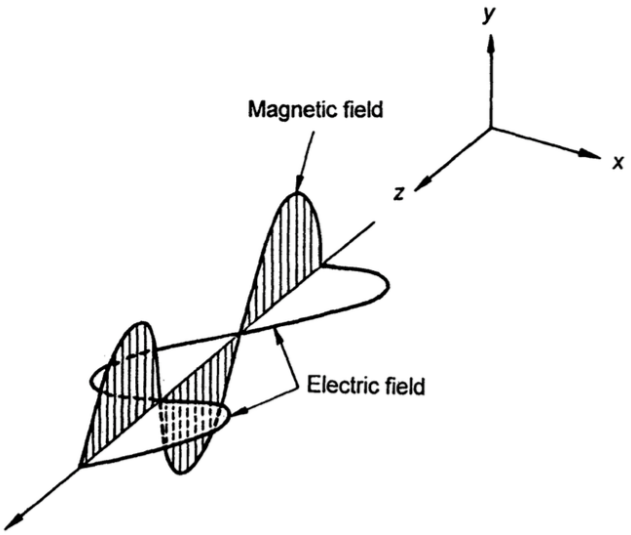

Figure 3.1: Electromagnetic field vectors of light [48].

Either of these two vector fields can be used to describe the fundamental light vector. The theory of photoelasticity uses the electric vector as the fundamental light vector.

The speed of light, *v*, through a medium is described by the following equation,

$$v = \frac{c}{n} \qquad (1)$$

where *n* is the index of refraction of the medium, and *c* is the speed of light in a vacuum. An optically isotropic material is one that has a constant index of refraction, *n*, regardless of the direction of incident light on the material. Certain crystalline solids are optically anisotropic, meaning that the index of refraction changes based on the direction of incident light. One example is silicon carbide, which refracts a single ray to produce two rays, an ordinary ray and an extraordinary ray as shown in Figure 3.2. This phenomenon is known as “double refraction” or “birefringence” and forms the basis of photoelasticity.

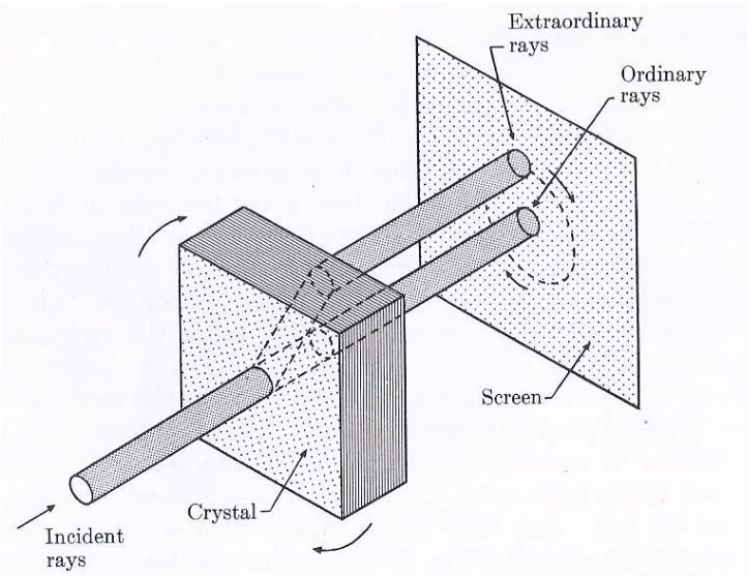

Figure 3.2: Behavior of laterally shifted ordinary and extraordinary rays [49].

The extraordinary ray exhibits a lateral shift from the ordinary ray. If the incident light falls in a direction parallel to the optical axis of the crystal, no birefringence will occur. If an incident ray is perpendicular to the crystal's optic axis, the extraordinary ray travels at a different speed from the ordinary ray, but in the same direction. Photoelasticity makes use of this phenomenon. The two waves that emerge from the crystal are perpendicular to each other and are polarized, and the relative phase difference between the refracted rays forms a fringe pattern due to the optical interference of the two waves. Figure 3.3 shows the behavior of polarized light through a birefringent material.

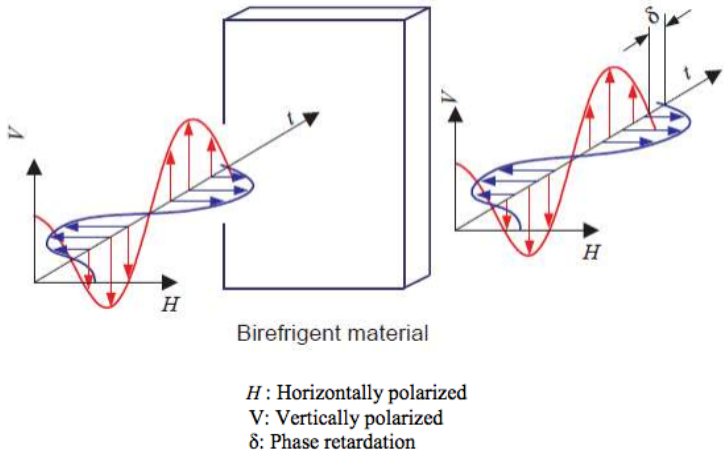

Figure 3.3: Light behavior through a birefringent material [50].

In Figure 3.3, δ is the phase shift or retardation of the polarized vectors after emerging from the material. Silicon, in its stress-free state, is an optically isotropic material, and no birefringence occurs. Under load, or in a stressed state however, the Si crystal behaves like an optically anisotropic medium.

The relationship between strain and birefringence was first discovered by Brewster [51] in 1816. E.G. Coker in his work, A Treaty in Photoelasticity [52], paraphrases Brewster's discovery as the following: "*When light passes through a plate of glass which is stressed transversely to the direction of propagation, the axes of polarization in the glass are along, and perpendicular to the direction of state.*" The directions of the refracted light are aligned with the principal axes of stress at any point in the material.

In 1852, Maxwell deduced that the changes in indices of refraction, *n*, were linearly proportional to the stresses induced in the crystal. The basis of this finding is called the stress optic law. The stress optic law can be derived very easily from Equation (1) as shown. Two equations are first formed,

$$n_1 - n_0 = c_1\sigma_1 + c_2\sigma_2 \quad (2)$$

$$n_2 - n_0 = c_1\sigma_2 + c_2\sigma_1 \quad (3)$$

where n_0 is the index of refraction in the unstressed state, and n_1, and n_2, respectively, are the indices of refraction along the two principal axes of σ_1, and σ_2, in a crystal. The material constant, c_1, is called the "direct stress-optic coefficient" and the constant c_2 is the "transverse stress-optic coefficient". Subtracting Equation (3) from Equation (2) eliminates n_o and results in Equation (4).

$$n_1 - n_2 = (c_1 + c_2)(\sigma_1 - \sigma_2) \quad (4)$$

Additionally, the well-established equation,

$$\delta = \frac{2\pi t}{\lambda}(n_1 - n_2) \quad (5)$$

which demonstrates the behavior of a half-wave plate producing polarized light, is needed for the derivation. The term δ is the phase shift, t is the material thickness, λ is the wavelength, and n_1 and n_2, respectively, are the indices of refraction for the two axes of the half-wave plate, which are typically referred to as the slow and fast axes. A diagram demonstrating this behavior is shown in Figure 3.4.

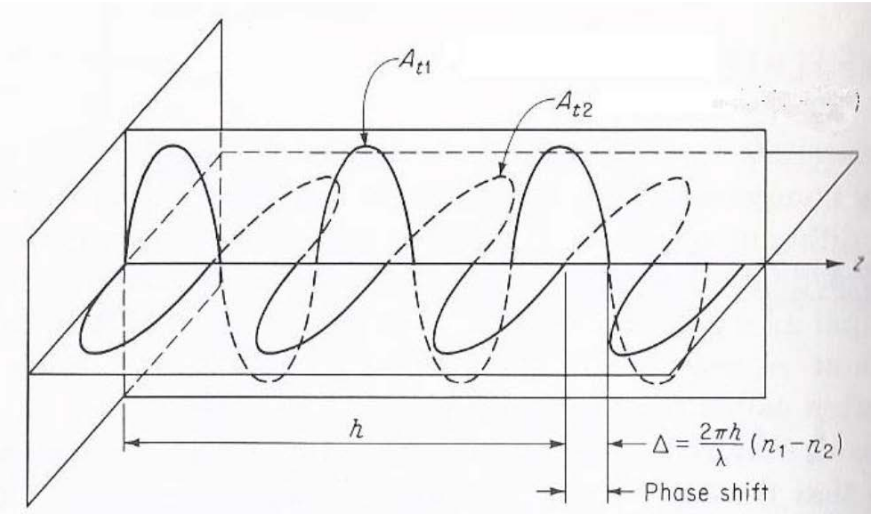

Figure 3.4: Behavior of a half-wave plate [53].

Equation (5) can be easily rearranged to the following equation.

$$n_1 - n_2 = \frac{\lambda}{2\pi t}\delta \qquad (6)$$

The term on the right hand side of Equation (6) can be substituted for the left hand term of Equation (4) as they are shown to be equivalent. Performing this substitution finally results in the stress optic law:

$$\tau_{max} = |\sigma_1 - \sigma_2| = \frac{\lambda}{2\pi t C}\delta \qquad (7)$$

where the constant *C* is the stress optic coefficient and is dependent on the material under observation. In the case of many crystalline materials including Si, *C,* is also dependent on the crystal orientation. Various studies have shown that this constant also depends on wavelength and should be evaluated carefully [48]. The difference $|\sigma_1 - \sigma_2|$ is the absolute value of the difference between the largest and smallest principal stresses, and is equal to twice the maximum shear stress, $2\tau_{max}$. The relationship between the principal stress and τ_{max} is shown in Figure 3.5 using Mohr's circle.

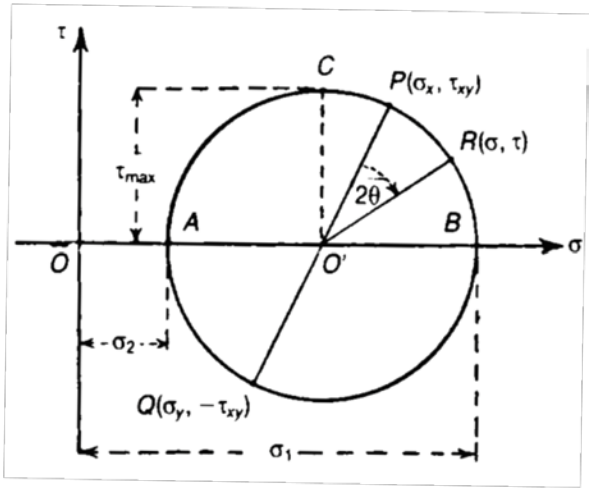

Figure 3.5: Mohr's Circle [54].

Ambiguity results when attempting to separate the effects of the principal stresses, σ_1 and σ_2. The isoclinic angle, θ, can be evaluated directly using the polariscope, however the principal or component stresses cannot be evaluated.

3.1.2 Experimental Set-up

To measure the phase shift δ, and the isoclinic angle θ, a polariscope, which consists of a series of optics and a light source, is used. The experimental set-up for the polariscope is shown in Figure 3.6.

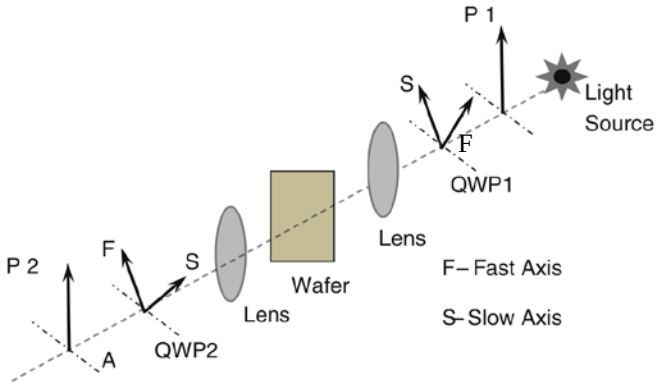

Figure 3.6: Schematic for near-infrared birefringence polariscope [55].

In Figure 3.6, the terms “QWP1” and “QWP2” refer to the quarter-wave plates. The terms “P1” and “P2” refer to the half-wave plates in the set-up. The set-up, method for determination of the photoelastic parameters, and the technique were previously developed by Zheng et al. [56, 57], Danyluk et al. [58], He et al. [59], Li [50], Skenes [8], Skenes et al. [8, 60, 61], and Prasath et al. [55].

Each component of the diagram in Figure 3.6 will be explained in order, beginning with the light source. An 1150 nm wavelength tungsten source with bandpass filters is used to provide light transmitted through the wafer. Silicon is opaque to UV and visible light, but has a 50% transmission ratio for near-infrared light at 1100 nm. 1150

nm light was chosen as the wavelength that can transmit through Si and thereby provide measurement of the phase shift of light through the wafer.

The light from the source first travels through a half-wave plate to create linearly polarized light. Following, a quarter-wave plate is in place to change the polarization state of the light from linear to circular. Figure 3.7 illustrates the differences in linear and circular polarization states.

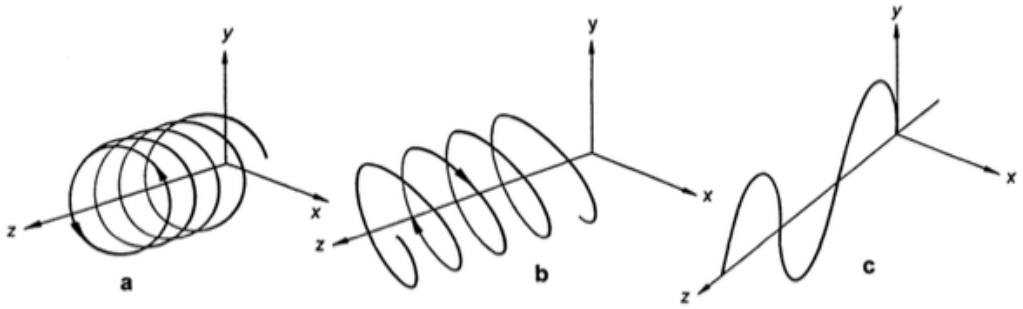

Figure 3.7: (a) circularly polarized light, (b) elliptically polarized light, (c) linearly polarized light [48].

Two large lenses are placed on either side of the wafer sample in order to collimate the light through the sample. After the sample, there is another quarter-wave plate, followed by a half-wave plate, which acts as an analyzer, blocking light of certain directions in order to provide measurement of the phase shift through the sample.

The phase difference between the two optical paths can be measured as an intensity variation by rotating the optical components of the polariscope. This technique, called phase shifting, is used to determine the photoelastic parameters, and was first developed by Hecker and Morsch [62] in 1986. By varying the phase difference at intervals or ‘steps’, an adequate number of intensity equations can be generated to solve for the isoclinic angle, θ, and the phase shift, δ, at each point imaged in the wafer. The 10 step phase-shifting algorithm described in Prasath et al. [55] was used in this research to

determine the photoelastic parameters δ and θ. The isoclinic angle, θ, and the phase shift, δ, were then used to calculate the difference in principal stresses and therefore the maximum shear stress, τ_{max} (see Equation (7)).

The polariscope was previously calibrated using a four point bending experiment with a mono-crystalline Si beam. The stress optic coefficients, C, for different crystallographic orientations, were determined from the work of Skenes [8]. In the case of mc-Si, an average stress optic coefficient was calculated from the known coefficients for Si [59] and used to calculate τ_{max}. The use of this average stress optic coefficient can introduce errors up to 34% of the measured value [50]. However, the error is also dependent on the thickness of the sample, and phase retardation measured and was found to be significantly less than 34% in the calculations of τ_{max} for this thesis.

3.2 Polarized Micro-Raman Spectroscopy

3.2.1 Fundamental Physical Principles

In 1928, Sir C.V. Raman won the Nobel Prize for discovering what became known as the “Raman effect”. The Raman effect describes the inelastic interaction of light and matter. Simply stated, when light interacts with matter, the majority of light is scattered elastically, meaning there is no exchange of energy with the medium, known as Rayleigh scattering. A small amount of light, however, is scattered inelastically, termed Raman scattering. See Figure 3.8.

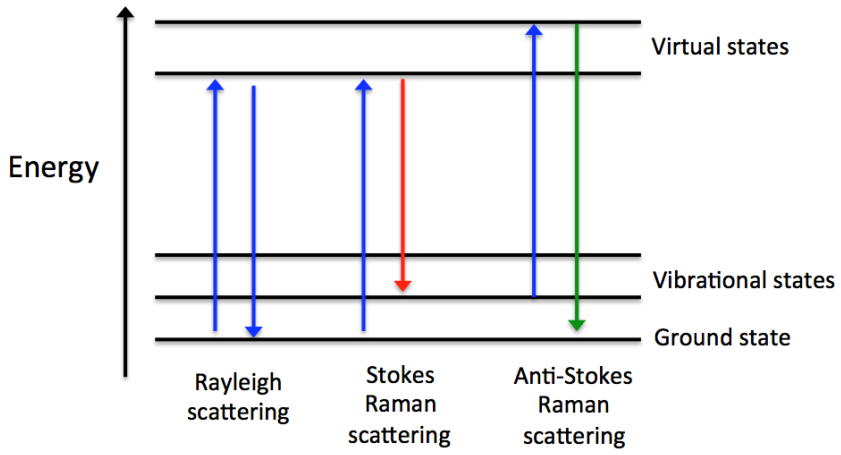

Figure 3.8: Rayleigh, Stokes Raman Scattering, and Anti-Stokes Raman scattering.

There are two types of Raman scattering, Stokes and Anti-Stokes. In Stokes Raman scattering, the scattered photon has less energy than the incident photon while in Anti-Stokes Raman scattering, the scattered photon has more energy than the incident photon. The fundamental principles of Raman spectroscopy, which is based on the Raman effect and lie within the realm of solid-state physics, will be described in this section.

The vibrations of a crystal are described by the vibrations of its crystal lattice, or collective motions in the form of waves, not of its individual atoms. Each possible vibration j of the lattice is characterized by a wave vector q_j, and a frequency ω_j [63]. The vibration amplitude at position r is given by,

$$Q_j = A_j \exp\left[\pm \mathrm{i}\left(q_j \cdot r - \omega_j t\right)\right] \qquad (8)$$

where Q_j is the normal coordinate of the vibration, and A_j is a constant. This quantized lattice vibration is called a “phonon”, or “normal mode”.

When strictly monochromatic light of a well-defined frequency ω_i is incident on a crystal with wave vector k_i, the associated electric field produces an electric moment at position r, having the following equation,

$$P = \varepsilon_0 \chi \cdot E_0 \exp[\pm \mathrm{i}(k_i \cdot r - \omega_i t)] \quad (9)$$

where ε_0 is the permittivity of free space and χ is the "susceptibility tensor", which describes the response of the crystal to the electric field [63]. If the atoms of the sample are vibrating, the susceptibility changes as a function of the vibrations. This is expressed by the susceptibility tensor in a Taylor series with respect to the normal coordinate Q_j. See the work of De Wolf [64] and Hayes [65] for more detailed explanation. The Taylor series expansion shows that the induced moment re-radiates the light with three distinct frequency components, Rayleigh, Stokes Raman, and anti-Stokes Raman, where the Rayleigh component is the first term of the Taylor series expansion, and Stokes Raman and anti-Stokes Raman components are the second and third terms, respectively. The Stokes Raman term gives the largest peak amplitude between Stokes and anti-Stokes Raman and is measured by Raman Spectroscopy.

3.2.2 Application of Raman Spectroscopy

Micro-Raman spectroscopy experiments are simply Raman spectroscopy measurements that use a microscope to focus the light onto the sample. In a micro-Raman spectroscopy experiment, monochromatic light is made incident on the sample. The energy is absorbed and re-radiated with three different amplitudes resulting in Rayleigh, Stokes Raman, and Anti-Stokes Raman. The change in amplitude due to Raman scattering is used to study the crystal lattice vibration. Small changes in amplitude can be related to strains in the lattice.

A typical Raman spectrum for Si is shown in Figure 3.9.

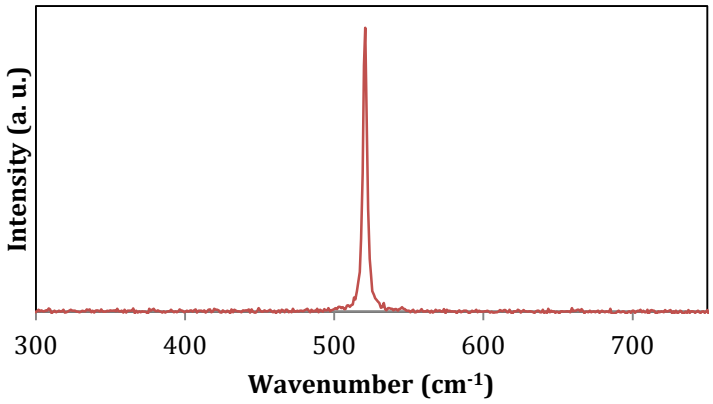

Figure 3.9: Raman spectrum showing the first order Raman peak of crystalline Si at 520.46 cm^{-1}.

Unstrained Si produces a first order Raman peak at the wavenumber 520.46 cm^{-1}. A positive shift (to higher wavenumbers) in the peak of the spectrum correlates to compressive stress while a negative shift (to lower wavenumbers) correlates to tensile stress. The term for peak shift is represented by $\Delta\omega$. The mathematical relationship between stress and peak shift is described in Section 3.2.7.

3.2.3 Dependence of Polarization on Raman Intensity

The intensity of Raman scattering, *I*, depends on the polarization of the incident light, $\vec{e_i}$, and scattered light, $\vec{e_s}$, and is given by the Equation (10),

$$I(\vec{e_i}, \vec{e_s}) \approx I_0 \cdot \sum_{j=1}^{3} \left| \vec{e}_i \cdot R'_j \cdot \vec{e}_s \right|^2 \qquad (10)$$

where R_j is the Raman tensor, which is unique to each crystallographic class. The Raman tensors are obtained from group theoretical considerations and are second-rank tensors, which are proportional to the susceptibility tensor, X_j [65, 66]. The index *j* goes from 1 to 3 as Si has three active optical phonons, one representing each of the three axes of the

crystal coordinate system, x = [100], y = [010], z = [001]. Loudon [66] derived the Raman tensors for each of the 32 crystallographic classes. Silicon belongs to the O_h crystallographic class and has three Raman tensors, shown below for the crystal coordinate system x = [100], y = [010], z = [001].

$$R_x = \begin{bmatrix} 0 & 0 & 0 \\ 0 & 0 & d \\ 0 & d & 0 \end{bmatrix}, \quad R_y = \begin{bmatrix} 0 & 0 & d \\ 0 & 0 & 0 \\ d & 0 & 0 \end{bmatrix}, \quad R_z = \begin{bmatrix} 0 & d & 0 \\ d & 0 & 0 \\ 0 & 0 & 0 \end{bmatrix} \qquad (11)$$

3.2.4 Experimental Method

In typical Raman spectroscopy based measurement of stress in mono-Si, the crystallographic orientation of the sample is known prior to the measurement. In the case of mc-Si, crystallographic orientation is not known, as it is random and dependent on the crystal growth during the casting process. Figure 3.10 shows a representative 156 mm x 156 mm mc-Si wafer, which has many different crystallographic orientations.

Figure 3.10: 156 mm x 156 mm mc-Si wafer.

The polarized micro-Raman spectroscopy method used to measure the stress state of Si in this thesis was developed by Becker et al. [28]. Using the method, each crystal to

be studied in a multi-crystalline sample is treated as a single crystal. The crystallographic orientation for each crystal is found in relation to the laboratory coordinate system. Figure 3.11 shows a diagram of the crystal and laboratory coordinate systems.

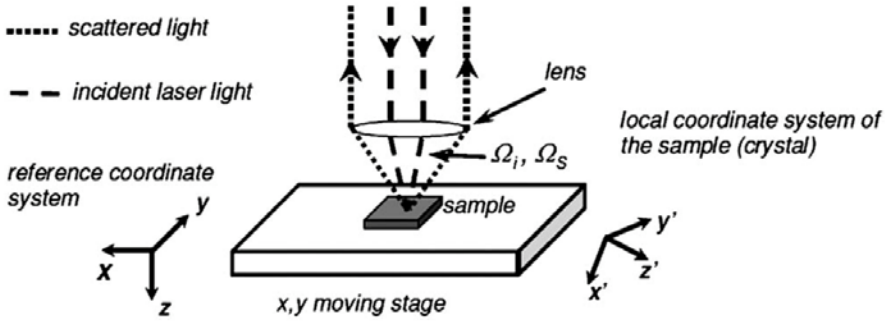

Figure 3.11: Crystal and laboratory coordinate systems [28].

Having determined the crystal orientation, and assuming a plane stress state, a stress tensor consisting of the components σ_{xx}, σ_{yy}, and τ_{xy} is calculated.

3.2.5 Experimental Setup

A schematic of the polarized micro-Raman experiment is shown in Figure 3.12.

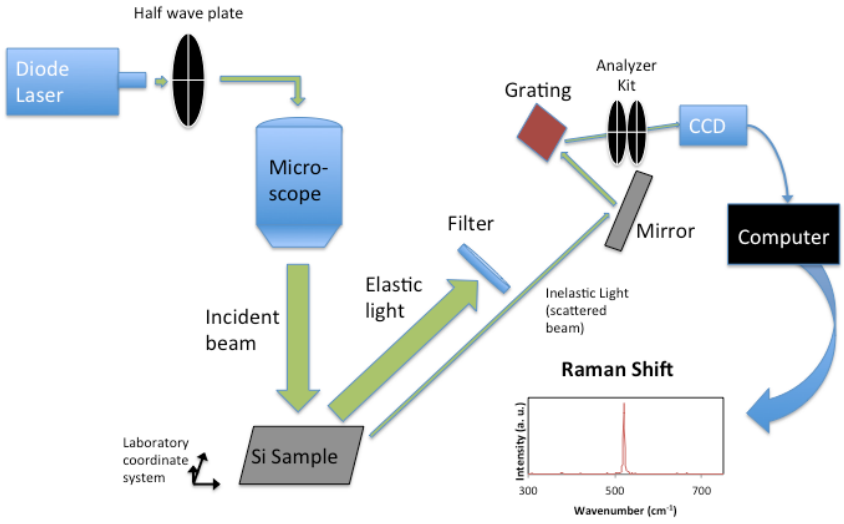

Figure 3.12: Schematic of polarized micro-Raman system.

A laser supplies the incident beam to the Si sample. A half-wave plate is placed in the path of the incident beam to control the polarization direction of the incident beam and a microscope is employed to focus the beam onto the sample. The elastically scattered light is blocked by a filter while the inelastically Raman scattered light is sent through a grating and an "analyzer kit" to analyze the polarization of the scattered beam before it is sent to the CCD detector. A computer processes the output from the CCD detector to provide the Raman spectrum.

A Renishaw InVia confocal microscope system with an attached Leica Microscope and a motorized *X*-*Y* stage was used for the experiment at Georgia Tech. The laser used was an Argon source 488 nm laser. The absorption/penetration depth for 488 nm wavelength light in Si is ~0.6μm and is independent of the crystal orientation [67]. A 50X microscope objective was used for all measurements, which resulted in a laser spot size of approximately 1.5μm. The Renishaw InVia system at Georgia Tech is equipped with the Renishaw "analyzer kit". The analyzer kit is made up of two half-wave plates and is shown in Figure 3.13.

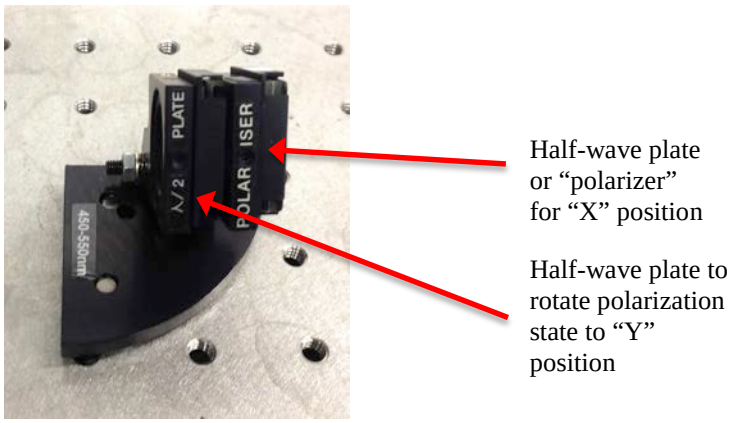

Figure 3.13: Analyzer kit within the Renishaw InVia system.

The analyzer kit is located in the path of the scattered beam before the detector. The analyzer consists of two half-wave plates, with their fast axes oriented 90° to each other. By moving the half-wave plate designated “polarizer” into the scattered beam path, only the light polarized in the ‘X’ laboratory coordinate direction is analyzed by the detector. By moving the designated “half-wave plate” and the “polarizer” into the beam path, the polarization is rotated 90° from X to Y, therefore, only the light polarized in the Y laboratory coordinate direction is analyzed by the detector. To summarize, there are two positions of the analyzed polarized light available, namely, X and Y aligned with the laboratory coordinate system.

The Renishaw InVia system was not equipped to allow polarization control of the incident light. In order to carry out the procedure of Becker et al. [28] and measure the crystal orientation, the linear polarization of incident light must be controlled in steps from 0° to 180°. A half-wave plate specific for the linear polarization of 488nm wavelength light was purchased from ThorLabs (WPH05M-488 - Ø1/2” Mounted Zero-Order Half-Wave Plate, Ø1” Mount, 488 nm) and placed in a rotation mount, shown in Figure 3.14.

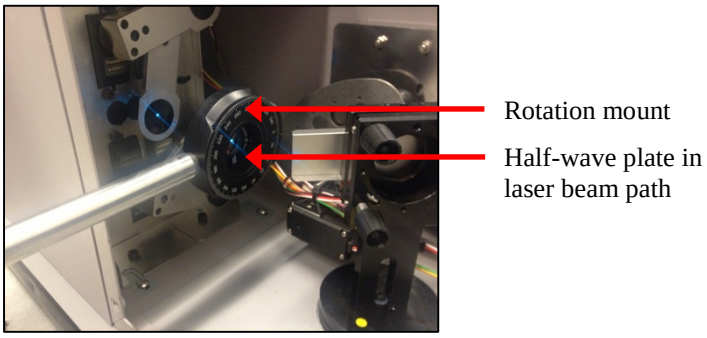

Figure 3.14: Half-wave plate placement in rotation mount in Renishaw InVia system.

The half-wave plate was placed in the laser beam path before entering the Renishaw system for easy access and manual rotation during measurements.

The general steps of the procedure described by Becker et al. [28] are shown in the process flow diagram of Figure 3.15, and will be explained in the subsequent sections of this thesis.

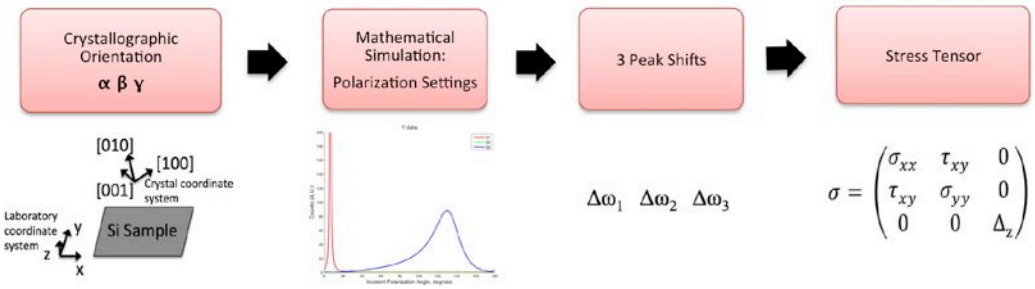

Figure 3.15: Process flow to determine stress tensor using polarized micro-Raman spectroscopy.

The major steps of the procedure are listed below.

1. Determination of crystallographic orientation of the grain of interest as denoted by the three Euler angles (α, β, γ).
2. Mathematical simulation of the intensity functions to find three polarization settings where the intensity of one phonon dominated over the sum of the intensities of the other two remaining phonons.
3. Using the three polarization settings found in step 2, three peak shifts were measured corresponding to the three phonon shifts.
4. The three peak shifts along with the three Euler angles found in step 1 were used to solve a series of nonlinear equations to find the stress tensor shown below.

$$\sigma = \begin{pmatrix} \sigma_{xx} & \tau_{xy} & 0 \\ \tau_{xy} & \sigma_{yy} & 0 \\ 0 & 0 & \Delta_z \end{pmatrix} \quad (12)$$

The Δ_z term acts as an error term to account for the residual stress that exists in the Z laboratory coordinate direction, counter to the plane-stress assumption. This term is discussed further in the subsequent sections.

3.2.6 Determination of Crystalline Orientation

Becker et al. [28] used the well-established dependence of polarization on scattering efficiency (see Equation (10)) to determine the crystallographic orientation of grains of unknown orientation in mc-Si wafers. Equation (13) incorporates an adjustment to Equation (10) which includes a transformation matrix, designated by **T**(*α, β, γ*), to allow for rotation between the two coordinate systems, the laboratory coordinate system and the crystal coordinate system.

$$I(\vec{e_i}, \vec{e_s}, \alpha, \beta, \gamma) \approx I_0 \cdot \sum_{j=1}^{3} \left| \left[[\mathbf{T}(\alpha, \beta, \gamma)] \cdot \vec{e}_i \right]^{\mathrm{T}} \cdot \boldsymbol{R'}_j \cdot [\mathbf{T}(\alpha, \beta, \gamma)] \cdot \vec{e}_s \right|^2 \quad (13)$$

In Equation (13), **T**(*α, β, γ*) is a rotation matrix where *α, β,* and *γ* represent the three Euler angles. The expression used for **T**(*α, β, γ*) is given in the Appendix. By experimentally controlling the polarization direction of the incident light and analyzing the scattered light, the resulting intensity functions are used to solve a nonlinear system of equations to calculate the Euler angles *α, β,* and *γ.*

Two functions are determined from the experimental data. With the analyzer in the X position, the incident beam is rotated from 0° to 180° at intervals of 8° using the mounted half-wave plate in the incident beam path and the crystalline Si peak intensity is measured. The analyzer is then switched to the “Y” position and again the intensity is

measured as a function of the incident beam polarization direction at rotation angles of 0° to 180° at intervals of 8°. An example of the resulting two functions is shown in Figure 3.16.

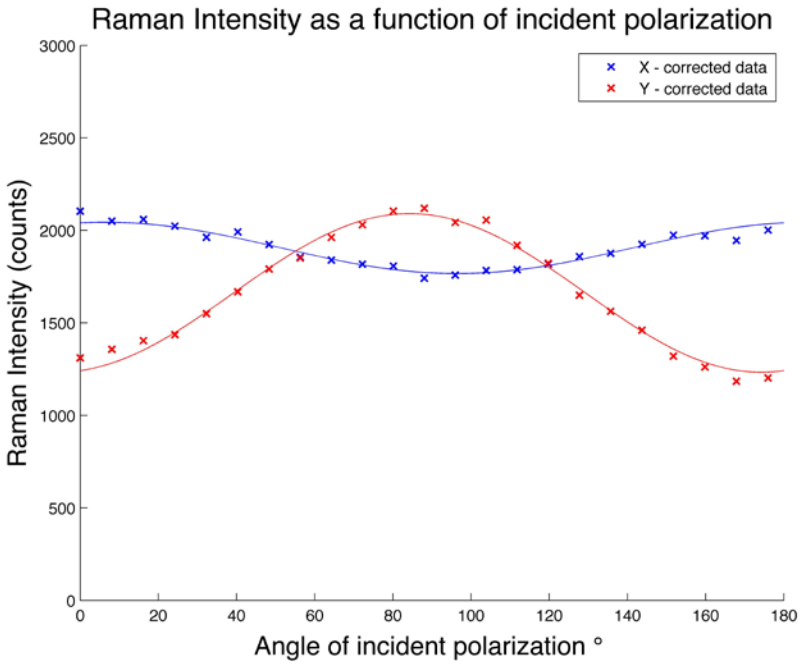

Figure 3.16: Example showing Raman intensity as a function of the angle of incident polarization.

Note that the data was corrected for variations in power due to the optical train. In order to perform this correction, the power on the sample stage was measured as a function of the polarization angle using an Ophir (model 3A) thermal power sensor. The correction is similar to the calibration procedure described by Hopkins et al. [68] and it allowed for the elimination of the *k* and *m* calibration constants used by Becker et al. [28].

The incident and scattered beam polarization directions can each be represented mathematically by the vectors shown below,

$$\overrightarrow{e_i} = \begin{pmatrix} \cos\phi \\ \sin\phi \\ 0 \end{pmatrix} \quad (14)$$

$$\overrightarrow{e_s} = \begin{pmatrix} \cos\eta \\ \sin\eta \\ 0 \end{pmatrix} \quad (15)$$

where $\overrightarrow{e_i}$ is the polarization direction of the incident laser beam, $\overrightarrow{e_s}$ is the polarization direction of the scattered beam, ϕ is the angle of rotation of the incident beam, and η is the angle of rotation of the analyzer. η is equal to 0° when the analyzer is in the X position and is equal to 90° when the analyzer is in the Y position.

The vectors for the terms $\overrightarrow{e_i}$ and $\overrightarrow{e_s}$ in Equation (14) and Equation (15) can be substituted into Equation (13). By setting η equal to 0° and 90° to represent the two positions of the analyzer, the two equations are simplified and the resulting equations are shown in Equation (16) and Equation (17).

$$I_{\phi x}(\phi, 0°, \alpha, \beta, \gamma) = I_0 \cdot (f_{11} \cdot \cos^2\phi + f_{12}\cos\phi\sin\phi + f_{13}\sin^2\phi) \quad (16)$$

$$I_{\phi x}(\phi, 90°, \alpha, \beta, \gamma) = I_0 \cdot (f_{13} \cdot \cos^2\phi + f_{23}\cos\phi\sin\phi + f_{33}\sin^2\phi) \quad (17)$$

where,

$$f_{11}(\alpha, \beta, \gamma) = 4 \cdot {t_{11}}^2{t_{21}}^2 + 4 \cdot {t_{11}}^2{t_{31}}^2 + 4 \cdot {t_{31}}^2{t_{21}}^2 \quad (18)$$

$$f_{12}(\alpha, \beta, \gamma) = 4 \cdot ({t_{11}}^2 t_{21}t_{22} + {t_{11}}^2 t_{31}t_{32} + {t_{21}}^2 t_{11}t_{12} + {t_{31}}^2 t_{11}t_{12} + {t_{21}}^2 t_{31}t_{32} + {t_{31}}^2 t_{21}t_{22}) \quad (19)$$

$$f_{13} = (t_{11}t_{22} + t_{12}t_{21})^2 + (t_{11}t_{32} + t_{12}t_{31})^2 + (t_{21}t_{32} + t_{22}t_{31})^2 \quad (20)$$

$$f_{23} = 4 \cdot t_{12}t_{22}(t_{11}t_{22} + t_{12}t_{21}) + 4 \cdot t_{12}t_{32}(t_{11}t_{32} + t_{12}t_{31}) + 4 \cdot t_{22}t_{32}(t_{21}t_{32} + t_{22}t_{31}) \quad (21)$$

$$f_{33} = 4 \cdot {t_{12}}^2{t_{22}}^2 + 4 \cdot {t_{12}}^2{t_{32}}^2 + 4 \cdot {t_{22}}^2{t_{32}}^2 \quad (22)$$

The t_{ij} terms represent the components of the **T** matrix given in Equation (23).

$$\mathbf{T} = \begin{bmatrix} t_{11} & t_{12} & t_{13} \\ t_{21} & t_{22} & t_{23} \\ t_{31} & t_{32} & t_{33} \end{bmatrix} = \tag{23}$$

$$\begin{bmatrix} \cos\alpha\cos\gamma - \cos\beta\sin\gamma\sin\alpha & -\cos\alpha\sin\gamma - \cos\beta\cos\gamma\sin\alpha & \sin\beta\sin\alpha \\ \sin\alpha\cos\gamma + \cos\beta\sin\gamma\cos\alpha & -\sin\alpha\sin\gamma + \cos\beta\cos\gamma\cos\alpha & -\sin\beta\cos\alpha \\ \sin\gamma\sin\beta & \cos\gamma\sin\beta & \cos\beta \end{bmatrix}$$

Note that Equation (13) and the equations for '*f*' listed in Equation (15) through Equation (21) are corrected forms of those given in the article by Becker et al. [28].

By setting the coefficient of each term in Equation (16) and Equation (17) equal to a constant, the two functions shown in Equation (24) and Equation (25) were used to fit the experimental data.

$$Fit_{\phi x} = U_1\cos^2\phi + U_2\cos\phi\sin\phi + U_3\sin^2\phi \tag{24}$$

$$Fit_{\phi x} = V_1\cos^2\phi + V_2\cos\phi\sin\phi + V_3\sin^2\phi \tag{25}$$

The experimental data (see Figure 3.16 for an example) was fit to each of the above equations using the Levenberg-Marquardt Method for solving sets of non-linear equations to determine the constants U_1, U_2, U_3, V_1, V_2 and V_3. Once $U_{1,2,3}$ and $V_{1,2,3}$ were determined, the following ratios were used to simplify the expressions and solve for α, β and γ.

$$u_1 = \frac{U_1}{U_3} = \frac{f_{11}}{f_{13}} \tag{26}$$

$$u_2 = \frac{U_2}{U_3} = \frac{f_{12}}{f_{13}} \tag{27}$$

$$v_1 = \frac{V_1}{V_3} = \frac{f_{13}}{f_{33}} \tag{28}$$

$$v_2 = \frac{V_2}{V_3} = \frac{f_{23}}{f_{33}} \tag{29}$$

Equation (26) through Equation (29) are rearranged and set equal to zero to obtain a system of nonlinear equations shown in Equation (30) through (33), which were used to solve for α, β, and γ,

$$u_1 \cdot f_{13}(\alpha,\beta,\gamma) - f_{11}(\alpha,\beta,\gamma) = 0 \quad (30)$$

$$u_2 \cdot f_{13}(\alpha,\beta,\gamma) - f_{12}(\alpha,\beta,\gamma) = 0 \quad (31)$$

$$v_1 \cdot f_{33}(\alpha,\beta,\gamma) - f_{13}(\alpha,\beta,\gamma) = 0 \quad (32)$$

$$v_2 \cdot f_{33}(\alpha,\beta,\gamma) - f_{23}(\alpha,\beta,\gamma) = 0 \quad (33)$$

The MATLAB nonlinear equation solving function, 'lsqnonlin' was used to solve the system of nonlinear equations using a least squares procedure to find the values of α, β, and γ that provided a solution with the minimum norm of the residuals. This solution procedure can yield multiple equivalent sets of α, β and γ. It is known from crystallography that for every crystal orientation denoted by a transformation matrix, there are 24 equivalent transformation matrices. This is based on symmetry. For a cubic crystal, there are 2 rotations of 120° about each of the four <111> directions, 3 rotations of 90° about each of the three <100> directions, and one rotation of 180° about each of the six <110> directions, plus the identity matrix [69]. Because the sets of α, β and γ are equivalent due to symmetry, any set may be used.

3.2.7 Determination of Polarization Settings and Calculation of Stress

Ganesan et al. [70] showed that the frequencies of the three optical phonon modes in the presence of strain can be found by solving the following equation,

$$\begin{vmatrix} p\cdot\varepsilon'_{xx} + q\cdot(\varepsilon'_{yy}+\varepsilon'_{zz}) - \lambda & 2r\cdot\varepsilon'_{xy} & 2r\cdot\varepsilon'_{xz} \\ 2r\cdot\varepsilon'_{xy} & p\cdot\varepsilon'_{yy} + q\cdot(\varepsilon'_{xx}+\varepsilon'_{zz}) - \lambda & 2r\cdot\varepsilon'_{yz} \\ 2r\cdot\varepsilon'_{xz} & 2r\cdot\varepsilon'_{yz} & p\cdot\varepsilon'_{zz} + q\cdot(\varepsilon'_{xx}+\varepsilon'_{yy}) - \lambda \end{vmatrix} = 0 \quad (34)$$

where p, q, and r are called the phonon deformation potentials. The terms p, q, and r are material constants and are provided in the Appendix. The ε'_{ij} terms are the tensor

components of strain. The eigenvalues, λ, represent the Raman frequency shifts in the presence of strain, and are determined from the following equation,

$$\lambda_{1,2,3} = (\omega_{1,2,3}^2 - \omega_0^2) = (\omega_{1,2,3} - \omega_0) \cdot (\omega_{1,2,3} + \omega_0) \approx \Delta\omega_{1,2,3} \cdot 2\omega_0 \qquad (35)$$

where $\Delta\omega_{1,2,3}$ are the frequency shifts in the strained material and ω_0 is the eigenfrequency in the unstrained material. In the absence of strain, the three optical Raman modes of Si, representing the three directions of the crystal, have an equal frequency at approximately 520.46 cm^{-1}. They are therefore degenerate. Following the procedure of Becker et al. [28], a mathematical simulation was used to separate the three optical Raman modes of Si to produce three frequency shifts, $\Delta\omega_{1,2,3}$, and solve for a stress tensor.

The mathematical simulation is employed to find three polarization settings where one phonon mode dominates the other two and therefore each of the three phonons can be separately measured. Six intensity functions are determined from Equation (13) with the previously calculated values of α, β, and γ. Three of the six are calculated with η equal to 0° while the other three are calculated with η equal to 90° using each of the three Raman tensors of Equation (11). Once the six intensity functions are calculated, intensity ratio functions are created:

$$Q_1^x(\phi) = \frac{I_1^x(\phi)}{I_2^x(\phi) + I_3^x(\phi)} \qquad (36)$$

$$Q_2^x(\phi) = \frac{I_2^x(\phi)}{I_1^x(\phi) + I_3^x(\phi)} \qquad (37)$$

$$Q_3^x(\phi) = \frac{I_3^x(\phi)}{I_1^x(\phi) + I_2^x(\phi)} \qquad (38)$$

$$Q_1^y(\phi) = \frac{I_1^y(\phi)}{I_2^y(\phi) + I_3^y(\phi)} \qquad (39)$$

$$Q_2^y(\phi) = \frac{I_2^y(\phi)}{I_1^y(\phi) + I_3^y(\phi)} \quad (40)$$

$$Q_3^y(\phi) = \frac{I_3^y(\phi)}{I_1^y(\phi) + I_2^y(\phi)} \quad (41)$$

where $I_{1,2,3}^{x,y}(\phi)$ are the intensity functions with the superscript term designating the analyzer position and the subscript term designating the three Raman tensors of Equation (11). $Q_{1,2,3}^{x,y}(\phi)$ are the ratio terms.

The six functions were plotted to determine the three polarization settings where, for each phonon, the intensity of one phonon was greater than the sum of the remaining two phonons. An example is shown in section 3.3.

In order to measure $\Delta\omega$, shown in Equation (35), a CZ mono-Si etched wafer sample was used to calibrate the system and to represent the "stress free", ω_0 case. The peak shifts for all stress measurements were calculated in reference to the Raman peak for the CZ mono-Si etched wafer sample.

Once the three peak shifts, $\Delta\omega_{1,2,3}$, were measured, the subsequent series of equations were used to solve for stress. Since at most only three phonon modes can be measured, not all components of strain can be determined. Hooke's law, in Equation (42), is used to calculate stress from strain shown in Equation (42).

$$\begin{pmatrix} \varepsilon'_{xx} \\ \varepsilon'_{yy} \\ \varepsilon'_{zz} \\ \varepsilon'_{yz} \\ \varepsilon'_{xz} \\ \varepsilon'_{xy} \end{pmatrix} = \begin{pmatrix} S_{11} & S_{12} & S_{12} & 0 & 0 & 0 \\ S_{12} & S_{11} & S_{12} & 0 & 0 & 0 \\ S_{12} & S_{12} & S_{11} & 0 & 0 & 0 \\ 0 & 0 & 0 & S_{44} & 0 & 0 \\ 0 & 0 & 0 & 0 & S_{44} & 0 \\ 0 & 0 & 0 & 0 & 0 & S_{44} \end{pmatrix} \begin{pmatrix} \sigma'_{xx} \\ \sigma'_{yy} \\ \sigma'_{zz} \\ \sigma'_{yz} \\ \sigma'_{xz} \\ \sigma'_{xy} \end{pmatrix} \quad (42)$$

The ε'_{ij} terms are the components of a strain tensor and are equal to those in Equation (34). The *S* matrix in Equation (42) is the stiffness matrix, the components of

which are material constants provided in the Appendix. The σ' values are given by the following equation,

$$\sigma' = \begin{pmatrix} \sigma'_{xx} & \tau'_{xy} & \tau'_{xz} \\ \tau'_{xy} & \sigma'_{yy} & \tau'_{yz} \\ \tau'_{xz} & \tau'_{yz} & \sigma'_{zz} \end{pmatrix} = [\mathrm{T}(\alpha,\beta,\gamma)]^{\mathrm{T}} \cdot \sigma \cdot [\mathrm{T}(\alpha,\beta,\gamma)] \quad (43)$$

where the σ matrix is given by Equation (44).

$$\sigma = \begin{pmatrix} \sigma_{xx} & \tau_{xy} & 0 \\ \tau_{xy} & \sigma_{yy} & 0 \\ 0 & 0 & \Delta_z \end{pmatrix} \quad (44)$$

The following iterative procedure is used to solve for σ_{xx}, σ_{yy} and τ_{xy} using the peak shifts, $\Delta\omega_{1,2,3}$. First, initial values are supplied for σ_{xx}, σ_{yy} and τ_{xy}. The Δ_z term is initially set to 0. The initial σ matrix values are substituted into Equation (43) with the matrix **T** to solve for σ'. The values of σ' are substituted into Equation (42) to calculate the components of strain, ε'_{ij}. The calculated values of strain can then be substituted into the matrix in Equation (34). The determinant of the matrix in Equation (34) is calculated yielding the following characteristic polynomial,

$$P(\lambda) = \lambda^3 + a\lambda^2 + b\lambda + c \quad (45)$$

where each of the coefficients *a*, *b*, and *c*, is equal to a function of σ_{xx}, σ_{yy}, τ_{xy} and Δ_z. Use of Vieta's formula [71] yields the following the three equations,

$$a(\sigma_{xx},\tau_{xy},\sigma_{yy},\Delta_z) = -2\omega_0(\Delta\omega_1 + \Delta\omega_2 + \Delta\omega_3) \quad (46)$$

$$b(\sigma_{xx},\tau_{xy},\sigma_{yy},\Delta_z) = (2\omega_0)^2(\Delta\omega_1\cdot\Delta\omega_2 + \Delta\omega_1\cdot\Delta\omega_3 + \Delta\omega \quad (47)$$

$$c(\sigma_{xx},\tau_{xy},\sigma_{yy},\Delta_z) = (2\omega_0)^3(\Delta\omega_1\cdot\Delta\omega_2\cdot\Delta\omega_3) \quad (48)$$

where *a*, *b*, and *c* are the coefficients of Equation (45), ω_0 is the frequency of the unstrained material, or the stress-free etched CZ sample used in this experiment, and

$\Delta\omega_{1,2,3}$ are the three measured frequency shifts using the three polarization settings determined earlier.

The set of equations in Equations (46) through (48) are solved for the values of σ_{xx}, σ_{yy}, τ_{xy} using the MATLAB nonlinear least squares problem solving function 'nsqnonlin' to find the solution with the minimum norm of the residuals.

The solution for σ_{xx}, σ_{yy}, τ_{xy} with Δ_z equal to zero, is then used to re-solve for the peak shifts. If any of the calculated three peak shifts differ by more than 0.08 cm^{-1} from the experimentally measured peak shifts, the Δ_z value is increased by 5 MPa and the procedure is repeated to solve for σ_{xx}, σ_{yy}, τ_{xy} and Δ_z. This iterative procedure is repeated until the difference between the experimentally measured and calculated values of the peak shifts are within 0.08 cm^{-1}.

Finally, a stress tensor is found,

$$\sigma = \begin{pmatrix} \sigma_{xx} & \tau_{xy} & 0 \\ \tau_{xy} & \sigma_{yy} & 0 \\ 0 & 0 & \Delta_z \end{pmatrix} \quad (49)$$

This stress tensor assumes a plane stress state, which is commonly used in Raman spectroscopy, as the wavelength used only penetrates the surface of the sample. The Δ_z term acts as an error term to account for the residual stress that exists in the Z laboratory coordinate direction, counter to the plane-stress assumption. For the majority of measurements calculated, Δ_z was found to be very low (less than 20 MPa) and in most cases equal to 0 MPa.

3.3 Polarized Micro-Raman Spectroscopy Experimental Validation

In order to validate the lengthy procedure of Becker et al. [28], several experiments were conducted to determine the crystal orientation and applied using Si wafer samples.

3.3.1 Crystalline Orientation

A polished semiconductor wafer of known orientation (111) was placed on the sample stage. Semiconductor wafers are manufactured with flats in standard configurations to designate crystalline orientation; <111> designates the surface normal direction while the <110> designates the direction of the wafer flat. The wafer used was n-type (111). Figure 3.17 shows the standard configurations of semiconductor grade Si wafers.

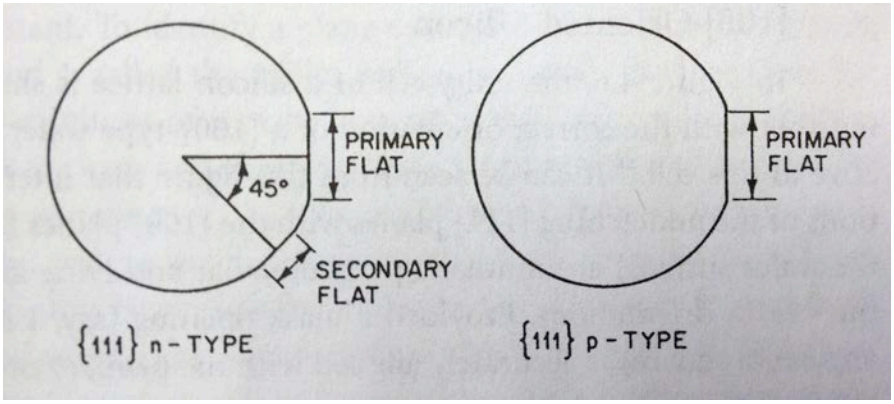

Figure 3.17: Semiconductor grade Si wafer orientation designation [72].

The wafer flat <110> direction was aligned with the laboratory “X” coordinate as shown in Figure 3.11 on the microscope sample stage. The [111] plane was placed on the stage, coplanar with the XY plane.

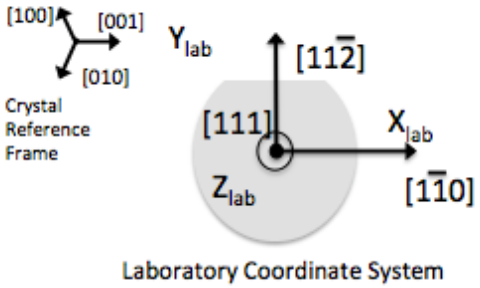

Figure 3.18: Si [111] wafer aligned with laboratory coordinate system.

The procedure described in section 3.2.6 was followed to produce both an X and a Y intensity curve as a function of the incident polarization angle, with X and Y designating the positions of the analyzer. Figure 3.19 shows both the X and Y analyzer position data along with the fitted curves.

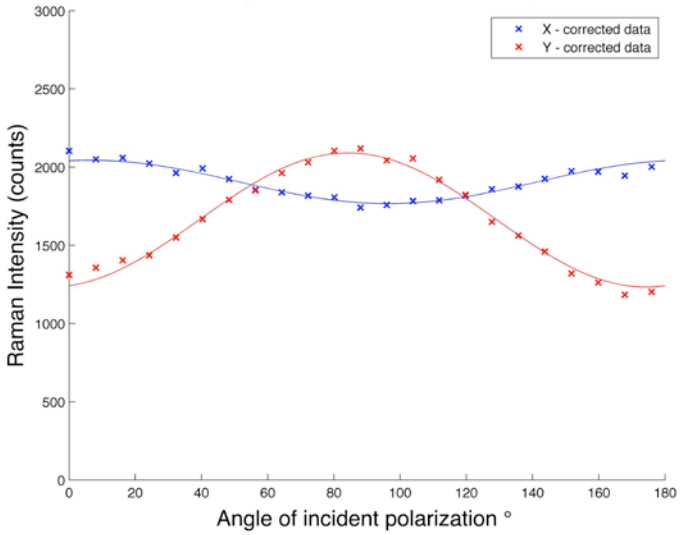

Figure 3.19: Raman intensity as a function of incident polarization angle, collected data points and fitted curves, for X and Y analyzer positions.

The Euler angles were calculated to be α = -44.6, β = -56.4, γ = 89.4. These Euler angles resulted in the following transformation matrix:

$$T_{exp.} = \begin{bmatrix} 0.40 & -0.71 & 0.59 \\ 0.39 & 0.71 & 0.59 \\ -0.83 & 0 & 0.55 \end{bmatrix} \quad (50)$$

The theoretical transformation matrix can be calculated from the known Miller indices of the surface normal and the direction of the wafer flat, assuming the flat is aligned with the X axis of the laboratory reference frame. There are 24 equivalent sets of Euler angles to describe every crystalline orientation. Therefore, it is easier to compare the transformation matrices instead of Euler angles for validation of theory to experiment. The theoretical transformation matrix using Euler angles for a [111] sample on the sample stage is as follows:

$$T_{theory} = \begin{bmatrix} 0.41 & -0.71 & 0.58 \\ 0.41 & 0.71 & 0.58 \\ -0.82 & 0 & 0.58 \end{bmatrix} \quad (51)$$

The theoretical transformation matrix in Equation (51) agreed very well with the experimental result given in Equation (50). The error between the experimentally measured and theoretical transformation matrices was less than 3°.

3.3.2 Stress Validation using Bending Experiment

To validate the stress measurements generated by polarized micro-Raman spectroscopy, a CZ mono-Si (100) wafer was cut into a 10 mm x 120 mm x 0.19 mm beam. The beam was manually bent and its edges were inserted in the lid of a shallow transparent box with sides less than the beam length resulting in a bending moment and corresponding stress in the beam. Figure 3.20 shows a diagram of the beam specimen in its unstressed and applied stress states.

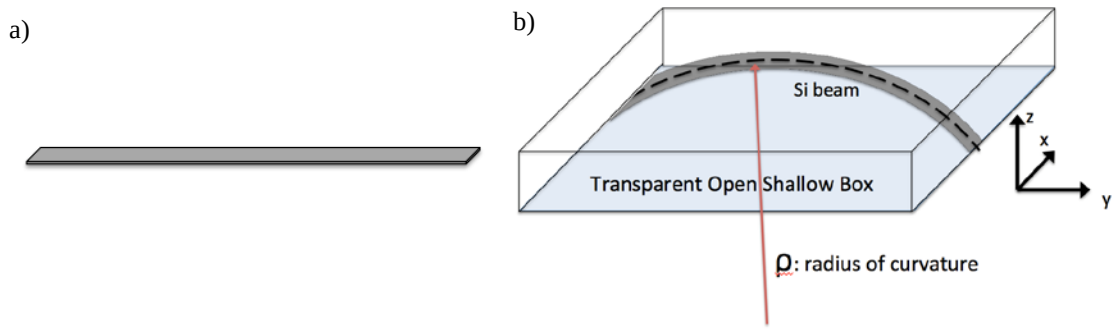

Figure 3.20: (a) Si beam, no applied stress. (b) Si beam, applied stress.

The region investigated was at the point of maximum deflection, shown by the highest point of the beam in Figure 3.20. ρ in Figure 3.20 is the radius of curvature of the bent Si beam.

Prior to placing the mono-Si beam in the stressed state, the orientation was measured. The theoretical and experimental transformation matrices for the (100) wafer beam are shown in Equations (52) and (53).

$$T_{(100)_{Theory}} = \begin{bmatrix} 0 & -1 & 0 \\ 1 & 0 & 0 \\ 0 & 0 & 1 \end{bmatrix} \quad (52)$$

$$T_{(100)_{Exp.}} = \begin{bmatrix} 0.06 & -0.98 & 0.18 \\ 1 & 0.03 & -0.12 \\ 0.12 & 0.19 & 0.97 \end{bmatrix} \quad (53)$$

The experiment and theory yielded very similar transformation matrices. The results of the mathematical simulation used to find the polarization settings to separate the phonon peak shifts are shown in Figure 3.21 and Figure 3.22.

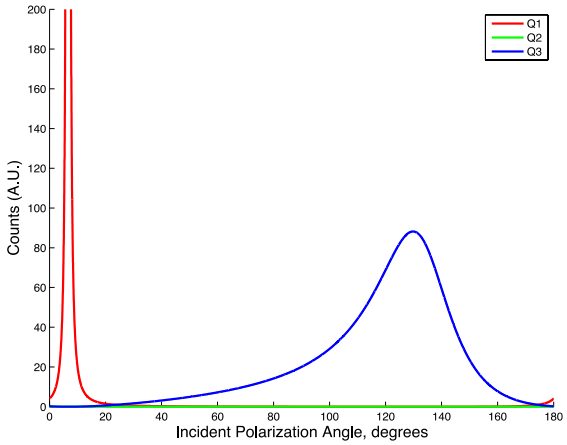

Figure 3.21: Analyzer in 'Y' position, mathematical simulation to separate the phonons for peak shift measurements.

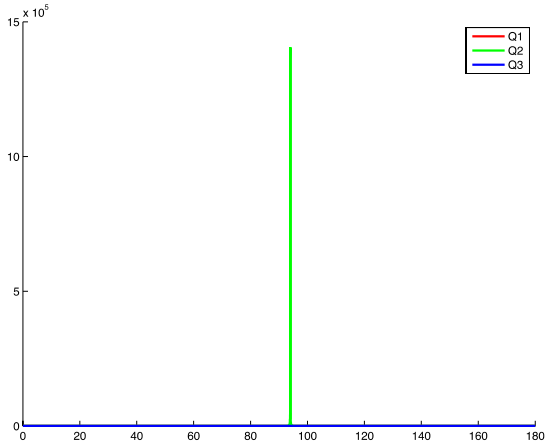

Figure 3.22: Analyzer in 'X' position, mathematical simulation to separate the phonons for peak shift measurements.

The polarization settings were determined to be as follows: Y analyzer position, 3° incident polarization angle, X 47°, and Y 65°. The angles are equal to ½ the angles shown in Figure 3.21 and Figure 3.22 since a half-wave plate rotates the incident beam two times the rotated angle of the half-wave plate.

To validate the applied stress measurements, first the stress tensor was measured with the beam flat on the microscope stage surface. Following this step, the beam was bent using the box lid to apply an equal moment on both ends of the beam and the stress

state was measured again. The peak shifts, $\Delta\omega_{1,2,3}$, used to calculate the stressed state were measured using the unstressed beam Raman peak to represent ω_0 as the "stress-free" case. This removed the influence of pre-existing residual stress in the beam and allowed for calculation of only the difference in stress due to the applied load. A 25µm x 25µm region of the beam surface was measured at 5µm intervals. This resulted in 25 measurements per peak shift, which were averaged to find the stress at the surface. The resulting average stress tensor is shown in Equation (54).

$$\sigma = \begin{bmatrix} 76 & 0.5 & 0 \\ 0.5 & 102 & 0 \\ 0 & 0 & 0 \end{bmatrix} \qquad (54)$$

Since micro-Raman spectroscopy is a surface measurement technique, only the top surface of the beam, above the neutral axis was investigated. See Figure 3.23.

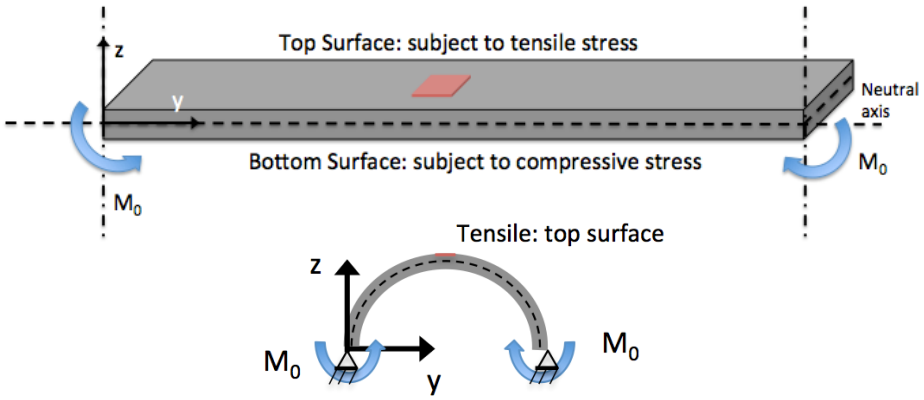

Figure 3.23: Applied stress experiment. Top: no moment applied. Bottom: moment applied to produce stress state. Neutral axis, moment applied, and surface subject to tensile stress are shown.

The stress components σ_{xx} = 76 MPa and σ_{yy} = 102 MPa were both tensile on the top surface of the beam, as expected from theory. Euler-Bernoulli beam theory was used to calculate the theoretical maximum stress at the surface of the beam. Although Si is not an isotropic linear material, the assumption is often used for validation purposes and

works well in many cases. In order to measure the radius of curvature of the bent beam, a photograph of the beam in the stressed state was taken and the radius of curvature was found by fitting a circle to the bent beam shape. The circle was used to find the radius of curvature. The moment curvature equation,

$$\kappa = \frac{1}{\rho} = \frac{M}{EI} \qquad (55)$$

was used to solve for the moment applied, where *E* is the modulus of Elasticity and *I* is the moment of inertia. The moment, *M* was substituted into the flexure formula,

$$\sigma_{yy} = -\frac{Mz}{I} \qquad (56)$$

where *z* is the vertical distance from the neutral axis to the point of interest. Substituting the moment, *M,* of Equation (55) into Equation (56) results in the equation,

$$\sigma_{yy} = -\frac{Ez}{\rho} \qquad (57)$$

where the radius of curvature, ρ, was equal to 180 mm and *z* was equal to one half the thickness of the beam, 90μm. *E*, the Modulus of Elasticity used for Si was 169 GPa [73]. Table 3.1 shows the difference between the theoretical and experimentally determined stress results for the bent beam.

Table 3.1: Comparison of theory and experiment; (100) Si beam.

	Theory	Experiment
σ_{xx}	~ 0 MPa	76 MPa
σ_{yy}	95 MPa	102 MPa

Although the experimental results matched theory on an order of magnitude basis, the high value of σ_{xx} = 76 MPa was not expected as all the applied load by bending was in the σ_{yy} direction of the beam. The above results are hypothesized to be due to the high likelihood of torsion occurring when the wafer was bent in the experimental setup.

However, the σ_{yy} component of stress matched very well with theory and serves to validate the stress measurement technique.

3.4 Comparison of Near-infrared Birefringence Polariscopy and Polarized Micro-Raman Spectroscopy Techniques to Measure Residual Stress

Both near-infrared birefringence polariscopy and polarized micro-Raman spectroscopy use the same fundamental principles of the effect of a medium on an electromagnetic wave to measure residual stress. Numerous texts show the relationship between susceptibility, χ, and the index of refraction, n, as well as the dielectric constant, commonly represented by ε. As discussed in sections 3.1.1 and 3.2.1, the near-infrared birefringence polariscope uses the index of refraction, n, for its calculations while micro-Raman spectroscopy uses phonon deformation potentials derived from the susceptibility, χ, of Si. Engineering applications tend to use the index of refraction, n, while physicists prefer to use the dielectric constant, ε, or the susceptibility, χ [74]. The simplest form of the refractive index can be defined as

$$n = \sqrt{\varepsilon} = \sqrt{\chi + 1} \qquad (58)$$

However, derivations and theory both show the susceptibility, χ, and index of refraction, n, to be complex with both real and imaginary parts and demonstrate the same behaviors of light interaction with a medium [74].

The primary experimental differences between the polarized micro-Raman spectroscopy technique and the near-infrared birefringence polariscope used in this thesis for the measurement of stress are:

1. Spatial resolution

    Polariscope: 17μm at best.

Micro-Raman spectroscopy: 1.5μm/laser spot size

2. Sample volume probed:

Polariscope: *Average* through-thickness measurement

Micro-Raman spectroscopy: Surface measurement (~0.6μm depth)

3. Stress components evaluated

Polariscope: Maximum shear stress: $\tau_{\max=} \frac{|\sigma_1-\sigma_2|}{2}$

Micro-Raman spectroscopy: Stress tensor consisting of σ_{xx}, σ_{yy}, and τ_{xy}; can be used to calculate τ_{max}.

3.5 Summary

The objective of this chapter is to provide a description of the fundamental physical principles behind the measurement of residual stress using near-infrared birefringence polariscopy and polarized micro-Raman spectroscopy. Both techniques use the interaction of light with a medium to determine stress and can be applied to crystalline Si. In addition, this chapter aimed to explain the experimental set-up, methods, and analysis used to give a comprehensive understanding of the results ascertained in the experiments conducted as part of this research, which are described in subsequent chapters. The mathematical and experimental procedure used for polarized micro-Raman spectroscopy experiments was validated experimentally using Si wafers of known crystalline orientation and applied stress states. The conclusions drawn from this chapter are as follows:

- The near-infrared birefringence polariscope provides measurements of maximum shear residual stress, τ_{max}, averaged through the wafer thickness while polarized

micro-Raman spectroscopy gives a plane-stress assumption stress tensor of the 0.5μm of the surface of the Si wafer sampled.

- The polarized micro-Raman technique detailed by Becker et al. [28] was successfully experimentally validated at Georgia Tech both for the measurement of Si crystalline orientation in relation to the laboratory coordinate frame, and for the measurement of stress in Si wafer samples.

CHAPTER 4
THE EFFECT OF WIRE SAWING AND CASTING ON THE RESIDUAL STRESS IN mc-SI WAFERS

Chapter 3 explained the fundamental physical principles and the experimental methods used for the two residual stress measurement techniques: near-infrared birefringence polariscopy and polarized micro-Raman spectroscopy. These two techniques will be used in the experiments detailed in this chapter to investigate residual stress in mc-Si wafers.

First, the research question addressed in this chapter will be stated. The subsequent sections will describe two experiments, which were used to quantify the contributions of residual stress from wire sawing and from the thermal gradients produced during casting and solidification of mc-Si ingots. The first experiment is designed to study saw damage induced residual stress using the near-infrared birefringence polariscope. The second experiment makes use of the polariscope and the polarized micro-Raman spectroscope to investigate residual stresses generated by both wire sawing and by the thermal gradient produced during casting of mc-Si ingots.

For each experiment, a process flow diagram of the procedure is shown and the methods are explained in detail. In addition, the results of each study are presented and discussed. This chapter concludes by comparing the results of the two measurement techniques and by presenting the scientific conclusions from the investigation.

4.1 Research Objective

As explained in Chapter 1, the first objective of this thesis is to investigate the contribution of residual stress generated by wire sawing and the contribution of residual stress generated by the thermal gradient produced during casting and solidification of mc-Si ingots. The influences of the two wire sawing processes, DWS and LAWS, are examined individually to quantify their respective contributions to residual stress in mc-Si wafers. In addition, the residual stress fields near grain boundaries and within the grains are analyzed.

4.2 Experimental Outline

Two experiments were designed to meet the research objectives. The first experiment, which is referred to as “Experiment 1”, was designed with the intent to study residual stress solely within the first 12μm of the saw damage layer. The second experiment, labeled “Experiment 2”, was designed to delineate the contribution of residual stress caused by saw damage and the contribution of residual stress caused by the thermal gradient produced during mc-Si ingot solidification. Experiment 2 examined the first 40μm of the silicon wafer surface. Multi-crystalline Si wafers were used for both experiments as they are presently the most widely-used solar cell substrate material. Furthermore, the many grain orientations of mc-Si wafers are known to influence both saw damage and thermal gradient induced residual stress and are therefore of scientific interest. Table 4.1 summarizes the two experiments side-by-side.

Table 4.1: Summary of Experiment 1 and Experiment 2.

	Experiment 1	**Experiment 2**
Research Question	Contribution of saw damage to residual stress	Contributions of saw damage and thermal gradient during mc-Si casting to residual stress
Wafer Samples	mc-Si DWS mc-Si LAWS	mc-Si DWS mc-Si LAWS
Characterization Techniques	• Near-infrared birefringence polariscope (residual stress) • Non-contact profilometer (surface roughness)	• Near-infrared birefringence polariscope (residual stress) • Polarized micro-Raman spectroscopy (residual stress)
Depth of Sample Probed	0µm - 12µm	0µm - 40µm
Sawing Process	DWS LAWS	DWS LAWS
Microstructural Features Studied	grain and grain boundary	grain and grain boundary

4.2.1 Experiment 1: Study of the Saw Damage Layer

Experiment 1 was designed with the goal of studying the residual stress in the top 12µm of the saw damage layer. A process flow diagram of the experimental approach is shown in Figure 4.1.

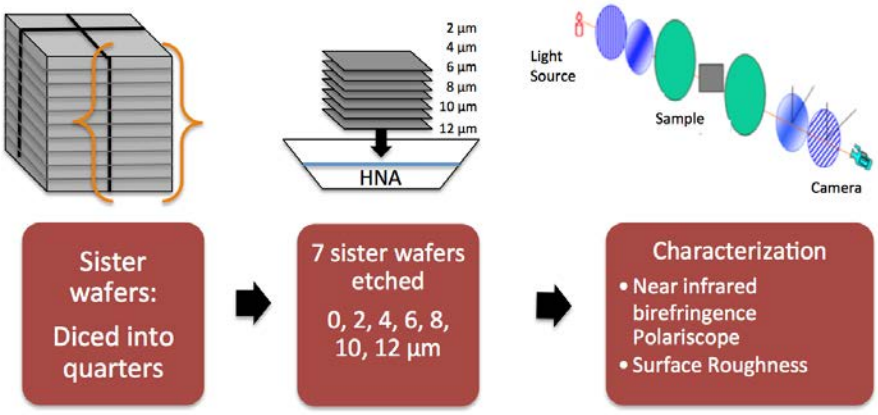

Figure 4.1: Experiment 1 process flow.

Multi-crystalline Si “sister wafers” of each sawing process type, DWS and LAWS, were first diced into quarters to facilitate handling and to allow for replication of experiments, if needed. Sister wafers are adjacent wafers taken from the same brick of the same ingot and can therefore be assumed to possess similar wire-sawing induced residual stress and similar thermal gradient induced residual stress resulting from the mc-Si ingot solidification process.

Seven sister DWS wafers and seven sister LAWS wafers were etched using wet chemical isotropic etching to obtain residual stress data for each of the following etch depths: 0, 2, 4, 6, 8, 10, and 12μm. Both sides of the wafers were etched to the same depth in each case i.e. for the 12μm etch depth case, 24μm of material was removed -- 12μm from each side of the Si wafer. For consistency, in this thesis, the term “etch depth” always refers to the depth removed from one side the wafer.

Wet Chemical Isotropic Etching

HNA ($HF:HNO_3:CH_3COOH$) (9:75:17) [75] was used as the wet chemical isotropic etchant to remove Si uniformly from both sides of the wafer. The compositions of the chemicals used were: 49% Hydrofluoric acid (HF), 69-70% Nitric acid (HNO_3) and >99% Acetic acid (CH_3COOH). HNA is an isotropic etchant meaning it etches all Si crystalline orientations at the same etch rate unlike other industrially used Si etchants, which etch different crystalline orientations anisotropically at different etch rates. Near-infrared birefringence polariscopy is dependent on the sample thickness for stress measurement, therefore an isotropic etchant was required to ensure a uniform thickness of the mc-Si wafers.

The etch rate using HNA was approximately 5μm/minute to produce a planar isotropic etch. The etch stop time was adjusted accordingly for each etch depth between 0μm to 12μm at 2μm intervals. The wafers were placed individually in a sample holder and submerged horizontally in the HNA bath. The sample holder prevented contact of the wafer with the bottom of the bath. Slight manual agitation was applied during etching to produce even Si removal. Due to incidental differences in agitation between the bottom and top of the bath, the wafers were inverted halfway through the total etch time. After etching, the wafers were immediately placed into two successive deionized water (DI H_2O) baths for 5 minutes each, rinsed with DI H_2O, and dried completely using nitrogen (N_2) gas.

To confirm that the correct etch depths were reached for each of the sister wafers, Apiezon Black Wax W was used as a mask to allow measurement of the original height of the wafer surface compared to the etched surface. Prior to etching, Apiezon Black Wax W was deposited on both sides of each wafer in a small area. The areas masked were less than 1 cm^2. Apiezon Black Wax W is resistant to HF and acts as an etch resist for Si. It can easily be removed with the use of hydrocarbons such as trichloroethylene (C_2HCl_3). After etching, the Apiezon Black W wax was removed with heat and C_2HCl_3. A stylus profilometer (KLA Tencor Alpha-Step IQ Surface Profiler) was used to measure the "step" or height difference between the area previously masked and the etched areas. This procedure provided validation that the correct depth measured from the original wafer surface was reached in each case of etching. Figure 4.2 shows schematics of the masking and the step height measurement procedures for one side of the wafer.

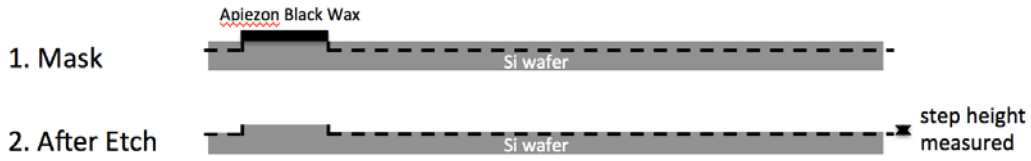

Figure 4.2: Wet chemical etching process using Apiezon Black Wax W.

In addition to using a mask to aid in the determination of the etch depth, the wafers were weighed using a Mettler Toledo scale (Model#: AB104) before and after etching. The thickness of the Si wafer was calculated before and after etching using the following formula,

$$t = \frac{m}{\rho l w} \tag{59}$$

where t is the thickness of the Si wafer, m is the measured weight of the Si wafer in grams, ρ is the density of Si, 2.33 g/cm^3 [76], and l and w are the length and width of the wafer, respectively. In the case of the diced Si wafer quarters used in this experiment, l and w were both equal to 7.8 cm, which is one-half the length of the 15.6 cm x 15.6 cm Si wafers.

Characterization

After etching to the pre-determined etch depths, all the wafers were analyzed using the near-infrared birefringence polariscope to calculate the through-thickness maximum residual shear stress, τ_{max}. In addition, a Taylor Hobson TalySurf CCI non-contact optical profilometer at the Advanced Remanufacturing and Technology Center (ARTC) in Singapore, in partnership with Nanyang Technological University (NTU) in Singapore was used. The Taylor Hobson TalySurf CCI non-contact optical profilometer

provided maps of the surface morphology of the wafers in the vicinity of the grain boundaries. This data aided in the understanding of the effect of etching on wafer surface morphology and provided knowledge complementary to the research objective.

As stated in Chapter 3, the near-infrared birefringence polariscope is a through-thickness measurement method that yields the through-thickness maximum residual shear stress, τ_{max} [59]. The polariscope enables the calculation of τ_{max} using the stress optic law,

$$\tau_{max} = |\sigma_1 - \sigma_2| = \frac{\lambda\delta}{2\pi tC} \quad (60)$$

where σ_1 and σ_2 are the principal stresses, λ is the wavelength of light used, δ is the retardation of light through the sample, t is the thickness of the sample, and C is the relative stress optic coefficient. For each point in the wafer, τ_{max} was calculated to generate a full-field residual stress map.

The Taylor Hobson TalySurf CCi non-contact optical profilometer uses a high-speed 1 mega pixel camera with 1/10 Ångstrom vertical resolution to create 3D surface maps. In a location near the grain boundaries, 3D maps were created using the optical profilometer and the average surface roughness, S_a, as a function of etch depth were calculated for the sister wafer samples. The roughness data provided topographical evidence of saw damage as a function of the etch depth.

4.2.2 Experiment 2: Study of the Saw Damage Layer and Thermal Gradient Stress

Experiment 2 was designed to delineate the residual stress produced by saw damage from the residual stress produced by the thermal gradient during mc-Si ingot solidification. Studies of the saw damage depth in DWS mc-Si wafers have recorded micro-cracks of lengths up to 12μm into the depth of the wafer [30]. A study by Möller et al. [3] found that the micro-cracks extend from the surface into the wafer and typical

micro-crack lengths for mc-Si LAWS wafers range from 10µm to 15µm. Based on these findings, it was determined that at an etch depth of 40µm, all damage due to the sawing process should be removed from the wafer surface, and at this depth, the residual stress can be assumed to be solely representative of the residual stress produced by the thermal gradients present during casting of the mc-Si ingot. A process flow diagram demonstrating the approach used in Experiment 2 is shown in Figure 4.3.

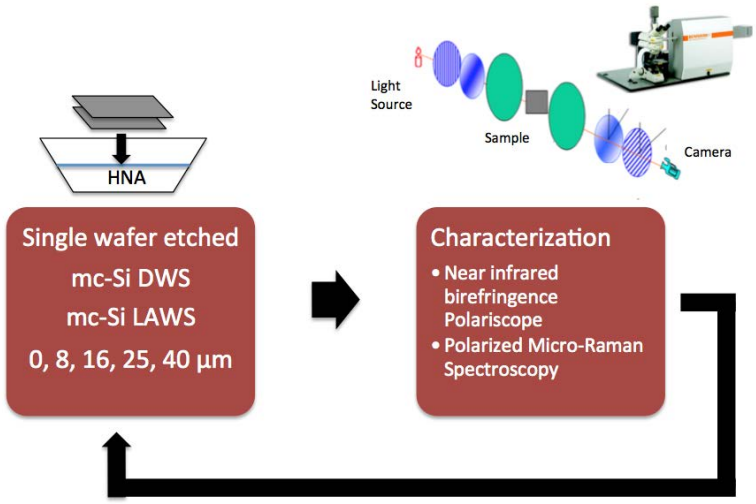

Figure 4.3: Experiment 2 process flow.

Single wafers were used for this experiment instead of sister wafers to reduce any possible variation between the sister samples. A single mc-Si DWS and a single mc-Si LAWS wafer was used in each case.

The same etching procedure described in Section 4.2.1 was used for Experiment 2. Instead of the 2µm etch depth intervals used in Experiment 1, each wafer (one DWS and one LAWS) was etched progressively to the following etch depths: 0, 0.5, 8, 16, 25, and 40µm.

At each etch depth, both near-infrared birefringence polariscopy and polarized micro-Raman spectroscopy were used to determine the through-thickness residual stress

and in specific localized regions of the wafer surface, respectively. Near-infrared birefringence polariscopy resulted in a through-thickness τ_{max} residual stress map with a spatial resolution of 17μm/pixel while polarized micro-Raman spectroscopy gave a stress tensor for each localized wafer surface area studied. The benefit of polarized micro-Raman spectroscopy is its ability to tell the stress state, i.e. tensile or compressive, at the wafer surface. The 488 nm wavelength used for the polarized micro-Raman spectroscopy measurements extends approximately 0.5μm into the sample surface. The spatial resolution of the polarized micro-Raman spectrometer was 1.5μm using a 50X objective. The experimental set-up and method are described in Chapter 3, section 3.3. All spectral peak shifts for the Raman stress measurements were measured in reference to an etched CZ mono-Si wafer sample, which was assumed to represent a "stress-free" case.

At 0μm etch depth, the rough and highly amorphous surfaces present in the LAWS and DWS wafers created some scatter in the micro-Raman spectra. Therefore, the micro-Raman spectroscopy measurements began at a 0.5μm etch depth while the near infrared birefringence polariscope was able to collect measurements at all etch depths. The 0.5μm etch depth for the polarized micro-Raman spectroscopy measurements is assumed to be representative of the as-sawn un-etched wafer surface.

4.3 Results

4.3.1 Experiment 1: The Saw Damage Layer

Residual Stress: τ_{max}

Experiment 1 yielded very interesting results for the maximum residual shear stress, τ_{max}, in the first 12μm of surface damage for both sawing process types. Two

regions with grain boundaries were selected to show the differences between τ_{max} in DWS and LAWS. The locations selected are shown in Figure 4.4.

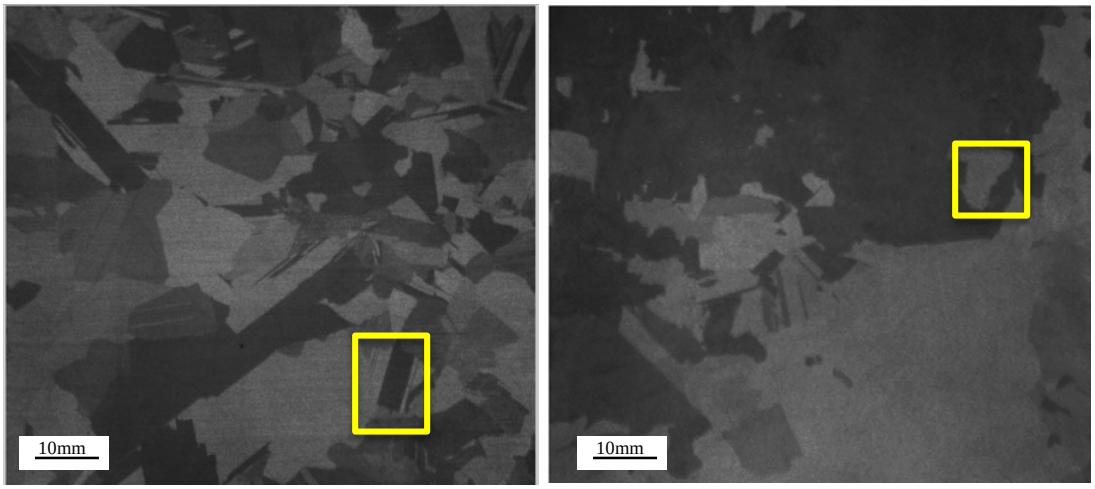

Figure 4.4: Locations selected for analysis from near-infrared transmission images of 78 mm x 78 mm diced mc-Si wafers. DWS (left) and LAWS (right).

A threshold of 25 MPa was selected to identify the points of highest τ_{max} at the as-sawn 0µm etch depth and at depths between 0µm and 12µm. Figure 4.4 shows points of τ_{max} greater than 25 MPa superimposed on the near-infrared transmission images to highlight the spatial distribution of τ_{max} above this threshold.

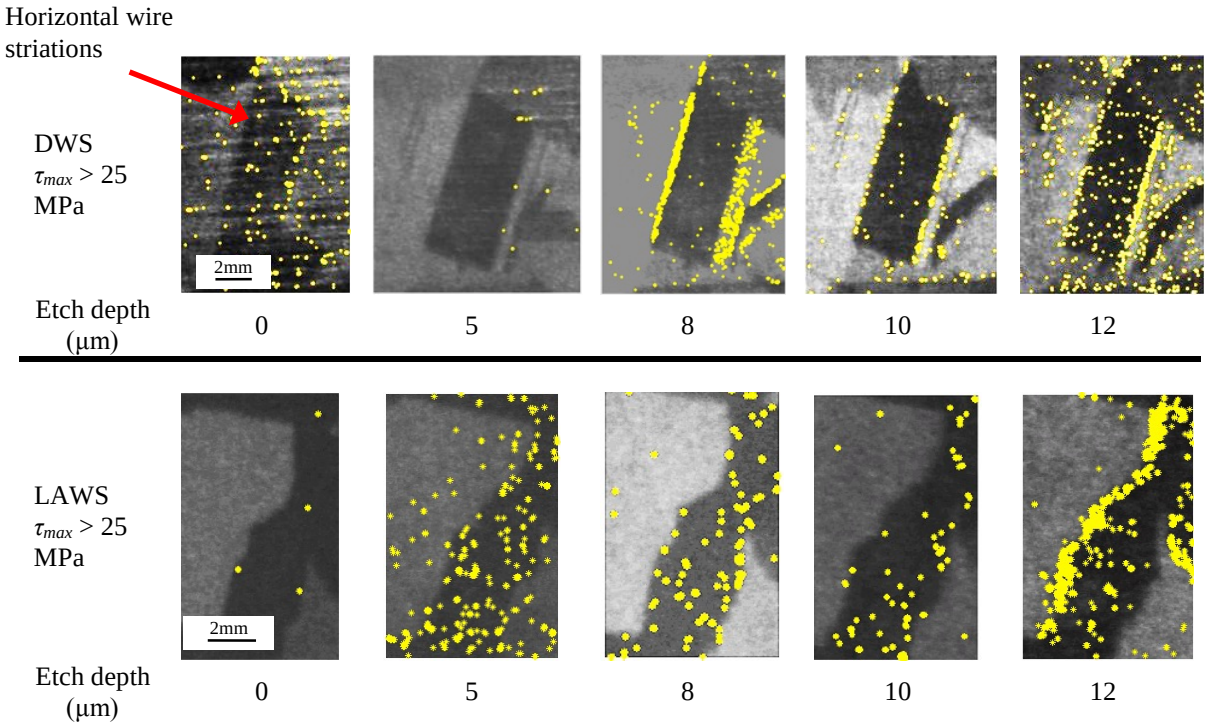

Figure 4.5: Top row: near-infrared transmission images of selected DWS region with τ_{max} > 25 MPa at increasing etch depths. Bottom row: near-infrared transmission images of LAWS region with τ_{max} > 25 MPa at increasing etch depths.

A comparison of the as-sawn, 0μm etch depth, cases (Figure 4.5) of the DWS and LAWS regions showed that DWS generated a larger number of points with τ_{max} greater than 25 MPa through the wafer thickness compared to LAWS. In the DWS as-cut wafer, all points of highest τ_{max} were predominantly aligned with the wire striation lines in the direction of wire travel. LAWS resulted in random locations of τ_{max} greater than 25 MPa; the locations were not aligned with a particular direction. This suggests that the points of high residual stress in DWS wafers are localized along the wire saw marks while they are randomly distributed in the LAWS wafers, which is consistent with the random rolling-indentation processes of material removal characteristic of the LAWS process.

Points of τ_{max} greater than 25 MPa are localized along grain boundaries beginning with the 8μm etch depth for DWS and with the 12μm etch depth for LAWS. The trend of high τ_{max} along grain boundaries can be intuitively deduced to be the product of the thermal gradient in the solidification process during mc-Si casting. This observation implies that the thermal gradient induced residual stress dominates the through-thickness τ_{max} in the DWS wafer at a shallower etch depth than in the LAWS wafer. For the 12μm etch depth, points of τ_{max} greater than 25 MPa were localized along the grain boundaries in both the DWS and LAWS wafers, showing similar trends. The number of points and the locations of τ_{max} along the grain boundaries changed from 8 to the 12μm etch depth. This finding implies that grain boundary stresses are inhomogeneous and can vary significantly through the wafer thickness, even at intervals of 2μm. Figure 4.6 shows the full field τ_{max} residual stress maps for the etch depths of 0μm, 8μm, and 12μm in the same regions shown in Figure 4.5.

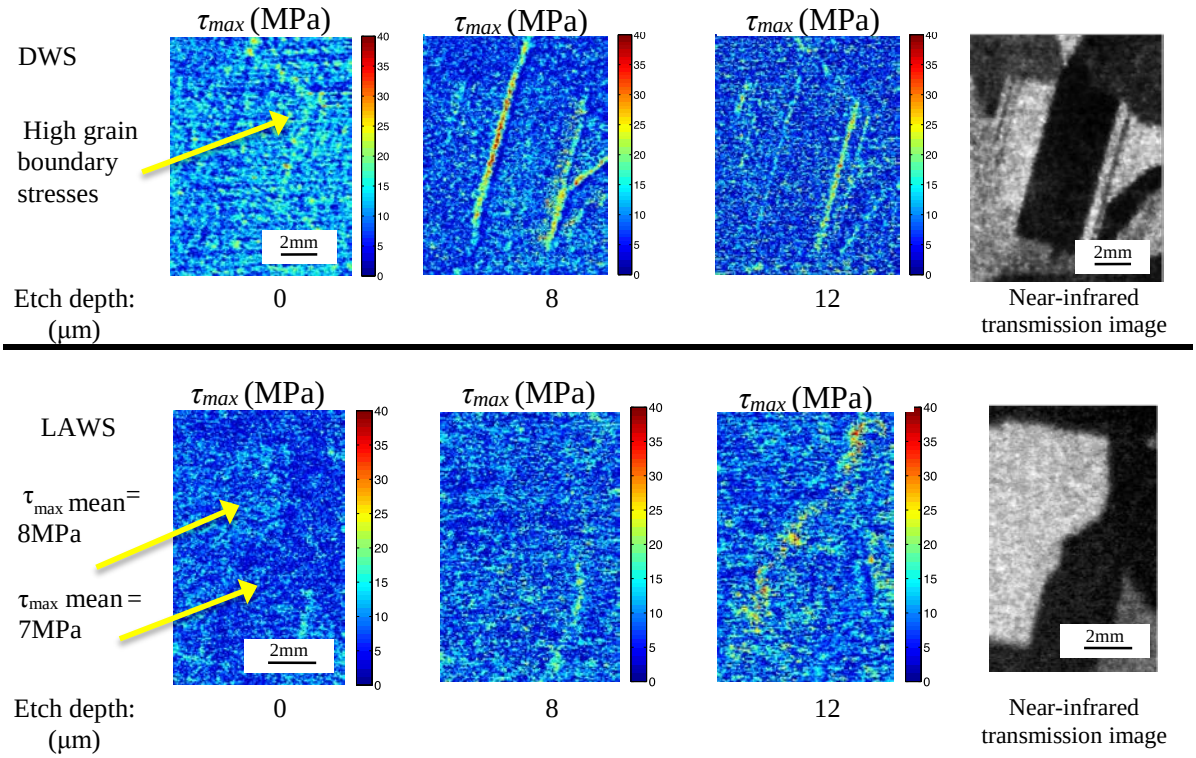

Figure 4.6: Full-field residual stress maps showing τ_{max} for the same regions shown in Figure 4.5. Top: DWS at 0, 8, and 12μm etch depths. Bottom: LAWS at 0, 8, and 12μm etch depths. The images in the rightmost column are the near-infrared transmission images showing the grain structure in these regions in order to identify the grain boundaries and grain locations.

It is interesting to note the differences in τ_{max} between the DWS and LAWS wafers for the as-sawn 0μm etch depth shown in Figure 4.6**.** DWS resulted in points of very high τ_{max} at the grain boundaries, differentiating the grain boundary from the grain. In the LAWS wafer, the two different grains examined possessed two different mean values of τ_{max} and high τ_{max} was not present at the grain boundary. The grain on the left had a mean value of 8 MPa while the grain on the right had a mean value of 7 MPa.

Figure 4.7 shows the effects of DWS and LAWS on the grain and grain boundary stresses over larger regions of the as-sawn wafers.

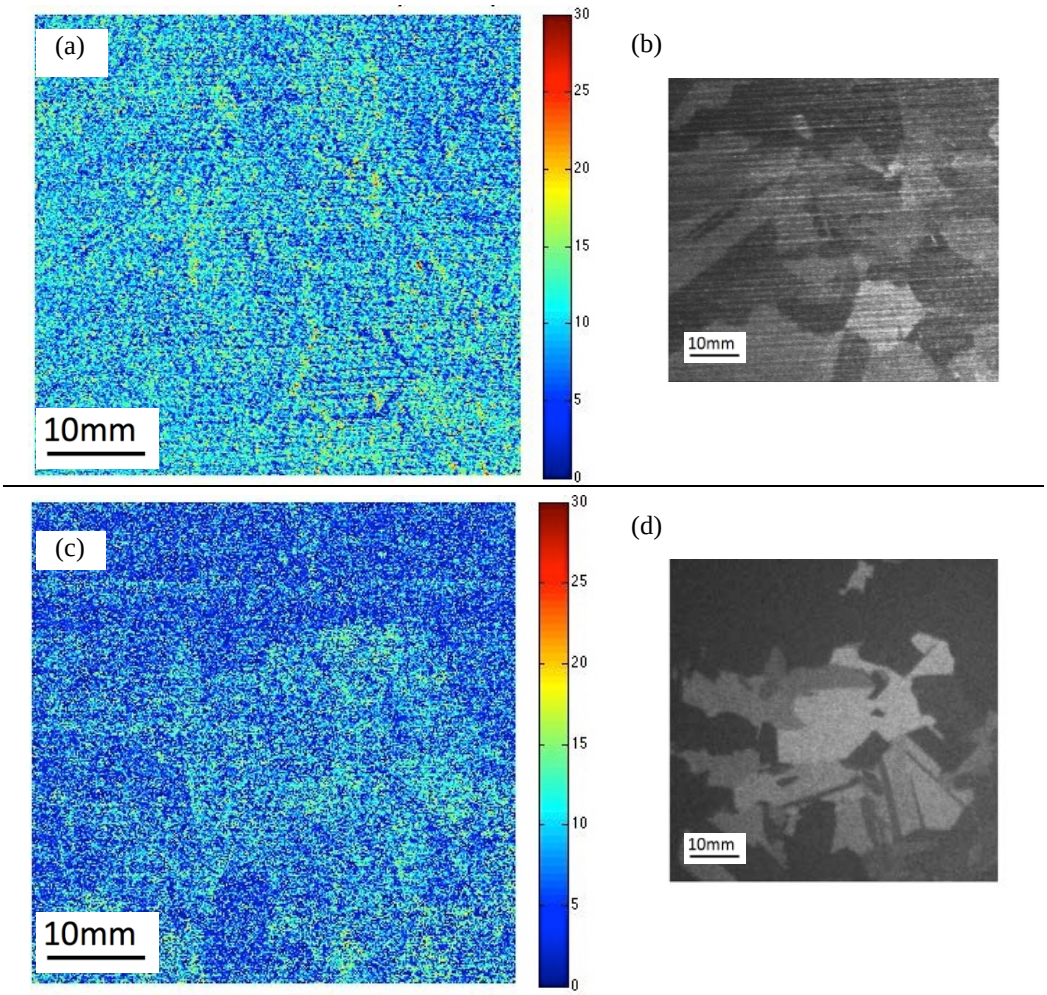

Figure 4.7: τ_{max} maps of as-cut wafers; (a) and (b) show results for the DWS wafer; (c) and (d) show results for the LAWS wafer; (a) τ_{max} map for region of the DWS wafer, (b) near-infrared transmission image of the area shown in (a), (c) τ_{max} map for region of LAWS wafer, (d) near-infrared transmission image of the area shown in (c).

The τ_{max} maps of Figure 4.7 show the variations between the two sawing process types more clearly over a larger region of the wafers, which reveal many grains and grain boundaries. The LAWS wafer clearly shows the τ_{max} differences between the grains. Some of the grain structure seen in the near-infrared transmission image shown Figure 4.7d can be seen in the τ_{max} map in Figure 4.7c. Some grains have lower average τ_{max} than others. In contrast, the DWS wafer is characterized by a pattern of lines with similar τ_{max} along the wire striation lines and obvious differences from grain-to-grain are not seen like

in the LAWS wafer. To summarize, LAWS produces different mean τ_{max} stresses depending on the grain orientation. In contrast, DWS produces mean τ_{max} stress independent of the grain orientation. However, in the DWS wafer, some grain boundaries are seen to have very low τ_{max} stress (0-5 MPa) while others have high τ_{max} stress (20-25 MPa). An example of this is shown in Figure 4.8.

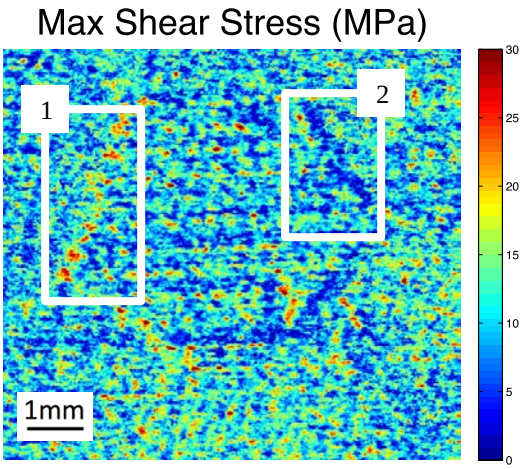

Figure 4.8: τ_{max} map of DWS as-cut wafer region. The white boxes show two grain boundaries of the same grain, one with high τ_{max} (1) and one with low τ_{max} (2).

The white boxes in Figure 4.8 highlight two grain boundaries of the same grain that are opposite each other, one with predominately high τ_{max} (Box 1) and one with low τ_{max} (Box 2). It can be concluded from this observation that either higher or lower τ_{max} can be produced at grain boundaries compared to the residual stress within the grains depending on the direction of the abrasive wire relative to the orientation of the grain boundary. Further investigations are needed to study the effect of sawing direction on the residual stress produced at small angle and large angle grain boundaries.

Surface Roughness and Surface Morphology

Figure 4.9 shows the 3D surface roughness maps of the as-cut LAWS and DWS wafers.

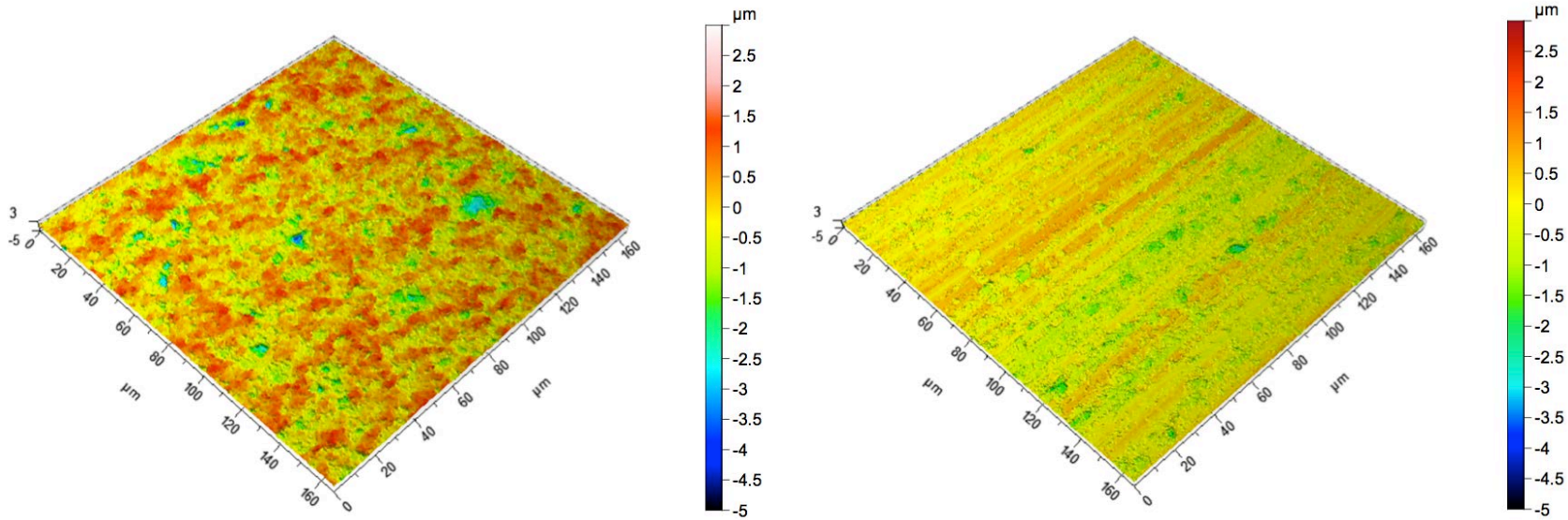

Figure 4.9: As-cut (0µm etch depth) surface morphology of the LAWS (right) and DWS (left) wafers.

The morphology of the LAWS surface is characterized by extensive pitting. The surface is a product of the rolling-indenting material removal mechanism of the LAWS process. The abrasion caused by loose, rolling, SiC particles in the LAWS slurry mix results in a uniform non-directional surface characterized by random large pits where Si is chipped and fractured. In contrast, the scratching-indenting process of DWS results in wire striation lines, and random pits along these lines where Si chipped and brittle fracture occurred.

Figure 4.10 shows a plot of the three-dimensional average surface roughness height parameter (S_a) as a function of the etch depth for both LAWS and DWS wafers.

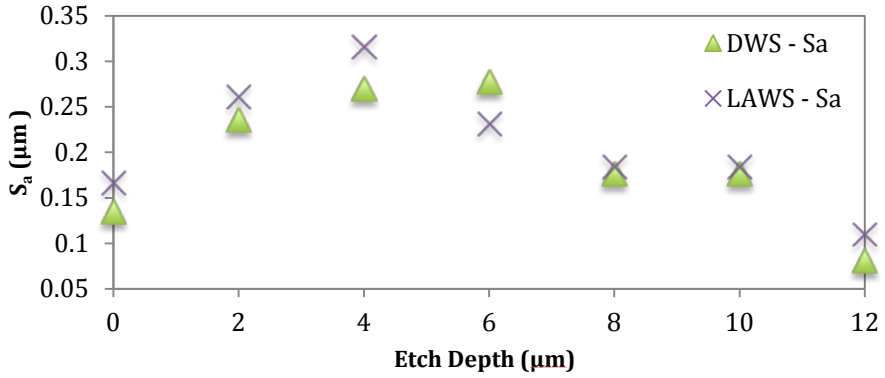

Figure 4.10: Surface roughness (S_a) as a function of etch depth for LAWS and DWS wafers.

For the 0µm etch depth, the as-cut average surface roughness of the LAWS wafer is greater than the DWS wafer. Chemical etching enlarged the micro-cracks initially present on the surface and increased the S_a values at shallow etch depths (0-8µm). For the 12µm etch depth, the surface is more planar and the S_a values decreased to 0.11µm for LAWS and .08µm for DWS.

Figure 4.11 shows 3D surface maps of the surface morphology of DWS and LAWS wafers at 8μm and 12μm etch depths.

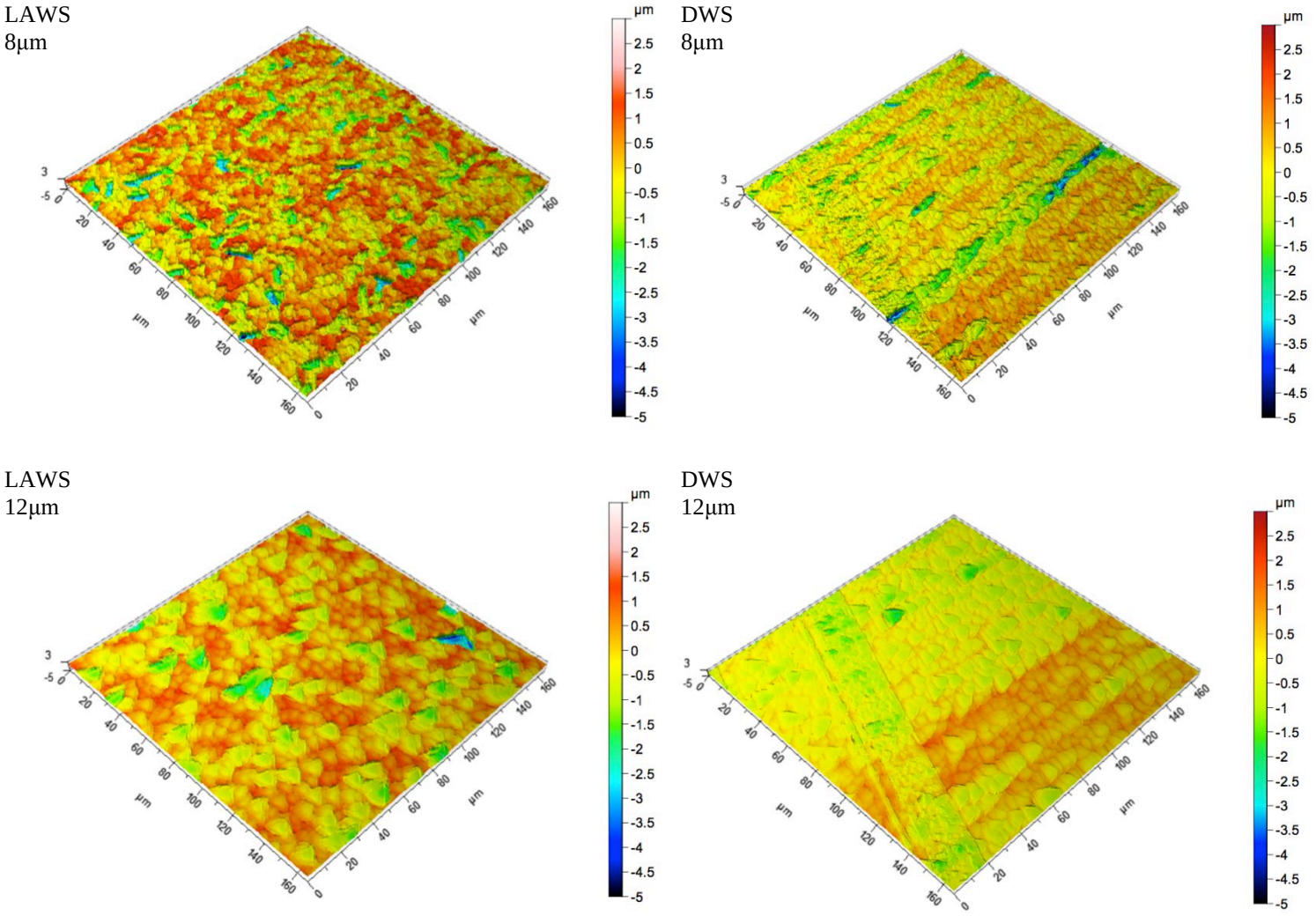

Figure 4.11: Surface morphology of LAWS and DWS wafers at 8µm and 12µm etch depths.

The acidic HNA etching of multi-crystalline Si wafers first resulted in a widening of the micro-cracks generated by saw damage. This caused an increase in the surface area as well as an increase in the surface roughness. As etching progressed, the cracks or pits from the surface were opened to form deeper and wider features that can be seen in the 8μm cases of Figure 4.9. At 12μm etch depth, the deeper features widened further and became flattened. Finally, chemical polishing took place, which is visible in the 3D surface map of the 12μm etch depth case.

Although the surface roughness decreased, Figure 4.11 shows that, in each case, the as-cut surface morphology of wire striations characteristic of DWS and the pits characteristic of LAWS were propagated by etching to the 12μm etch depth.

The effects of acidic etching on LAWS and DWS Si wafers agree very well with other published investigations [27, 77]. Because acidic etching will deepen and widen cracks, once the etch pits are removed and a more planar surface is produced, all geometrical evidence (cracks) of saw damage are removed. Even at depths where geometrical evidence of saw damage are no longer present, residual stress fields beneath the micro-cracks, produced by the sawing process, can still be present in the remaining material.

4.3.2 Experiment 2 Results

Areas Selected for Analysis

For each case of LAWS and DWS wafers, a sister wafer was etched to a depth of 16μm and the through-thickness τ_{max} was determined using the near-infrared birefringence polariscope. For each of the LAWS and DWS wafers, specific regions containing grains and grain boundaries with higher τ_{max} at the grain boundaries (in

comparison to stress inside the grains) were selected for analysis. Figure 4.12 shows the locations of the LAWS and the DWS wafers that were selected for analysis.

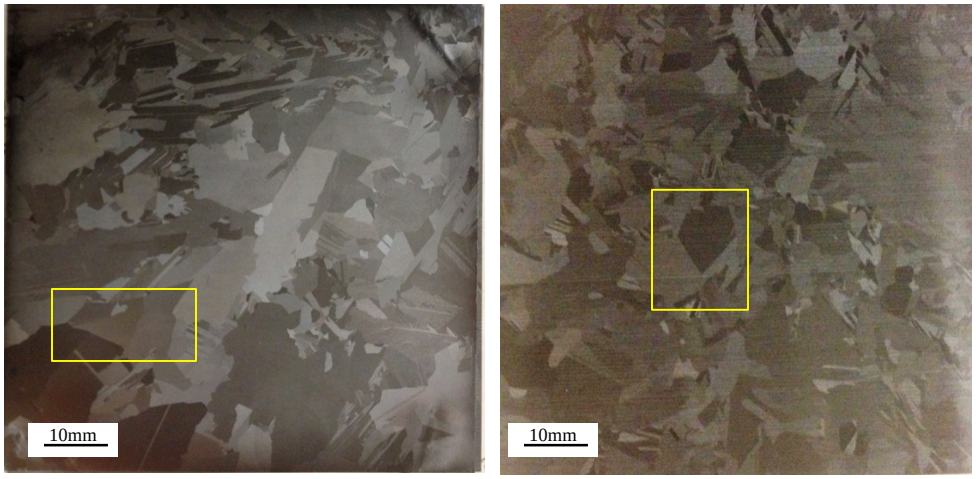

Figure 4.12: LAWS wafer (left), DWS wafer (right).

For each location shown in Figure 4.12, the near-infrared birefringence polariscope was used to obtain a full-field τ_{max} residual stress map of the entire region including the grains and the grain boundaries of interest.

Micro-Raman spectroscopy does not easily lend itself to the mapping of large areas because of its small spatial resolution and the time required for many measurements to investigate large regions. Therefore, small local areas were selected for analysis for polarized micro-Raman spectroscopy. Figure 4.13 shows the locations where the polarized micro-Raman spectroscopy measurements were made in each set of grains.

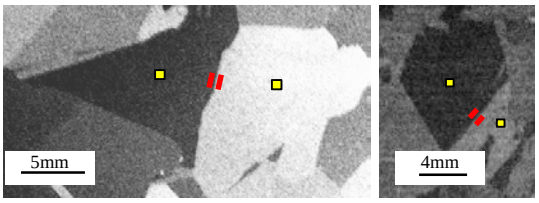

Figure 4.13: Locations for the polarized micro-Raman spectroscopy measurements. LAWS region (left) and DWS region (right). Two yellow boxes show area maps taken at the center of the grains; the two red lines show locations of the line scans taken on either side of the grain boundary.

Two locations in each grain were analyzed. One set of locations is indicated by the yellow boxes in Figure 4.13 and was in approximately the center of each grain. The second set of locations is designated by the red lines in Figure 4.13 and located on either side of the grain boundary. The measurement in the center of the grain was an area map of 60μm x 60μm. Point measurements were taken at 20μm intervals in this region to obtain a 4 x 4 point map with a total of 16 data points. The measurements near the grain boundary consisted of 50μm long line scans with a step size of 5μm yielding 10 data points for each scan. Figure 4.14 shows a representative path of the line scans on either side of the grain boundary superimposed on an optical micrograph of the region.

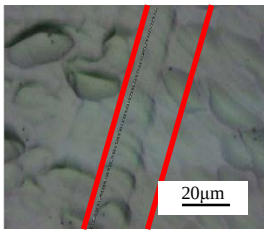

Figure 4.14: Micrograph of the grain boundary of an etched mc-Si wafer. Red lines show the path of line scans measured on either side of the grain boundary.

The measurement procedure of Becker et al. [28], which was described in Chapter 3, requires the determination of the crystal orientation of each grain relative to the laboratory coordinate system in order to calculate a stress tensor. Therefore, two line scans were made as close as possible to and on both sides of the grain boundary where the crystal orientation could be determined.

Polarized Micro-Raman Spectroscopy Results

For each of the four locations shown in Figure 4.13, the following single stress tensor was calculated from the mean peak shifts generated by the map or line scans,

$$\sigma = \begin{pmatrix} \sigma_{xx} & \tau_{xy} & 0 \\ \tau_{xy} & \sigma_{yy} & 0 \\ 0 & 0 & \Delta_z \end{pmatrix} \quad (61)$$

where σ_{xx} and σ_{yy} are stresses in the directions of the x-axis and y-axis of the laboratory coordinate system, respectively, as shown in Figure 4.15; τ_{xy} is the shear stress, and Δ_z is a factor which aided in solving the system of equations using the mathematical technique of Becker et al. [28] discussed in Chapter 3. The calculation of the stress tensor assumes plane-stress conditions in the Si wafer surface.

Two stress tensors per grain were computed from the measurements, one at the center of the grain and one at the grain boundary. Each grain was labeled using the notation shown in Figure 4.15.

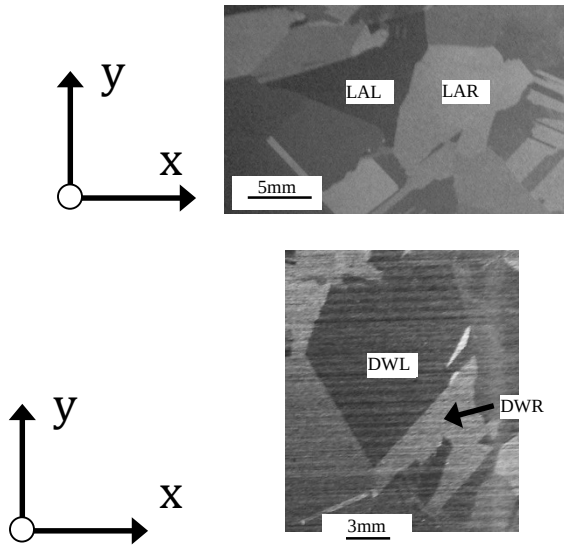

Figure 4.15: Top: LAWS region of interest showing the labels of the two grains, LAL and LAR. Bottom: DWS region of interest showing the labels of the two grains, DWL and DWR. The laboratory coordinate system is shown on the left of each image.

The two grains in the LAWS wafer were labeled ‘LAR’ and ‘LAL’ while the two DWS wafer grains were labeled ‘DWR’ and ‘DWL’. The laboratory coordinate system is shown next to the images of each wafer in Figure 4.15.

Residual Stress Produced by Wire Sawing

Figure 4.16 shows plots of the σ_{xx} component measured by polarized micro-Raman spectroscopy as a function of the etch depth for all four grains, the two LAWS grains, ‘LAL’ and ‘LAR’, and the two DWS grains, ‘DWL’ and ‘DWR’.

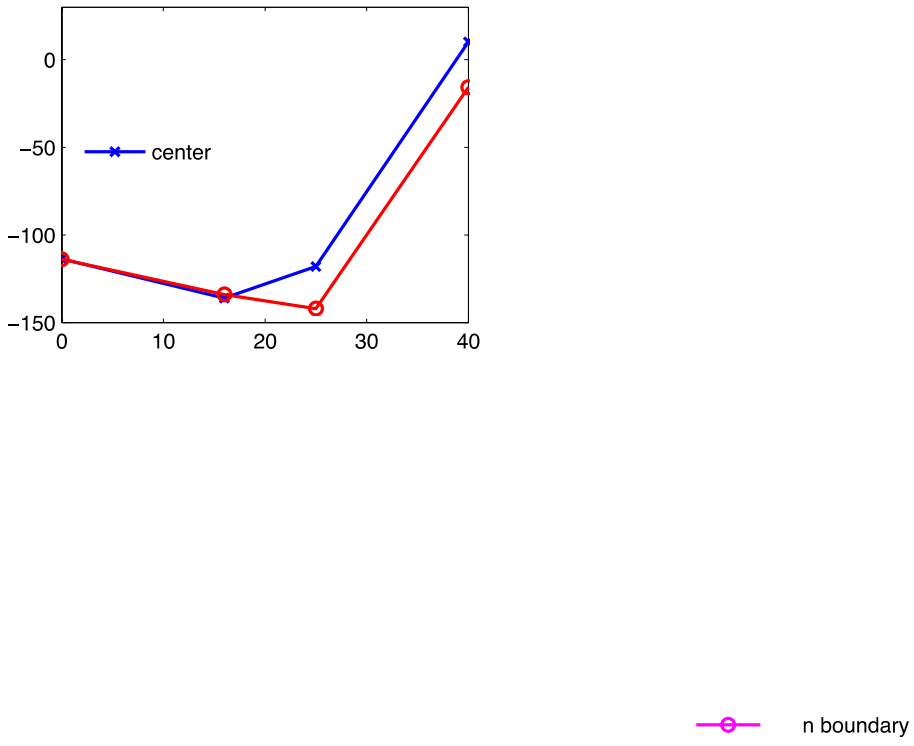

Figure 4.16: σ_{xx} as a function of the etch depth for all four grains; LAWS (top) and DWS (bottom).

The penetration depth of the 488 nm laser used in the polarized micro-Raman spectroscopy analysis was approximately 0.6μm. Therefore, the measurements taken at

the 0μm etch depth are indicative of the stress state of the as-cut saw damage layer. Saw damage is well documented as being present in the first few micrometers of an as-cut wafer of either sawing process type [34].

The findings of this thesis show that both DWS and LAWS produced compressive stresses in the surface layer of the Si wafers, irrespective of the location, i.e. within a grain or at a grain boundary. The surface residual stress produced by LAWS was found to be more compressive than the surface residual stress produced by DWS. LAWS induced surface residual stresses ranged from -50 MPa to -110 MPa depending on the location. The DWS saw damage stresses ranged from -20 MPa to -85 MPa. These ranges include stresses in both the x- and y- laboratory coordinate directions, namely, σ_{xx} and σ_{yy}. Plots of σ_{yy} as a function of etch depth are shown in Figure 4.17.

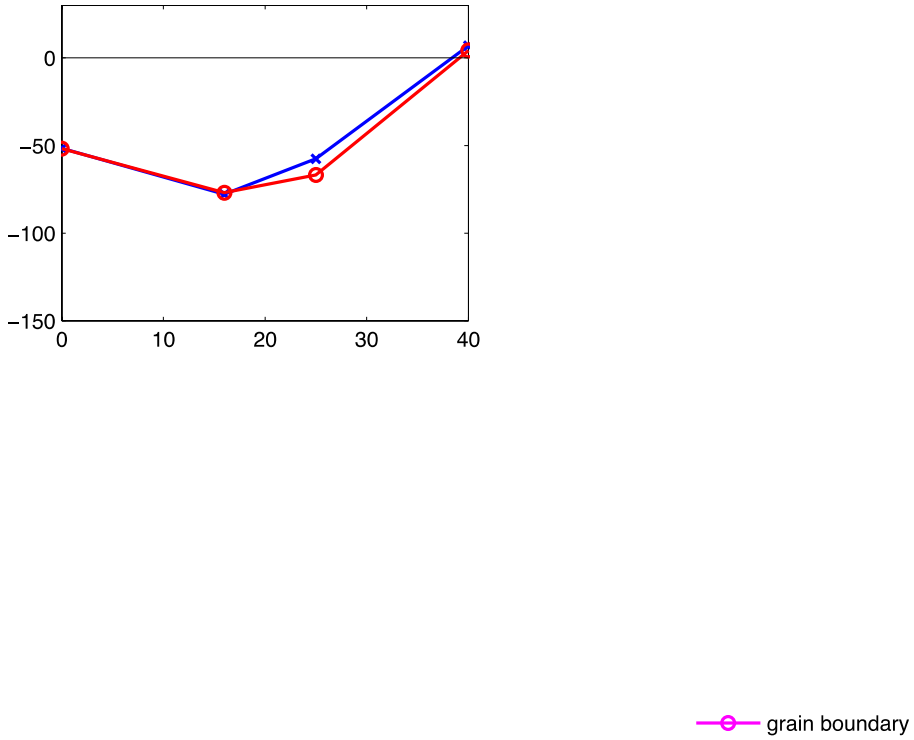

Figure 4.17: σ_{yy} as a function of the etch depth for all four grains; LAWS (top) and DWS (bottom).

Figure 4.17 shows the σ_{yy} stress component in the as-cut surfaces of wafers for both sawing process types was compressive. Similar to Figure 4.16, LAWS produced higher compressive stress compared to DWS. The reason for the differences in compressive stress magnitudes between DWS and LAWS may be explained by analyzing the basic cutting mechanisms of each process. The rolling-indenting process of LAWS may result in increased pressure in Si compared to the scratching-indenting process of DWS. In the fixed abrasive DWS process, the particles do not roll to indent the wafer; instead they slide or scratch the wafer as they are fixed to the wire. The pressure due to indentation as a result of the two cutting mechanisms would need to be estimated to determine a definitive explanation for the findings.

In both cutting mechanisms, the magnitude of the residual stress is greatly influenced by the abrasive grit size, which contacts the wafer at any given location and varies in both LAWS and DWS processes. This explains the effect of some wire striations exhibiting higher residual stress than the others, as was seen to be more apparent in the near-infrared transmission images of Figure 4.5.

Residual Stress Due to Solidification

Similar to using the 0μm etch depth as representing the stress induced solely by saw damage, the polarized micro-Raman spectroscopy stress results for the 40μm etch depth are assumed to be free from all sawing damage for both the LAWS and DWS wafers and, therefore, representative of the stress state produced by the thermal gradients present during solidification of the cast mc-Si ingot.

The measured σ_{xx} and σ_{yy} stresses for the 40μm etch depth are presented in Figure 4.16 and Figure 4.17, respectively. The residual stress produced by the thermal gradients present during casting is found to be much less compressive and often tensile compared to the stress at smaller etch depths. For the 40μm etch depth, all four locations measured in the DWS wafer were characterized by predominately low tensile stresses in the 0-30 MPa range. The center location of the DWR grain deviated from this trend, exhibiting a slightly compressive σ_{xx} stress equal to -6 MPa. The LAWS wafer showed similar trends at the 40μm etch depth with σ_{xx} and σ_{yy} ranging from -15 MPa to 10 MPa. Based on the numerical modeling work of Oswald et al. [39], the stress state within a mc-Si cast ingot was shown to be tensile, agreeing with the findings of this thesis. Oswald et al. deduced their finding based on the exterior of the ingot solidifying first during casting, creating

solid material around the center of the ingot. Because of the thermal volumetric expansion of Si occurs, tensile stresses within the ingot upon cooling/solidification of the melt in the interior of the crucible.

Trends in Residual Stress as a Function of Etch Depth

The stress states in the surfaces of both the DWS and the LAWS wafers became less compressive as the saw damage was removed in every location measured, at the center of the grains as well as at grain boundaries. At 20μm etch depth, the polarized micro-Raman spectroscopy results in all DWS locations, except at the center of grain 'DWR', showed that both σ_{xx} and σ_{yy} are tensile. The stress state in the surface of the wafer was not found to be tensile in the LAWS wafer until the wafers were etched to a depth of 40μm. This finding implies the depth of residual stress generated by LAWS extends deeper into the wafer than the depth of residual stress generated by DWS. Compressive residual stress in LAWS can extend deeper than 25μm into the wafer while the compressive residual stress in DWS is no longer present at 25μm etch depth. More data taken between 0μm and 40μm could provide greater resolution for the saw damage induced residual stress. Based on the micro-Raman spectroscopy results, which showed a distinct trend in the DWS and LAWS wafers of the residual stress state changing from compressive to tensile with increased etch depth, it can be concluded that the depth of residual stress induced by LAWS is between 25μm and 40μm and the depth of residual stress induced by DWS is between 16μm and 25μm

The residual stress trend as a function of etch depth agreed with the near-infrared birefringence polariscope results of Experiment 1, which examined the first 0-12μm of

the as-cut wafer in a different region of the same wafer. Figure 4.5, which superimposes the points of highest τ_{max} on near-infrared transmission images at multiple etch depths, showed grain boundary stresses were initially seen at 8μm etch depth in the DWS wafer and at 12μm etch depth in the LAWS wafer. The near-infrared birefringence polariscope averages stresses through the entire wafer thickness. Therefore, it is reasonable that the effect of thermal gradient induced residual stress (evident from the grain boundary stress fields) would be seen at a shallower etch depth in the polariscope measurements compared to polarized micro-Raman measurements, which only probe the wafer surface.

In addition to the comparison with other experimental findings, Wu et al. [34] determined micro-crack depth and density for wafers cut by LAWS and DWS. The mean micro-crack length in DWS wafers was found to be shorter than the micro-crack length of LAWS wafers. This further suggests saw damage depth and therefore the residual stress induced by saw damage is shallower in DWS wafers than in LAWS wafers and is supported by the findings of both Experiment 1 and Experiment 2.

Trends in τ_{xy} and τ_{max} as a Function of Etch Depth

The third component of the stress tensor, τ_{xy}, was plotted as a function of etch depth, and is shown in Figure 4.18.

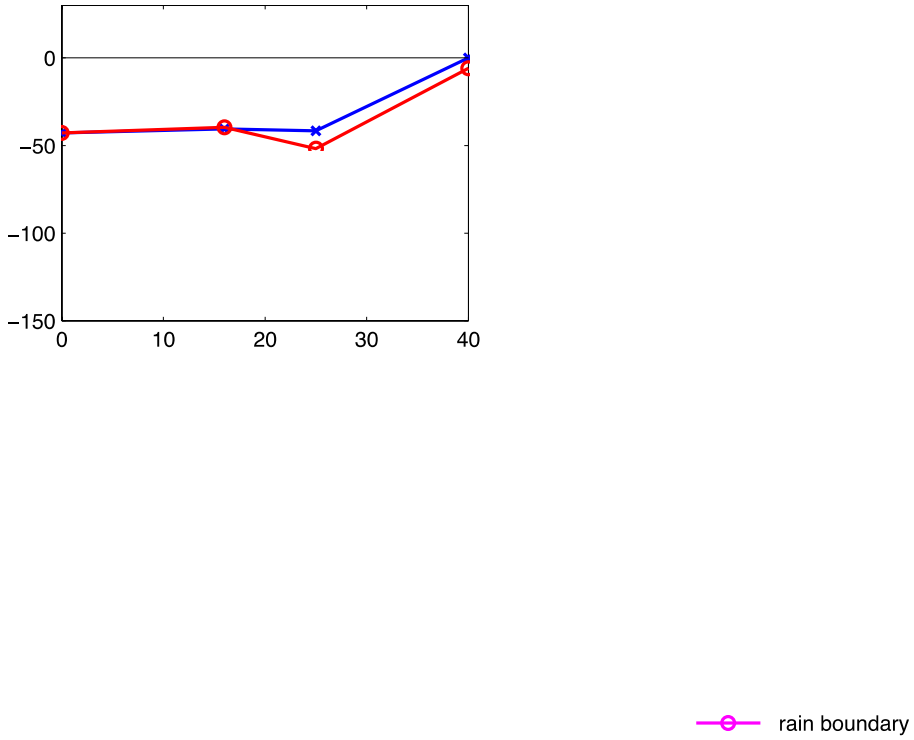

Figure 4.18: τ_{xy} plotted as a function of the etch depth for each grain and each location; LAWS (top) and DWS (bottom).

The stress component τ_{xy}, ranged from 27 MPa to -50 MPa for both LAWS and DWS, and had relatively low magnitudes compared to σ_{xx} and σ_{yy}. τ_{xy} followed a similar trend as σ_{xx} and σ_{yy} for the LAWS wafers in that it exhibited the most change between the 25μm and 40μm etch depths, which is in the range of depths where saw damage stress was removed through etching. In the DWS wafer, the magnitude of τ_{xy} varied in the saw damage layer at 0μm etch depth ranging from 0 MPa to nearly -50 MPa. At the 40μm etch depth, τ_{xy} was less than $\pm$5 MPa at all four locations measured.

The maximum residual shear stress, τ_{max}, was calculated using the equation for in-plane τ_{max} [78],

$$\tau_{max} = \sqrt{\left(\frac{\sigma_{xx} - \sigma_{yy}}{2}\right)^2 + {\tau_{xy}}^2} \qquad (62)$$

where σ_{xx}, σ_{yy}, and τ_{xy} are the components of the stress tensor measured by polarized micro-Raman spectroscopy given in Equation (61). Figure 4.19 shows τ_{max} as a function of etch depth for all four grains and locations measured.

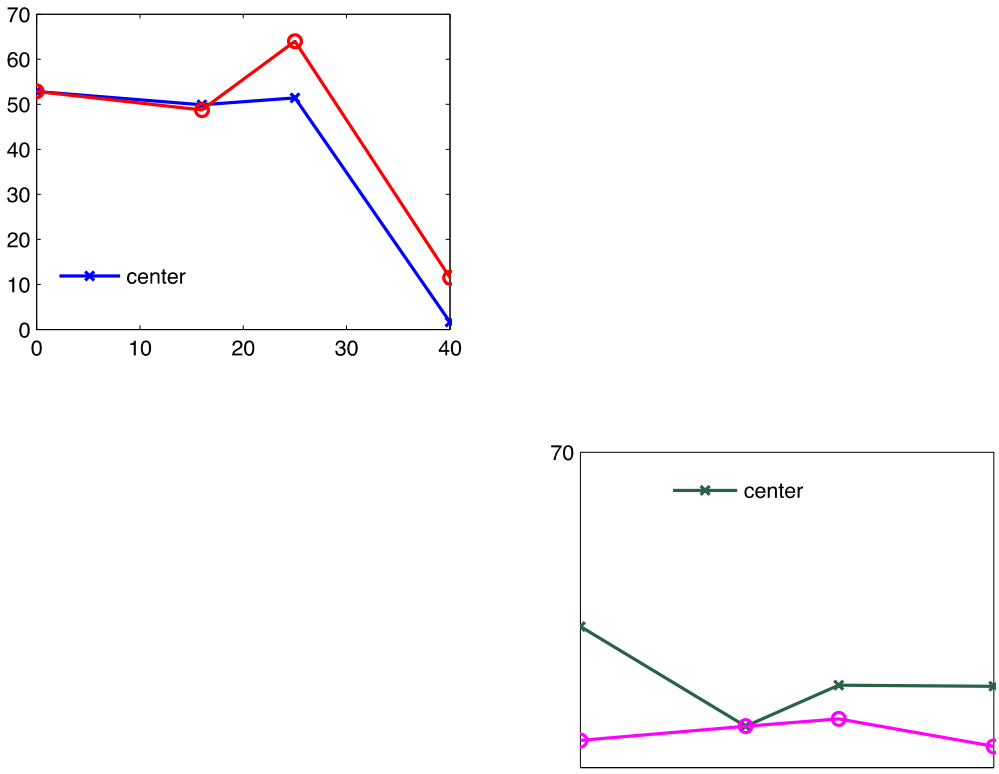

Figure 4.19: τ_{max} plotted as a function of the etch depth for each grain and each location, LAWS (top) and DWS (bottom).

The τ_{max} results did not produce any clear trends for either sawing process type or grain location. At the center of the grains and at the grain boundaries of the LAWS wafer, τ_{max} ranged from approximately 0 MPa to 50 MPa depending on the etch depth. For DWS, at the center of the grain and at the grain boundary, the τ_{max} stresses ranged from 8 MPa to 40 MPa, similar to the LAWS case. At the 40μm etch depth, which corresponds

to a depth where only solidification induced stresses are expected to be present, the τ_{max} for both the DWS and LAWS wafers was between 10 MPa and 20 MPa and spanned a smaller range of stresses than between the 0μm and 25μm etch depths.

Comparison of Residual Stress at Center of Grain and at Grain Boundary Locations.

All three components of the stress tensor, σ_{xx}, σ_{yy}, and τ_{xy}, showed there was no significant difference between the stresses corresponding to the scans taken near the grain boundary and at the center of grain. The measurements at the grain boundaries and at the center of the grains exhibited similar trends for each stress component. In other words, the trends in stress were more dependent on the *grain* measured than on the location within each grain. The only grain to exhibit a marked difference between the grain and grain boundary stresses at increased etch depths was the DWR grain. At both 25μm and 40μm etch depths, the grain boundary exhibited a tensile stress while the center of the grain had compressive stress. The σ_{xx} plot for the DWR grain is shown in Figure 4.16.

Based on these results, it is difficult to derive definitive conclusions about the difference in stress states near the grain boundaries and in the center of the grains. Previous work by Sarau et al. [25], investigated stress fields at grain boundaries. In their work, the reference for the peak shift was compared to the center of the grain instead of an etched “stress-free” CZ Si sample as in this thesis. Sarau et al. found that stress fields at grain boundaries vary and are inhomogeneous along the same grain boundary. Sarau et al. attributed this finding to the presence of dislocations, which can vary spatially both near grain boundaries and inside the grains. The results of the current thesis found residual stress to be dependent on the depth (dependent on location of saw damage or the

thermal gradient) and to be dependent on the grain examined. Large differences or trends in stress fields between the center of the grain and at the grain boundary, as a function of etch depth, were not found.

Near-infrared Polariscope Results: τ_{max}

As stated previously, the near-infrared birefringence polariscope is only able to measure τ_{max} averaged through the wafer thickness at each point imaged in the wafer and is not able to distinguish the stress type (i.e. tensile or compressive) without additional analysis, which is usually very sensitive to noise in the isoclinic parameter [8]. For each of the four grains examined using micro-Raman spectroscopy, the polariscope was used to spatially map τ_{max}. For the purposes of comparing the τ_{max} values obtained from the two residual stress measurement techniques, all points inside the grain, i.e. excluding the grain boundary, were selected and the τ_{max} values averaged to produce a mean value. An example of the selection process is shown in Figure 4.20.

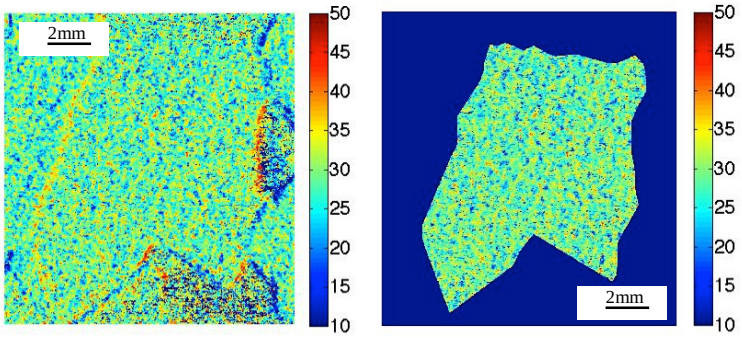

Figure 4.20: Example of grain selection. Left (LAWS) 'LAR' Grain, τ_{max} map, Right: Selection of stress only within the 'LAR' grain is used for mean τ_{max} calculations.

Figure 4.21 shows the calculated mean τ_{max} as a function of the etch depth for each of the two DWS and two LAWS grains investigated. The grains were labeled using the

same notation used for the polarized micro-Raman spectroscopy results, as shown in Figure 4.15.

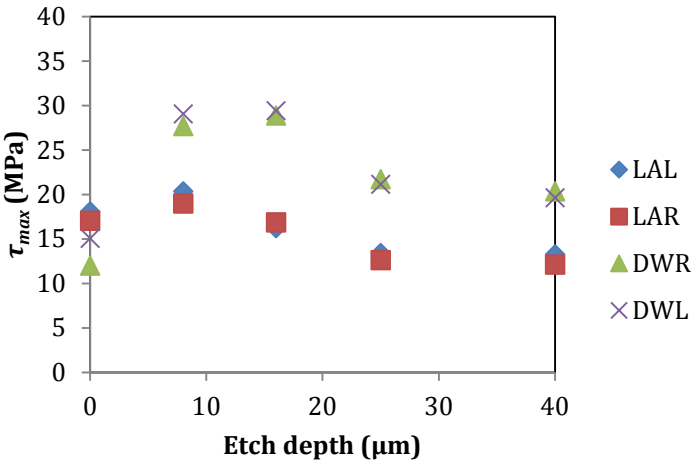

Figure 4.21: Mean τ_{max} plotted as a function of etch depth for each DWS and LAWS grain analyzed.

The mean τ_{max} of both DWS grains, 'DWR' and 'DWL', increased from 12 MPa and 15 MPa, respectively, at 0µm etch depth to approximately 30 MPa for both grains at 8µm etch depth. At 25µm and 40µm etch depths, the mean τ_{max} values were approximately 20 MPa. LAWS followed a similar trend with smaller differences in the mean τ_{max} between the data points. For each sawing process type, the mean τ_{max} in both grains analyzed followed the same trends. At 25µm and at 40µm, the mean τ_{max} values reached a plateau at 12 MPa.

The results from the near-infrared birefringence polariscope were used to create histogram plots showing the distribution of τ_{max} in both the DWS and LAWS wafers in larger regions which exhibited many grains. These histogram plots are representative of the full LAWS and DWS wafers. Figure 4.22 displays the histograms showing the τ_{max} distribution for increasing etch depths for both the DWS and LAWS wafers.

Etch depth: (μm)	0	8	25	40
DWS	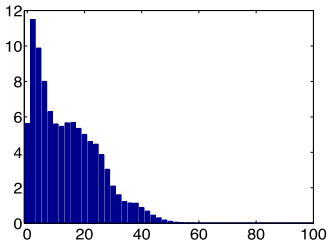	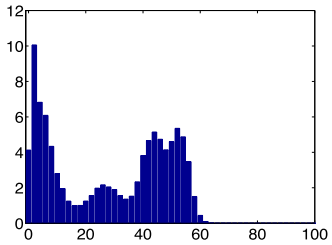	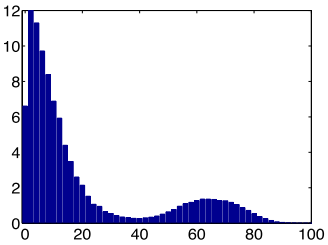	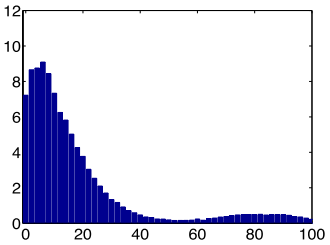
LAWS	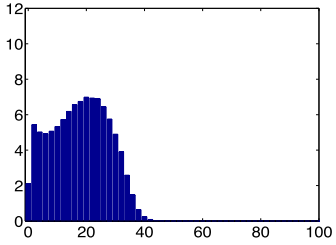	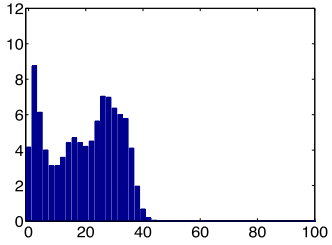	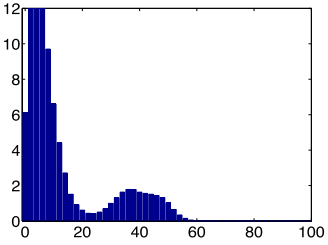	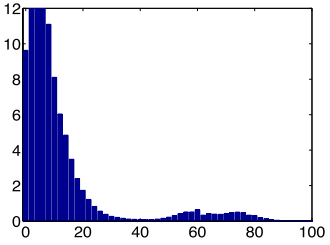

Figure 4.22: Histograms showing τ_{max} distributions for DWS (top) and LAWS (bottom) at 0μm, 8μm, 25μm, and 40μm etch depths.

The frequency or "count" was normalized in each plot to account for the variation that occurs due to manual error during the selection of the same spatial regions. The y-axis of Figure 4.22 therefore shows the "percent area of the region selected" for each bin of the histogram.

The histograms in Figure 4.22 show that the range of τ_{max} increased as the etch depth increased for both the LAWS and the DWS wafers. At 0μm, the τ_{max} spanned from 0 MPa to 40 MPa for both the LAWS and DWS wafers. The range increased from 0 MPa to 100 MPa in the DWS wafer and from 0 MPa to 80 MPa in the LAWS wafer at 40μm etch depth. However, the histograms of τ_{max} at the ~20μm and 40μm etch depths show that the majority of τ_{max} values were between 0 MPa and 20 MPa. The 'tails' of the distributions became much longer yielding a larger span of τ_{max}. The histograms for LAWS and DWS were very similar in shape at 20μm and at 40μm etch depths, implying that the influence of the two types of saw damage were mostly removed at this depth and that the distributions are representative of stresses caused by the thermal gradients during mc-Si ingot casting. This data implies that the through-thickness τ_{max} due to the thermal gradient during mc-Si ingot formation can span a range greater than 0-100 MPa, depending on the ingot and location. Prior to etching, the through-thickness τ_{max} had a much narrower range and spanned approximately 0 MPa to 40 MPa. The compressive layers induced on the surface by saw damage change the through-thickness τ_{max}, resulting in a smaller range compared to wafers with no saw damage.

At increased etch depths, the points of highest stress were not concentrated along the wire striation lines or randomly distributed in either wafer. Instead, at the 40μm etch depth, high τ_{max} was located along grain boundaries in both the LAWS and DWS wafers.

In addition to the high τ_{max} points along grain boundaries at this etch depth, many high τ_{max} stress points were also present within the grains. Relative to stresses within grains, the grain boundaries of either sawing process type showed mean τ_{max} in the range of 25 MPa to 50 MPa at 40μm etch depth. In comparison, the within -grain mean τ_{max} stresses were approximately 10-20 MPa. These magnitudes were found by isolating and averaging the τ_{max} stress in the center of grains and at the grain boundaries for the 40 μm etch depth case. This was done for each of the four grains studied using the process shown in Figure 4.20.

4.4 Comparison of Results of Near-Infrared Birefringence Polariscopy and Polarized Micro-Raman Spectroscopy

The 16μm etch depth LAWS data is used to present a comparison of the measurements taken by micro-Raman spectroscopy and near-infrared birefringence polariscopy. Figure 4.23 shows the near-infrared birefringence polariscope results at 16μm etch depth for the LAWS ‘LAR’ grain.

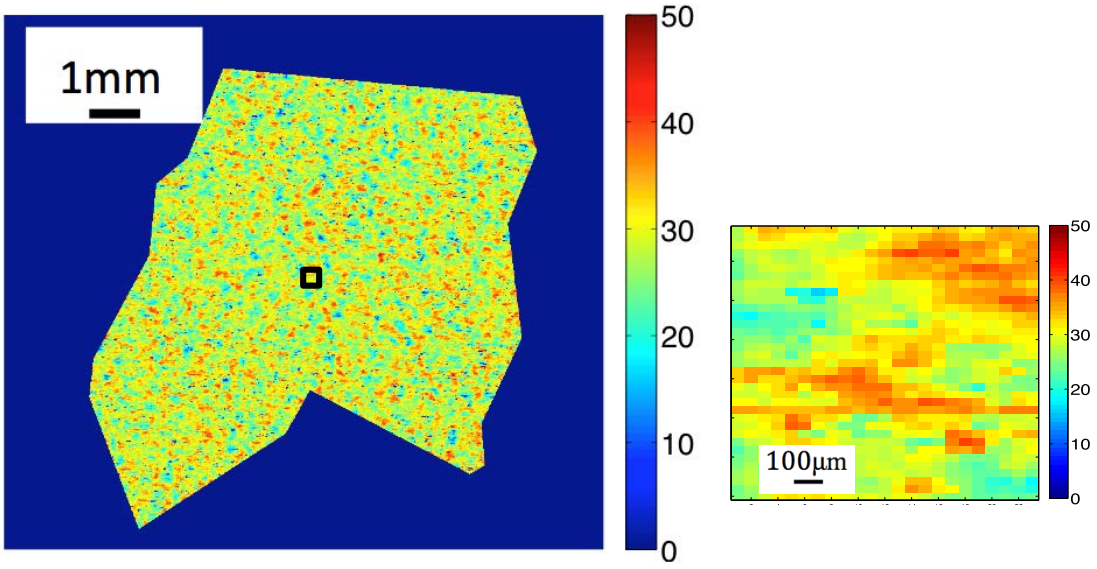

Figure 4.23: Left: τ_{max} map for LAR grain. Right: τ_{max} map for 0.75 mm x 0.75 mm region selected in the center of the grain represented by the black box shown on left.

The map on the left of Figure 4.23 shows all τ_{max} values within the 'LAR' grain, excluding the grain boundary. The plot on the right shows an approximately 0.75 mm x 0.75 mm region in the center of the grain; its location is shown by the black box on the left-hand plot. This example shows the large range of τ_{max} stresses that the near-infrared birefringence polariscope measures over both large and small areas. At the center of the grain and all over the grain, τ_{max} ranged from 10 to 40 MPa.

In addition, the grain boundary, while it exhibited a slightly narrower range of stresses, was still found to have a large range of τ_{max} values. In the same manner as before, all τ_{max} points along the grain boundary between the grains 'LAR' and 'LAL' were selected, excluding the points in the interior of the grains. Figure 4.24 shows the τ_{max} grain boundary residual stress map and its distribution.

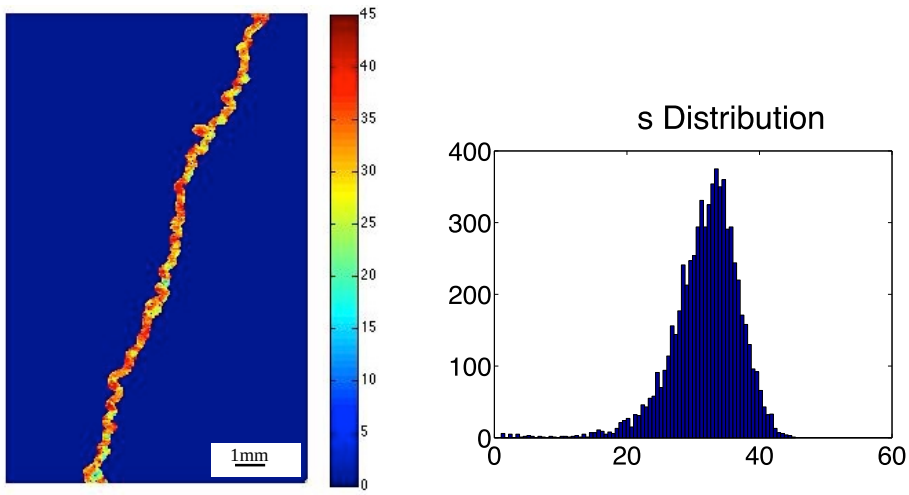

Figure 4.24: 'LAR' and 'LAL' grain boundary τ_{max} stress. Left: τ_{max} map of grain boundary stresses. Right: distribution of stress within the grain boundary.

The grain boundary stress distribution showed the τ_{max} mathematical mode was at approximately 34 MPa. However, even at the grain boundary, a distribution that resembles a Normal or skewed right distribution is obtained, with the majority of τ_{max} spanning from 25 MPa to 40 MPa. Table 4.2 shows the statistics for the extracted regions for the 'LAR' within-the grain stress and for the grain boundary stress. The τ_{max} obtained from the near-infrared birefringence polariscope ranged from 44 MPa at the grain boundary to 25 MPa at the center of the grain.

Table 4.2: Statistical summary of τ_{max} measured by the near-infrared birefringence polariscope; LAWS wafer, 16μm etch depth.

	'LAR' Grain	Center of 'LAR' Grain 0.75 mm x 0.75 mm region	Grain boundary between 'LAR' and 'LAL'
Mean	28 MPa	30 MPa	32 MPa
Maximum	49 MPa	40 MPa	45 MPa
Minimum	0 MPa	15 MPa	1 MPa
Range	49 MPa	25 MPa	44 MPa

The stress tensors and the τ_{max} stress found in the center of the 'LAR' grain and on both sides of the grain boundary at 16μm etch depth using polarized micro-Raman spectroscopy are given in Table 4.3.

Table 4.3: Polarized micro-Raman spectroscopy stress results for LAWS wafer at 16μm etch depth.

	'LAR' Center of grain	'LAR' Grain boundary	'LAL' Grain boundary
Stress tensor	$\begin{pmatrix} -81 & -22 & 0 \\ -22 & -87 & 0 \\ 0 & 0 & 0 \end{pmatrix}$ MPa	$\begin{pmatrix} -94 & -11 & 0 \\ -11 & -97 & 0 \\ 0 & 0 & 0 \end{pmatrix}$ MPa	$\begin{pmatrix} -134 & -40 & 0 \\ -40 & -77 & 0 \\ 0 & 0 & 0 \end{pmatrix}$ MPa
τ_{max} (MPa)	22	12	49

The τ_{max} value at the center of the grain marked 'LAR' was 22 MPa. The τ_{max} at the grain boundary measured from the 'LAR' side was 12 MPa and 49 MPa when measured from the 'LAL' side. The measurements made by near-infrared birefringence polariscopy and polarized micro-Raman spectroscopy had the same order of magnitude. Based on the differences in spatial resolution and the differences in the sample volume probed, the two measurements are not expected to give the same values. Similar order of magnitude is satisfactory to verify that the results were consistent.

In Chapter 3, the two methods were compared in terms of their fundamental physical principles. It was described that both near-infrared birefringence polariscopy and polarized micro-Raman spectroscopy use the same fundamental principles of the effect of a medium on an electromagnetic wave to measure residual stress. As discussed, the near-infrared birefringence polariscope uses the index of refraction, *n,* for its calculations whereas micro-Raman spectroscopy uses phonon deformation potentials derived from the susceptibility, χ, of Si. The parameters used are primarily a product of tradition and

training. Engineering applications tend to use the index of refraction, n, while physicists prefer the use of the dielectric constant, ε, or the susceptibility, χ [74].

The near-infrared birefringence polariscope averages the stress through the wafer thickness in a full-field stress map and shows a large range both within the grains and at the grain boundaries. Meanwhile, the polarized micro-Raman spectroscope probes very small areas ($<100\mu m^2$) and has less variability within these local areas, but is not representative of the larger field assessed by the near-infrared birefringence polariscope. The stress tensor derived from micro-Raman spectroscopy can be used to calculate a value of τ_{max}, however due to the differences in the sample volume probed, they cannot be directly compared. The two techniques however can be used in parallel and demonstrate congruence in the study of both surface and through-thickness residual stresses.

4.5 Error Analysis – Polarized micro-Raman Spectroscopy and Near-infrared Birefringence Polariscopy

This section discusses the accuracy of both measurement techniques used. The near-infrared birefringence polariscope was previously developed [59] and was found to be accurate to within 1 MPa of known applied stress during an experiment designed to validate the measurement technique [8].

The Renishaw InVia micro-Raman spectrometer has a spectral resolution of 0.02 cm^{-1}. This peak shift correlates to a difference in stress values of 6 MPa. Using the CZ mono-Si etched “stress free”, sets of 16 and 8 Raman spectra were taken to examine the repeatability of the Renishaw InVia system. For each set of spectra, the standard deviation was calculated to be less than 0.02 cm^{-1} for both sample sizes. Based on the repeatability and accuracy of the measurements, the polarized micro-Raman spectroscopy

technique can be said to be accurate to within +/- 18 MPa, using the three-sigma rule of standard deviation for the sample sizes used.

4.6 Discussion

It is known that compressive stress, when present on the surface of a metal material, can inhibit fracture and enhance fatigue strength. In brittle materials, such as Si, the effect of stress type on fracture and fatigue is not as well understood. For the surfaces of as-cut LAWS and DWS sawn wafers, while the stress state was found to be compressive, they are also damaged by micro-cracks, pits, spalling, and grooves, which are defects that can lead to fracture and negate the effect of a potentially beneficial compressive surface layer.

Yang et al. [21] found that the fracture strength of DWS wafers is highly dependent on the direction of stress applied relative to the wire striations (or saw marks). The fracture probability is shown in Figure 4.25.

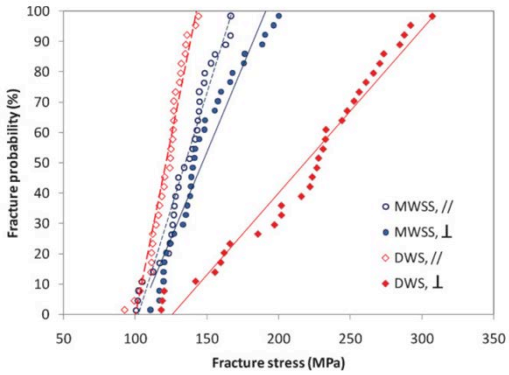

Figure 4.25: Weibull plot of fracture strength distributions for LAWS (MWSS) and DWS wafers measured in two bending orientations: parallel (//) and perpendicular (⊥) to the wire speed direction [21].

When tensile stress is applied perpendicular to the wire striations, the wafers were shown to exhibit lower fracture strength than when the stress is applied parallel to the wire striations. The characteristic strength of LAWS wafers was found by Yang et al. to be between the two characteristic strength values of DWS for perpendicular and parallel applied stress.

The higher τ_{max} seen in the as-cut DWS wafers along the wire striations in this study suggests that it is a possible contributing factor to the lower fracture strength observed in the study of Yang et al. for the perpendicularly applied stress case. The large number of high τ_{max} stresses in the saw damage layer of DWS wafers could lead to increased fracture during manufacturing and outweigh the benefit of decreased kerf loss when compared to LAWS. A cost-benefit analysis of industrial processes would be required to confirm this possibility. In addition, the lower compressive stress measured by micro-Raman spectroscopy in the saw damage layers shown in Figure 4.16 and Figure 4.17 and the higher micro-crack density of DWS wafers [34] compared to LAWS wafers mean that they are likely to fracture more during subsequent handling and processing steps.

The stress type induced by the thermal gradients during solidification of mc-Si ingots was found to be primarily tensile in nature. The finding of tensile stress within the center of the grain agrees with the numerical simulations of the casting process [39]. The relative magnitudes of tensile stress are likely dependent on the solidification rate, which was not studied as a variable in the work reported in this thesis. All the grains studied possessed similar tensile stress magnitudes between 0 MPa and 30 MPa, shown in Figure 4.16 and Figure 4.17.

4.7 Conclusions

The objective of the experiments described in this chapter was to investigate the contribution of residual stress generated from saw damage caused by wire sawing and the contribution of residual stress generated by the thermal gradient produced during casting and solidification of mc-Si ingots. The polarized micro-Raman spectroscopy technique was used to determine the residual stress states (compressive or tensile) and magnitudes in specific locations on the surface of mc-Si wafers while the near infrared birefringence polariscopy technique was used to determine the full-field *through-thickness* residual maximum shear stress in the mc-Si wafers. The major findings of this chapter are summarized below.

:

Residual Stress due to Wire Sawing:

- Diamond Wire Sawing (DWS) produces high through-thickness residual maximum shear stresses, τ_{max}, (>25 MPa) that are spatially aligned with wire striations. Loose Abrasive Wire Sawing (LAWS) produces high τ_{max} stresses (>25 MPa) that are randomly distributed, with no directional preference.
- Both DWS and LAWS produce compressive residual stresses (σ_{xx} and σ_{yy}) in the as-cut mc-Si wafer surface. LAWS produces larger compressive stresses in the as-cut surface layers than DWS. The surface residual stresses (σ_{xx} and σ_{yy}) in the LAWS and DWS wafers examined ranged from -50 MPa to -110 MPa and from -18 MPa to -80 MPa, respectively.
- With increasing etch depth, the residual stresses (σ_{xx} and σ_{yy}) in the DWS and LAWS wafers transition from compressive to tensile. Based on the etching

results, the depth of residual stress due to LAWS is estimated to be between 25 to 40 μm while that due to DWS is estimated to be between 16 and 25 μm.

- The mean through-thickness τ_{max} produced by DWS does not change with the grain orientation. In contrast, the mean through-thickness τ_{max} produced by LAWS does change with grain orientation.
- DWS produces high and low distinctive mean through-thickness τ_{max} stresses along the grain boundaries compared to within the grains. In contrast, LAWS does not produce distinctive τ_{max} stress fields along the grain boundaries.
- There are no significant differences in the surface residual stress states or the surface residual stress magnitudes (σ_{xx} and σ_{yy}) between the inside of a mc-Si grain and the grain boundary.

Residual Stress due to Solidification:

- After saw damage removal (40 μm etch depth), the surface residual stresses (σ_{xx} and σ_{yy}) due to thermal gradients present during solidification/casting are found to be much less compressive (and mostly tensile) than the surface stresses in the as-cut surfaces of the wafers. After saw damage removal, the DWS wafer yielded tensile residual stresses (σ_{xx} and σ_{yy}) in the 0-30 MPa range while the LAWS wafer yielded stresses in the -15 MPa to 10 MPa range.
- NIR birefringence polariscopy measurements show that after saw damage removal (40 μm etch depth) the mean through-thickness residual maximum shear stress, τ_{max}, is greater at the grain boundaries (25-50 MPa) than inside the grains (10-20 MPa).

- With progressive etching, the through-thickness residual maximum shear stress, τ_{max}, are concentrated in the grain boundary regions of DWS and LAWS wafers. This suggests that casting and solidification induced residual stresses tend to accumulate at the grain boundaries in mc-Si wafers.

Polarized Micro-Raman Spectroscopy versus NIR Birefringence Polariscopy:

- While the two residual stress measurement techniques cannot be compared directly (due to one being a surface probing technique and the other being a through-thickness technique), the results of this study confirm that, on an order of magnitude basis, the two methods yield similar values of the maximum shear stress, τ_{max}, when probing the same region of a wafer.
- The polarized micro-Raman technique is well-suited to measure the individual components of the residual stress, including their states and magnitudes, generated by wire sawing in the surface layers of crystalline Si wafers. The NIR birefringence polariscopy method is well-suited to measure the full-field distribution of the maximum residual shear stress due to casting and solidification.

CHAPTER 5
THE EFFECT OF RESIDUAL STRESS ON ELECTRICAL PERFORMANCE IN mc-SI WAFERS

This chapter describes the results obtained from experiments designed to meet the second objective of this thesis, which is to understand the effect of residual stress on the electrical performance of Si wafers used for PV applications. The experiment in this chapter again relies on the use of both near-infrared birefringence polariscopy and polarized micro-Raman spectroscopy to measure the residual stress. In addition, photoluminescence (PL) is introduced as a means to evaluate electrical performance in minimally processed mc-Si wafers. In this chapter, first, a background is provided to summarize previous work and to create a basis for the experimental method used. Subsequently, the experimental procedure is described, the results are discussed, and finally, the conclusions are presented.

5.1 Background

As summarized in the literature review of Chapter 2, stress as a parameter for electrical activity has been previously studied in relationship to the band gap energy for semiconductor materials [23, 42-44]. While it is well understood that applied stress directly changes the band gap energy of Si and this change is highly reversible if the applied stress is removed, the quantitative effect of residual stress induced during industrial manufacturing has not been sufficiently studied.

Gundel et al. [23] simultaneously studied stress and defect luminescence using micro-photoluminescence (μPL) spectroscopy. Using μPL to map areas surrounding the presence of metal precipitates in Si wafers, both tensile and compressive stress fields were found, and residual stress and the μPL response were simultaneously measured at the same locations. A positive correlation was found between tensile stress and increased recombination activity surrounding metal precipitates, regardless of the type of metal precipitate. Correspondingly, compressive stress was found to decrease the recombination activity surrounding the precipitates. It was hypothesized by Gundel et al. that in the regions containing metal precipitates, the increased mobility caused by tensile stress surrounding recombination centers facilitated the movement of carriers to the recombination center, and is therefore assumed to be detrimental to the electrical performance of a finished cell in these regions. Likewise, compressive stress hindered the recombination in the areas surrounding the precipitates. The experiment of this chapter attempts to build upon previous knowledge to increase the understanding of residual stress on electrical performance in mc-Si wafers.

The experiment reported in this chapter uses polarized micro-Raman spectroscopy to examine the state of surface stress in mc-Si wafers at locations within grains and at grain boundaries, and uses a near-infrared birefringence polariscope to study the residual maximum shear stress, τ_{max}, averaged over the wafer thickness, at a lower spatial resolution. The residual stress findings are correlated to electrical activity using PL. By studying the residual stress state through the wafer bulk as well as on the surface at a higher spatial resolution, more applicable findings were derived with respect to the direct effect of manufacturing induced residual stress on the electrical performance.

5.2 Experimental Procedure

5.2.1 Overview

The experimental procedure was designed to isolate the effects of manufacturing induced residual stress on the electrical performance of mc-Si wafers. Saw damage and residual stress caused by the wire sawing (or wafering) process results in a high number of dangling bonds due to disruption of the crystal lattice. In the case of DWS, a thin amorphous layer can also be produced on the wafer surface due to ductile mode cutting [79]. The saw damage layer is always removed during the fabrication of solar cells because of its adverse effect on electrical performance. The experiment detailed in this chapter selectively studies residual stress produced by the thermal gradients during the solidification of the Si ingot as it is the only source of stress that is expected to impact the electrical performance of a finished cell.

The experimental process flow is shown in Figure 5.1.

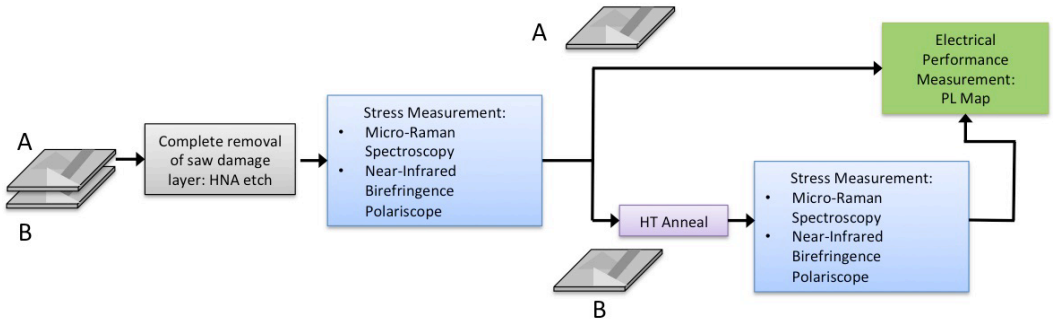

Figure 5.1: Process flow diagram for electrical performance experiment.

Two mc-Si sister wafers were first cleaned and chemically etched using a wet isotropic etch (HNA) to remove 40μm from each side of the wafers to include all saw damage. After this step, the full-field through-thickness residual maximum shear stress,

τ_{max}, was measured using the near-infrared birefringence polariscope, and the localized surface stress tensors were determined using polarized micro-Raman spectroscopy. One wafer was kept as a control sample and its electrical activity was measured by PL mapping, while the other wafer was high temperature annealed (HT anneal) in order to change its stress state. The intent of the HT anneal was to reduce or alter the residual stress state of the wafer by heating it to a temperature high enough to cause movement of crystallographic planes while not changing the crystal orientation and structure of the sample. After annealing, residual stress was again measured using the two methods, and the electrical activity was measured using PL. The process flow results in two residual stress cases: a "high stress case" labeled wafer A, and a "lower or altered stress case" labeled wafer B.

Photoluminescence (PL) of Si wafers is caused by the radiative recombination of photo-excited electron hole pairs. Radiative recombination, also known as band-to-band recombination, results when an electron in the conduction band directly combines with a hole in the valence band and a photon is released [80]. To conduct the PL mapping experiment, a diode laser is used to illuminate the Si wafer and a Si-CCD camera is used to detect the radiative recombination. The typical set-up and method for PL is described by Trupke et al. [81]. Photoluminescence is able to provide measurements indicative of the finished cell electrical performance of Si wafers [82].

5.2.2 Wafer Samples

The samples used for the experiment were two 156 mm x 156 mm mc-Si sister wafers, which were taken from the center of a mc-Si ingot to limit the number of

impurities or inclusions. No dicing of the wafers was performed in order to prevent any stress relaxation within the grains that would affect the measurements.

Prior to high temperature annealing, and after saw damage removal, τ_{max} was measured in both samples using the near-infrared birefringence polariscope in order to confirm the sister wafer assumption. The wafers were found to exhibit very similar τ_{max} residual stress maps, as shown in Figure 5.2a and Figure 5.2b.

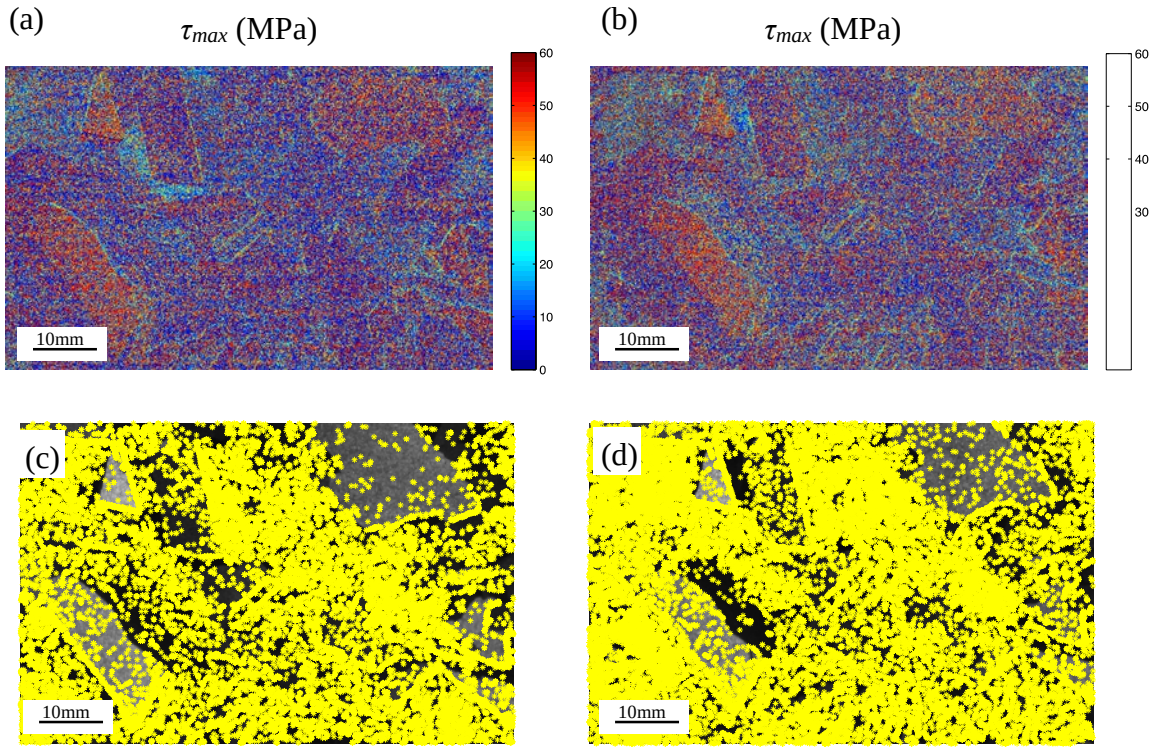

Figure 5.2: τ_{max} maps prior to annealing and spatial distribution of points of highest $\tau_{max.}$; (a) residual stress map for Wafer A, (b) residual stress map for Wafer B; (c) and (d) show NIR transmission images of the same regions in the sister wafer with yellow data points showing locations of τ_{max} > 60 MPa in Wafer A and Wafer B, respectively.

It can be seen from Figure 5.2 that the residual stress maps are very similar for the two sister wafers. While there are slight differences between the two plots in (c) and (d),

the number of points greater than the 60 MPa threshold was found shown to be similar in both wafer samples.

5.2.3 Cleaning and Etching Procedure

The wafer cleaning and etching procedure step was performed with care to reduce the number contaminants on the wafer surfaces and to fully remove the saw damage layer. The wafers were placed in a cartridge and held vertically during each bath and rinse step. All processing steps took place in a class 100 cleanroom to reduce the number of contaminants. Contaminant particles are known to negatively influence the HT annealing process by migration into the substrate at elevated temperatures [83]

The saw damage in both wafers was completely removed by wet chemical isotropic etching. The wafers were etched for 8 minutes in HNA ($HF:HNO_3:CH_3COOH$) with a ratio of (8:75:17) to yield a planar polishing etch rate of 5μm per minute [75]. Approximately 40μm of material was etched from each side of the wafer for a total of 80μm material removal. The full cleaning and etching procedure is detailed in Table 5.1.

Table 5.1: Cleaning and etching procedure used for as-cut Si wafers to remove saw damage.

Step	Description
1.	Deionized water (DI H_2O) rinse
2.	10% Hydrofluoric acid (HF) dip
3.	DI H_2O rinse
4.	High concentration KOH etch (5 minutes): The purpose of this step is to strip the badly damaged surface areas, remove organics, and prevent staining due to porous Si formation during subsequent etching steps.
5.	DI H_2O rinse
6.	10% HF dip
7.	DI H_2O rinse
8.	Dry using Nitrogen (N_2) gas
9. 10. 11. 12. 13. 14. 15.	CMOS Clean: Piranha bath (HSO_4:H_2O_2) (9:1) 120°C, 10 minutes DI H_2O rinse SC-1 bath (H_2O:NH_4OH:H_2O_2) (5:1:1) 80°C, 10 minutes DI H_2O rinse 10% HF dip DI H_2O rinse
16.	DI H_2O rinse
17. 18.	HNA (HF:HNO3:CH3COOH) (8:75:17) etch 8 minute etch resulting in 40μm etch per side (5μm/minute rate) Note: the wafers were removed from the bath and rinsed several times during this step in order to reduce the heat generated by the etching process.
19.	DI H2O rinse
20.	Commercial Piranha bath
21.	DI H2O rinse
22.	SC-2 bath (5:1:1) (H2O:HCl:H2O2), 10 minutes
23.	DI H2O rinse
24.	Dry using Nitrogen (N2) gas

Table 5.1 shows that a thorough cleaning procedure was performed both prior to and after the saw damage HNA etch in step 11. A high concentration potassium hydroxide (KOH) etch was also performed prior to the saw damage (HNA) etch in order to strip badly damaged surface areas and remove organics. This step prevents staining of the wafer due to porous Si formation during subsequent steps.

5.2.4 High Temperature Anneal

HT annealing was performed in a Tystar Poly Furnace with N_2 gas flow with the goal of reducing or altering the residual stress through the potential pairwise annihilation of dislocations, or diffusion of dislocations out to the wafer surfaces [84]. The HT anneal was performed at 1100 °C for 8 hours. The temperature ramp-up rate was set to 10 °C per minute and the ramp-down rate was set to 2 °C per minute. During the ramp-down period, the temperature was held at 600 °C for 3 hours to allow for migration of precipitates back into the dislocation regions and to reduce temperature gradient ramp-down induced stress.

The HT anneal temperature of 1100 °C was based on the findings of Hartman et al. [84]. The brittle-to-ductile transition temperature for Si is between 530 °C to 660 °C depending on the strain rate and dopant concentration [85]. Above this temperature, dislocations are able to move along certain crystallographic slip planes. Additionally, there is a characteristic temperature, T_0, approximately at 1000 °C, above which, dislocations can move unconstrained by glide planes [84]. Hartman et al. found large grain-to-grain variations in the dislocation density after HT annealing at temperatures between 1100 °C to 1170 °C. Higher temperatures closer to 1366 °C produced predictable dislocation pair annihilation, however 1100 °C was sufficient to produce

movement of dislocations and is therefore considered to be high enough to alter the residual stress state within the wafers.

5.2.5 Photoluminescence and Electrical Performance Correlation

PL mapping was performed using a BT Imaging LIS R2 PL imaging tool at Suniva, Inc. located in Norcross, Georgia. The spatial resolution of the tool is 160μm/pixel, which has a similar order of magnitude, albeit larger, than the spatial resolution of ~ 17μm/pixel obtained with the near-infrared birefringence polariscope.

The results generated by PL mapping of as-cut Si wafers are indicative of the finished cell electrical performance [82]. Although the wafers used in this study were not truly as-cut since they were etched prior to PL mapping, the surface was still characterized by a very high surface recombination velocity (SRV) due to the presence of dangling bonds. Haunschild et al. [82] examined the use of PL mapping in multiple process steps for as-cut Si wafers to determine finished cell performance. Surface passivation is needed to accurately calibrate and determine the bulk minority carrier lifetime using PL for wafers with high SRV due to the fact that poor surface quality will dominate the bulk lifetime results. While PL mapping does not produce a quantitative measure of minority carrier lifetime in as-cut wafers, it can be used to qualitatively determine areas of crystal lattice defects that directly affect finished solar cell performance [82].

5.3 Results and Discussion

All steps of the experiment were completed as detailed in section 5.2. The two wafer residual stress cases, i.e. pre-anneal and lower or altered residual stress post-anneal,

were compared using the near-infrared birefringence polariscope to map residual stress, and PL to determine electrical performance.

Figure 5.3 shows the PL maps and the near-infrared transmission images with locations of high τ_{max}, namely greater than 60 MPa, plotted for the same regions in the center of each wafer, approximately 52 mm x 35 mm, shown in Figure 5.2.

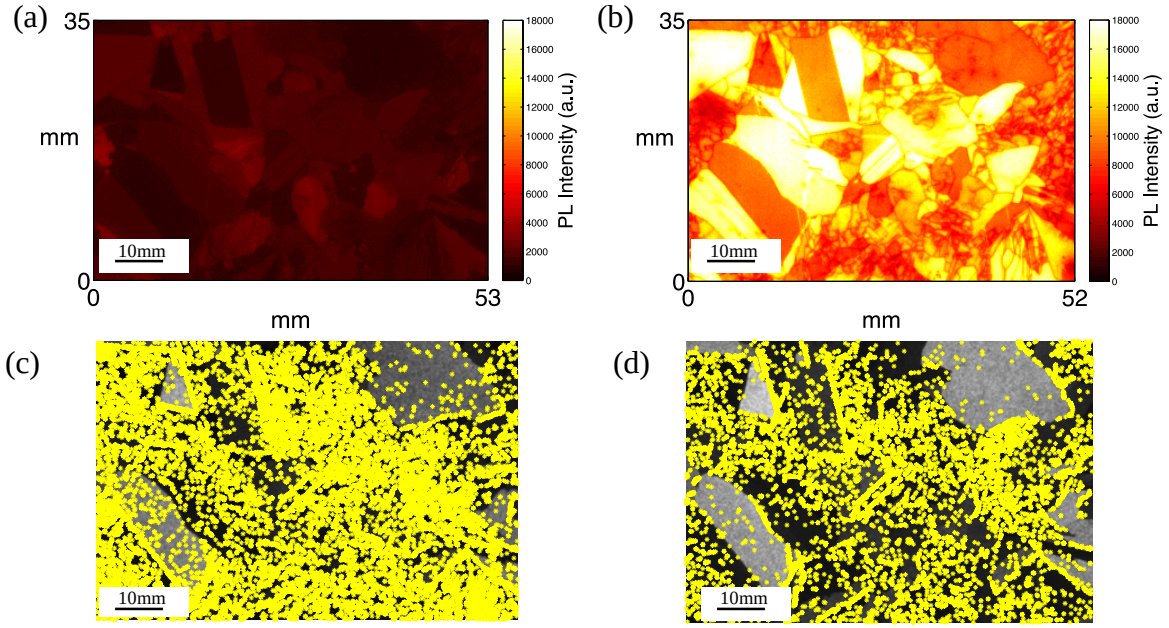

Figure 5.3: Large region of wafer exhibiting many grains: PL maps and τ_{max} before and after annealing. (a)-(d) all show the same center of wafer region exhibiting many grains. (a) shows the PL map for Wafer A, not annealed. (b) shows the PL map for Wafer A, annealed. (c) and (d) show a near-infrared transmission image with superimposed yellow data points showing locations of $\tau_{max} > 60$ MPa for Wafer A, for the not annealed, and annealed cases, respectively.

The color scales for the PL maps shown in Figure 5.3a and Figure 5.3b were chosen to provide greater contrast than the typical gray scale. The PL mapping results showed a significant increase in PL due to the HT anneal. This is evident from the drastic increase in lighter color regions in the wafer after annealing, which correlate with higher PL counts all over the 35 mm x 52 mm region. Figure 5.3c and Figure 5.3d show that there is a decrease in points with τ_{max} greater than 60 MPa as a result of annealing. The

threshold of 60 MPa was chosen based on the tail of the τ_{max} distribution (see Figure 5.4 and Figure 5.5) and the points of highest τ_{max}. The points of τ_{max} > 60 MPa decreased by approximately 50% after the HT anneal.

Figure 5.4 and Figure 5.5 show the distributions of τ_{max} as a function of percent wafer area selected for the pre-anneal and post-anneal steps.

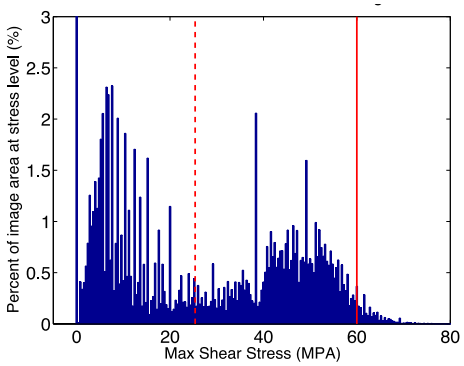

Figure 5.4: Pre-HT anneal: distribution of τ_{max} as a function of percent of image area. Red dotted line shows mean, solid line shows 60 MPa threshold.

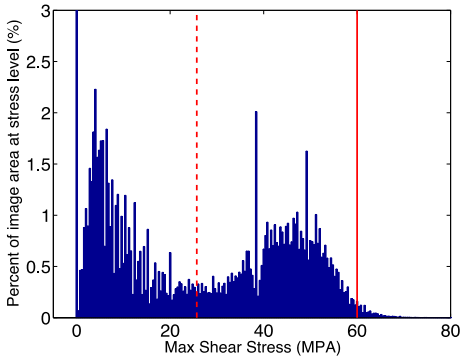

Figure 5.5: Post-HT anneal, distribution of τ_{max} as a function of percent of image area. Red dotted line shows mean, solid line shows 60 MPa threshold.

Although the number of points with τ_{max} greater than 60 MPa (the tail of the distribution) decreased, the average value of τ_{max} changed by less than 1 MPa. The statistical variance of the distributions was calculated before and after annealing and found to decrease by 6%. The decrease in variance suggests that the HT anneal likely caused a smoothing in the local stress variations.

Figure 5.6 shows the PL maps and the residual stress maps for a region in the wafer that demonstrated marked differences in residual stress prior to and after annealing.

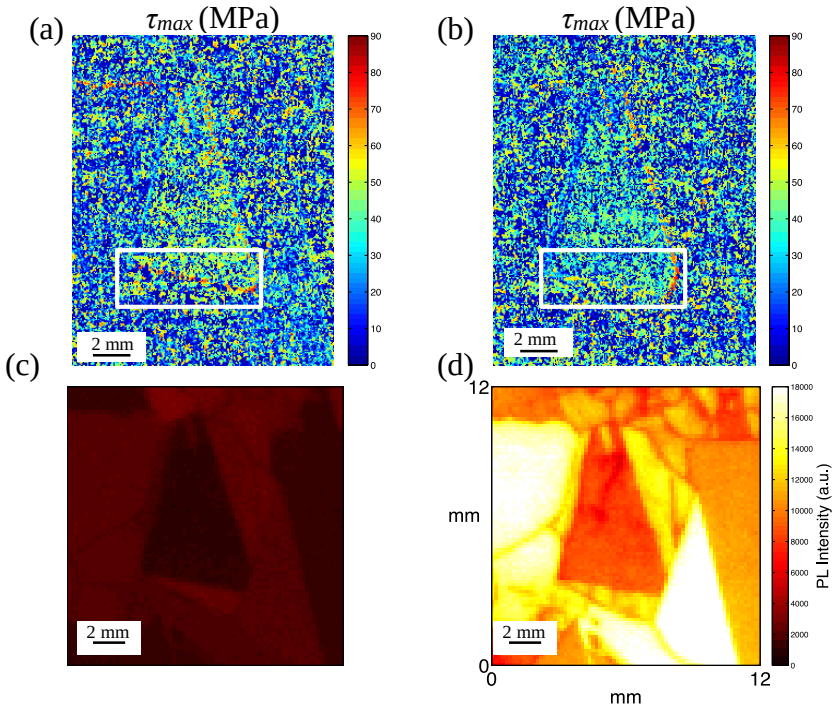

Figure 5.6: Triangular grain exhibiting marked differences in residual stress after HT anneal. (a)-(d) show the same triangular grain and surrounding region which is an approximately 12 mm x 12 mm area of Wafer A. (a) shows the τ_{max} map of the region before HT anneal, (b) shows τ_{max} after HT anneal, (c) shows PL map before HT anneal, and (d) shows PL map after HT anneal.

The white boxes Figure 5.6(a) and Figure 5.6b) highlight differences in grain boundary stresses after annealing. The τ_{max} residual stress maps showed that the very high grain boundary stresses (see white boxes in Figure 5.6a and Figure 5.6b) along the bottom of the central triangular grain decreased after annealing. Additionally, the mean of the τ_{max} stresses within the triangular shaped grain decreased. Prior to annealing, the mean τ_{max} within the triangular grain was 30.5 MPa. After annealing, the mean τ_{max} within the grain was 28 MPa. These calculations do not include the grain boundary stresses. Due to the fact that certain crystallographic planes are more prone to slip at higher temperatures

than others [86], it is likely that certain grains would exhibit a more marked change than others. As a result of prolonged elevated temperatures, the residual stress is likely to change in location and magnitude at some grain boundaries and not change at others.

5.3.1 Study of Two Cases: Grains and Grain Boundaries

Two sets of two grains, which will be referred to as “Case 1” and “Case 2”, and their respective grain boundaries were selected for polarized micro-Raman spectroscopy based residual stress measurement. Figure 5.7 shows a macrograph of the mc-Si sister wafer and the areas selected for Case 1 and Case 2.

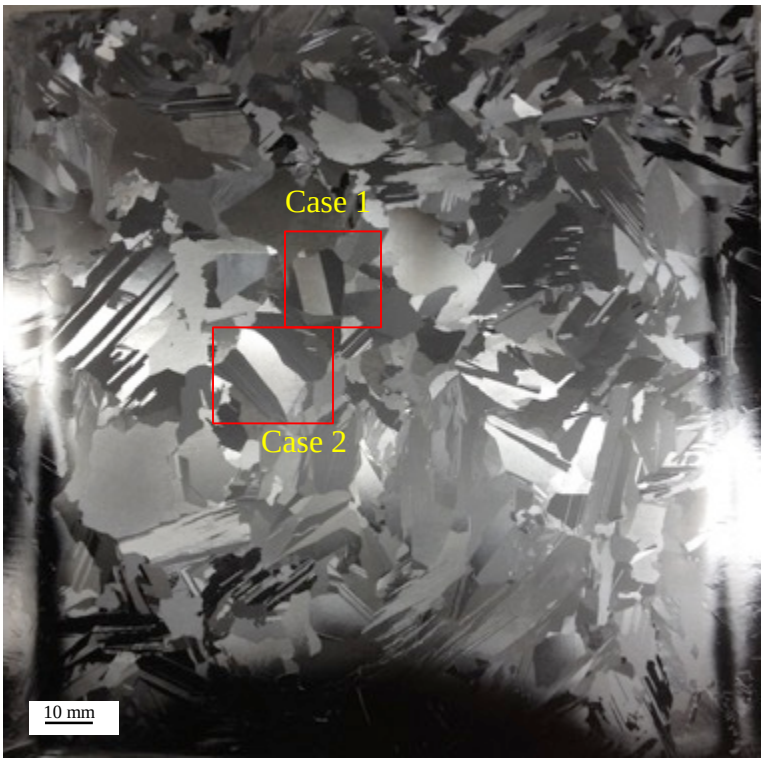

Figure 5.7: Macrograph of 156 mm x 156 mm mc-Si sister wafer. Boxes show “Case 1” and “Case 2” selections.

Figure 5.8 and Figure 5.9 show near-infrared transmission images for both Case 1 and Case 2 before and after annealing with locations of τ_{max} greater than 60 MPa superimposed on the images as yellow data points.

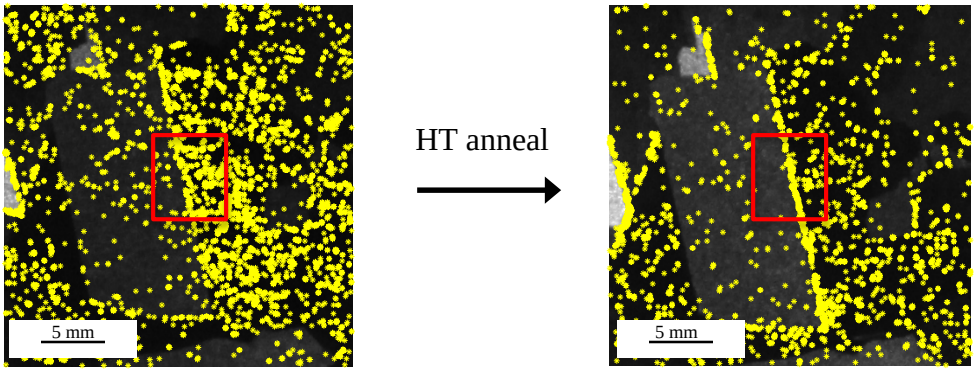

Figure 5.8: Case 1: Near-infrared transmission images of two grains and their respective grain boundaries with points exhibiting τ_{max} > 60 MPa superimposed on the images.

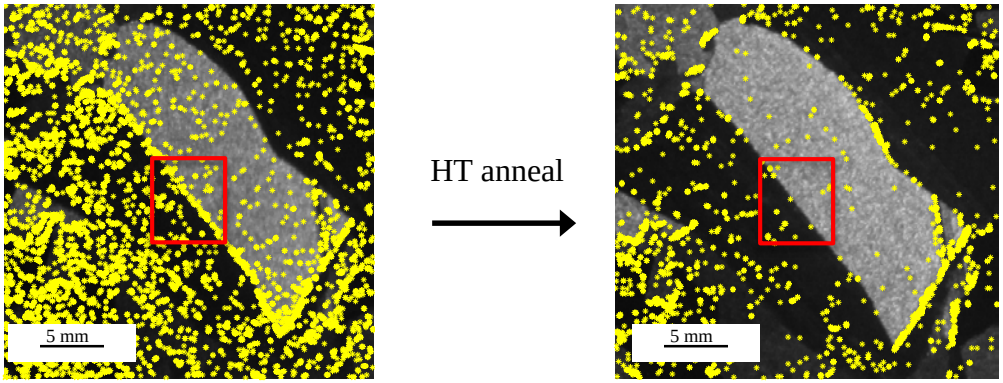

Figure 5.9: Case 2: near-infrared transmission images of two grains and their respective grain boundaries with points exhibiting τ_{max} > 60 MPa superimposed on the images.

The red boxes in Figure 5.8 and Figure 5.9 delineate the grain boundaries of interest in each case. In Case 1, the number of points with highest τ_{max} (>60 MPa) decreased in the grains but increased at the grain boundary after annealing. In Case 2, the number of points with highest τ_{max} (>60 MPa) decreased both in the grains and at the grain boundary after annealing.

For comparison, the polariscope was used to examine the mean τ_{max} both before and after annealing. The results are shown in Table 5.2 for Case 1 and Case 2.

Table 5.2: Mean τ_{max} for Case 1 and Case 2 at the center of the grains and at the grain boundaries.

		Mean τ_{max} Pre-anneal (MPa)	Mean τ_{max} Post-anneal (MPa)
 Case 1	Grain R	29	28
	Grain L	26	26
	Grain Boundary	35	37
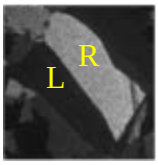 Case 2	Grain R	31	29
	Grain L	28	26
	Grain Boundary	32	31

The grains were labeled “R” and L” in the near-infrared transmission images shown in the the table for each case. The grain boundaries of interest were between the two “R” and “L” grains selected. The mean τ_{max} for all four grains remained more or less the same after HT annealing. In Case 1, the mean τ_{max} grain boundary stress increased by 2 MPa while the within grain τ_{max} decreased by 0-1 MPa. In Case 2, the mean τ_{max} grain boundary stress decreased by 1 MPa while the τ_{max} decreased by 2 MPa in the center of the grain. These results show a consistent trend in the reduction of within-the-grain stresses and the observation that certain grain boundaries exhibit an increase in τ_{max} while others exhibited a decrease in τ_{max}. A possible explanation for this behavior could be the 1100 °C HT annealing temperature used. Hartman et al. found large grain-to-grain variations in the dislocation density between temperatures of 1100-1700 °C [84]. They hypothesized that at these lower temperatures, which are closer to T_0=1000 °C, the characteristic temperature of Si [86], dislocation glide is favored in certain

crystallographic planes, which can explain the large grain-to-grain variation and the variation seen at grain boundaries.

Intuitively, it can be explained by the mechanism of dislocations moving along slip planes at elevated temperatures during annealing. It is well understood that the movement of dislocations along the same slip plane can be arrested at grain boundaries where they "stack up". In addition, there is a critical value of stress required to move dislocations across a grain boundary [87]. It is hypothesized that during annealing, certain slip planes caused dislocations to stack up and amplify the stress fields at certain grain boundaries while in other crystalline orientations and slip planes dislocations were annihilated or they moved away from the grain boundaries.

Previous studies often found a high influx of metal precipitates into the wafers during HT annealing [88], which led to a decrease in electrical performance by increasing the number of recombination centers. With the HT anneal procedure used in this thesis, the temperature hold at 600 °C during ramp-down likely allowed for the migration of precipitates back into dislocation regions and prevented a negative impact on the crystal lattice.

Micro-Raman spectroscopy was used to determine the stress state of the surfaces of the wafers before annealing. The results showed that both Case 1 and Case 2 were characterized by low tensile stresses in the range of 0-25 MPa in the center of the grains and at the grain boundaries. In Case 1, the average tensile stresses (σ_{xx} and σ_{yy}) after annealing increased by 13 MPa while in Case 2, the average tensile stresses (σ_{xx} and σ_{yy}) after annealing increased by 35 MPa. Table 5.3 shows the stress tensors measured for each Case 1 and Case 2.

Table 5.3: Stress tensors measured by polarized micro-Raman spectroscopy for each region of interest, pre-anneal, and post-anneal.

		Pre-Anneal Center of grain (MPa)	*Pre-Anneal* Grain boundary (MPa)	*Post-Anneal* Center of grain (MPa)	*Post-Anneal* Grain boundary (MPa)
 Case 1	Grain R	$\begin{bmatrix} 4 & -11 & 0 \\ -11 & 19 & 0 \\ 0 & 0 & 0 \end{bmatrix}$	$\begin{bmatrix} 7 & -3 & 0 \\ -3 & 2 & 0 \\ 0 & 0 & 0 \end{bmatrix}$	$\begin{bmatrix} 25 & 1 & 0 \\ 1 & 17 & 0 \\ 0 & 0 & 0 \end{bmatrix}$	$\begin{bmatrix} 28 & 11 & 0 \\ 11 & 22 & 0 \\ 0 & 0 & 0 \end{bmatrix}$
	Grain L	$\begin{bmatrix} 13 & 6 & 0 \\ 6 & 3 & 0 \\ 0 & 0 & 0 \end{bmatrix}$	$\begin{bmatrix} 12 & -7 & 0 \\ -7 & 9 & 0 \\ 0 & 0 & 0 \end{bmatrix}$	$\begin{bmatrix} 23 & -14 & 0 \\ -14 & 17 & 0 \\ 0 & 0 & 0 \end{bmatrix}$	$\begin{bmatrix} 12 & -9 & 0 \\ -9 & 29 & 0 \\ 0 & 0 & 0 \end{bmatrix}$
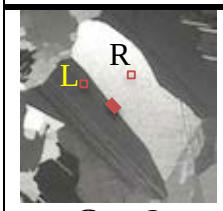 Case 2	Grain R	$\begin{bmatrix} 6 & 3 & 0 \\ 3 & 8 & 0 \\ 0 & 0 & 0 \end{bmatrix}$	$\begin{bmatrix} 12 & 2 & 0 \\ 2 & 5 & 0 \\ 0 & 0 & 0 \end{bmatrix}$	$\begin{bmatrix} 39 & 13 & 0 \\ 13 & 48 & 0 \\ 0 & 0 & 0 \end{bmatrix}$	$\begin{bmatrix} 42 & 14 & 0 \\ 14 & 49 & 0 \\ 0 & 0 & 0 \end{bmatrix}$
	Grain L	$\begin{bmatrix} 24 & 0 & 0 \\ 0 & 8 & 0 \\ 0 & 0 & 0 \end{bmatrix}$	$\begin{bmatrix} 13 & 0 & 0 \\ 0 & 15 & 0 \\ 0 & 0 & 0 \end{bmatrix}$	$\begin{bmatrix} 88 & -1 & 0 \\ -1 & 41 & 0 \\ 0 & 0 & 0 \end{bmatrix}$	$\begin{bmatrix} 48 & -1 & 0 \\ -1 & 18 & 0 \\ 0 & 0 & 0 \end{bmatrix}$

As stated in Chapter 4, the finding of primarily tensile stress in the Si wafers after removal of the saw damage layers is expected based on previous literature. In particular, the work of Oswald et al. [39] who modeled thermo-mechanically induced stresses in mc-Si ingots generated during casting, showed that the stress state in the center of an mc-Si ingot is tensile.

Gundel et al. proposed that tensile stress can be correlated to an increase in carrier mobility based on the piezo-resistivity of silicon [23]. Around precipitates, which act as recombination centers, tensile stress was hypothesized to hinder electrical performance by facilitating the movement of carriers to these sites. In the same manner, compressive stress was shown to exhibit the opposite effect. Based on the results of the current experiment, and the findings of Gundel et al. [23], it is hypothesized that the increase in

tensile stress of the component stresses, σ_{xx}, and σ_{yy}, at the surface of the mc-Si wafers shown Table 5.3, can be directly correlated to increase in carrier mobility at the surface, and thereby an increase in diffusion length at the surface of the wafer. This mechanism can serve to explain the improvement in PL, shown in Figure 5.10 for each, Case 1 and Case 2.

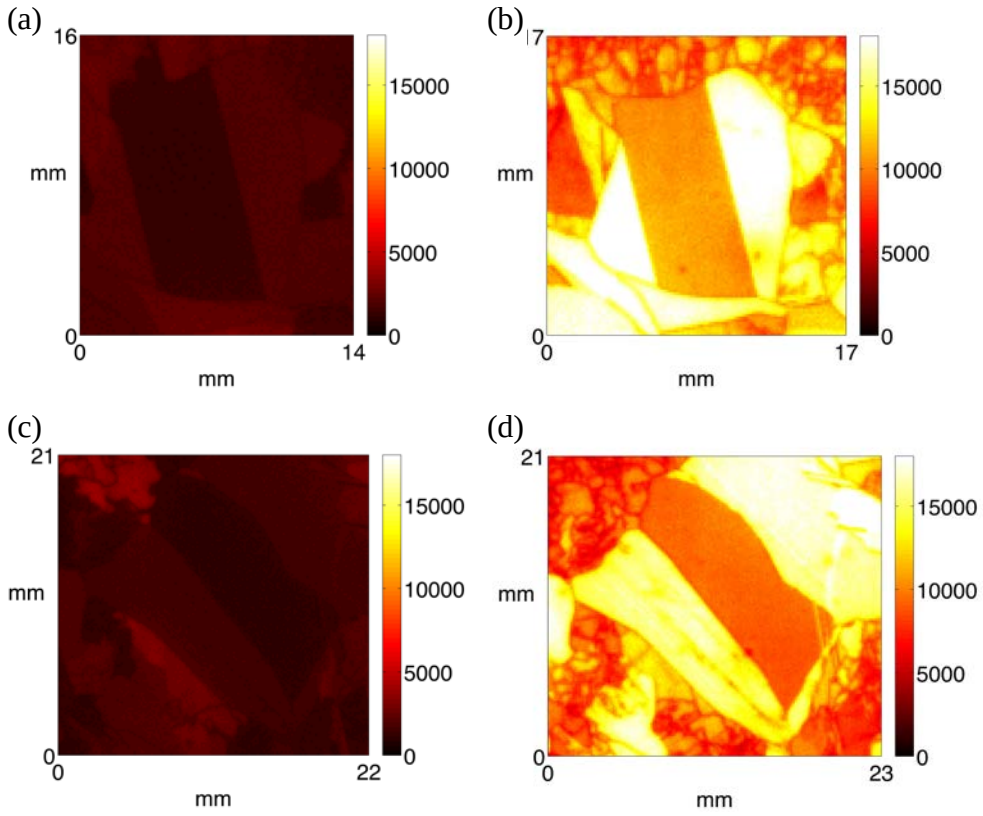

Figure 5.10: PL intensity (a.u.) maps of Case 1 and Case 2 regions, before and after HT annealing. (a) Case 1, before HT anneal. (b) Case 1, after anneal. (c) Case 2, before HT anneal. (d) Case 2, after anneal.

The improvement in PL was found to correlate with an increase in tensile stress at the surface of the region, measured by polarized micro-Raman spectroscopy.

5.4 Conclusions

The objective of the experiment described in this chapter was to understand the effect of residual stress on the electrical performance of mc-Si wafers. The experiment examined thermal gradient induced residual stress stemming from the solidification process of casting mc-Si ingots. The main conclusions are summarized below.

- A negative correlation was found between the τ_{max} residual stress and the electrical performance of mc-Si wafers.
    - HT annealing of the mc-Si wafers decreased the variance of τ_{max} and significantly decreased the number of points with highest τ_{max} (> 60 MPa) throughout the wafer, both at the grain boundaries and within the grains. Simultaneous to the decrease in variance of τ_{max}, the PL of the Si wafers significantly improved, leading to an increase in electrical performance of the Si wafer substrates.
- A positive correlation was found between *tensile* residual stress at the surface of the mc-Si wafer and an improvement in PL.
- Some grains exhibit a more marked decrease in τ_{max} than others when HT annealed at a temperature of 1100 °C.
- Mean within-the-grain τ_{max} residual stress either remained constant or decreased slightly as a result of the HT anneal while the mean grain boundary τ_{max} residual stress both increased and decreased depending on the grain boundary.
    - This behavior was explained by the mechanism of dislocations moving along slip planes at elevated temperatures during annealing [87]. It is hypothesized that during annealing, certain slip planes caused dislocations to stack up and increase the stress fields at certain grain boundaries while other crystalline orientations

and slip planes allowed for dislocations to be annihilated or move away from the grain boundaries.

- The HT anneal procedure caused a significant increase in PL.
    - Previous studies often found a high influx of metal precipitates into the wafers during HT annealing [88], which led to a decrease in electrical performance by increasing the number of recombination centers. With the HT anneal procedure used in this thesis, the temperature hold at 600 °C during ramp-down likely allowed for the migration of precipitates back into dislocation regions and prevented a negative impact on the crystal lattice. In addition, the specimen cleaning regimen used in the work decreased the number of impurities on the wafer surface, thereby minimizing the possibility of additional impurities migrating into the wafer at elevated temperatures.

In conclusion, the results of the experiment described in this chapter suggest that if variations and points of high τ_{max} stress can be reduced by either annealing at the ingot or the wafer level, the electrical efficiency of finished mc-Si solar cells can be potentially improved. The negative correlation between electrical performance and residual stress found using the results of this experiment was opposite to the positive correlation found by He [26]. Further investigation is needed to understand the opposing findings.

CHAPTER 6
CONCLUSIONS AND RECOMMENDATIONS

This chapter summarizes the main contributions and conclusions of this thesis, and suggests related areas for further investigation.

6.1 Main Contributions

The main contributions of this thesis can be summarized as follows:

- Fundamental understanding of the nature, magnitudes, and spatial distribution of residual stress induced by individual crystalline Si wafer manufacturing processes, namely Diamond Wire Sawing (DWS), Loose Abrasive Wire Sawing (LAWS), and thermal gradients produced during casting and solidification.
- Comparison of residual stress measurements made by the two complementary residual stress measurement techniques of polarized micro-Raman spectroscopy and near-infrared birefringence polariscopy.
- Increased understanding of the relationship between residual stress induced in mc-Si wafers during solidification of the ingot and electrical performance of mc-Si wafers.

6.2 Conclusions

The main conclusions of this thesis may be summarized as follows:

Residual Stress due to Wire Sawing:

1. Both Diamond Wire Sawing (DWS) and Loose Abrasive Slurry Wire Sawing (LAWS) produce compressive residual stresses (σ_{xx} and σ_{yy}) in the as-cut mc-Si wafer surface. LAWS produces larger compressive stresses in the as-cut surface layers than DWS. The surface residual stresses (σ_{xx} and σ_{yy}) in the LAWS and DWS wafers examined ranged from -50 MPa to -110 MPa and from -18 MPa to -80 MPa, respectively.

2. DWS produces high through-thickness residual maximum shear stresses, τ_{max}, (>25 MPa) that are spatially aligned with wire striations. LAWS produces high τ_{max} stresses (>25 MPa) that are randomly distributed, with no directional preference.

3. With increasing etch depth, the residual stresses (σ_{xx} and σ_{yy}) in the DWS and LAWS wafers transition from compressive to tensile. Based on the etching results, the depth of residual stress due to LAWS is estimated to be between 25 to 40 μm while that due to DWS is estimated to be between 16 and 25 μm.

4. The mean through-thickness τ_{max} of individual grains in mc-Si wafers produced by DWS does not change with the grain orientation. In contrast, the mean through-thickness τ_{max} produced by LAWS does change with grain orientation.

5. DWS produces high and low distinctive mean through-thickness τ_{max} stresses along the grain boundaries compared to within the grains. In contrast, LAWS does not produce distinctive τ_{max} stress fields along the grain boundaries.

Residual Stress due to Solidification:

6. After 40 μm of saw damage removal through etching, the surface residual stresses (σ_{xx} and σ_{yy}) due to thermal gradients present during solidification/casting, are much less compressive (and mostly tensile) than the surface stresses in the as-cut surfaces of the wafers. After saw damage removal, the DWS wafer yielded tensile residual stresses (σ_{xx} and σ_{yy}) in the 0-30 MPa range while the LAWS wafer yielded stresses in the -15 MPa to 10 MPa range.

7. The casting and solidification induced residual stresses tend to accumulate at the grain boundaries in mc-Si wafers. With progressive etching, the through-thickness residual maximum shear stress, τ_{max}, are concentrated in the grain boundary regions of DWS and LAWS wafers.

8. There are no significant differences in the surface residual stress states or the surface residual stress magnitudes (σ_{xx} and σ_{yy}) between the inside of a mc-Si grain and the grain boundary.

Polarized Micro-Raman Spectroscopy versus NIR Birefringence Polariscopy:

9. While the two residual stress measurement techniques cannot be compared directly (due to one being a surface probing technique and the other being a through-thickness technique), the results of this study confirm that, on an order of magnitude basis, the two methods yield similar values of the maximum shear stress, τ_{max}, when probing the same region of a wafer.

10. The polarized micro-Raman technique is well-suited to measure the individual components of the residual stress, including their states and magnitudes, generated by wire sawing in the surface layers of crystalline Si wafers. The NIR birefringence polariscopy method is well-suited to measure the full-field distribution of the maximum residual shear stress due to casting and solidification.

Residual Stress and Electrical Performance:

11. There exists an inverse relationship between the maximum residual shear stress due to casting/solidification and the electrical performance of mc-Si wafers.
    - HT annealing of mc-Si wafers decreased the variance of τ_{max} and significantly decreased the number of points of highest τ_{max} (> 60 MPa) throughout the wafer, both at the grain boundaries and within the grains. Simultaneous to the decrease in τ_{max}, the photoluminescence (PL) of the Si wafers improved significantly throughout the wafer, demonstrating an increase in the electrical performance of the Si wafer substrates.

6.3 Recommendations for Future Work

Related areas for further research include the following:

- Based on the finding of a positive correlation between tensile stress at the surface of mc-Si wafer after annealing and improvement in PL, further work could be conducted to understand the effect of tensile stress on surface recombination velocity and the effect of tensile stress in the bulk of the wafer. Based on the findings of this thesis, it is hypothesized that improvements in tensile stress in the bulk could increase diffusion length, and thereby improve lifetime of mc-Si wafers.
- The work of this thesis examined residual stress primarily in the center of the mc-Si wafers. As fracture is likely to initiate along the edges of a wafer [34], similar procedures used in this thesis could be used to investigate the stress type at the edges of mc-Si wafers, which could provide knowledge regarding the sources of wafer fracture.
- The residual stress measurement procedures used in this thesis could be extended to mono-Si wafers produced by both DWS and LAWS to eliminate the effect of grain boundaries and to understand the residual stress in mono-Si wafers.
- The results of this thesis suggest that the interaction of fixed abrasive grits in DWS with different crystallographic grain boundary angles produce high and low residual stress fields compared to the within-the-grain stresses. The effect of the fixed abrasive DWS wire direction on small and large angle crystallographic grain boundaries could be investigated further.

APPENDIX A
EQUATIONS AND MATERIAL CONSTANTS

Equation for the transformation matrix, **T**(α, β, γ):

$$\mathbf{T}(\alpha,\beta,\gamma) = \begin{bmatrix} \cos\alpha\cos\gamma - \cos\beta\sin\gamma\sin\alpha & -\cos\alpha\sin\gamma - \cos\beta\cos\gamma\sin\alpha & \sin\beta\sin\alpha \\ \sin\alpha\cos\gamma + \cos\beta\sin\gamma\cos\alpha & -\sin\alpha\sin\gamma + \cos\beta\cos\gamma\cos\alpha & -\sin\beta\cos\alpha \\ \sin\gamma\sin\beta & \cos\gamma\sin\beta & \cos\beta \end{bmatrix}$$

Phonon deformation potentials material constants for silicon [89]:

p/ω_0^2 = -1.85 ± 0.06

q/ω_0^2 = -2.31± 0.06

r/ω_0^2 = -0.71± 0.02

where ω_0 = 521 cm^{-1}

Stiffness matrix constants [90] :

S_{12} = -2.134 × 10^{-12} Pa^{-1}

S_{11} = 7.67 × 10^{-12} Pa^{-1}

S_{22} = 12.5 × 10^{-12} Pa^{-1}

REFERENCES

[1] G. Cellere, H. Forstner, T. Falcon, Martijn Zwegers, J. Bernreuter, G. Xing, *et al.* (2015). *International Technology Roadmap for Photovoltaic (7th ed.).* Available: http://www.itrpv.net

[2] J. F. Nijs, J. Szlufcik, J. Poortmans, S. Sivoththaman, and R. P. Mertens, "Advanced manufacturing concepts for crystalline silicon solar cells," *IEEE Transactions on Electron Devices,* vol. 46, pp. 1948-1969, 1999.

[3] H. J. Möller, C. Funke, M. Rinio, and S. Scholz, "Multicrystalline silicon for solar cells," *Thin Solid Films,* vol. 487, pp. 179-187, 2005.

[4] (1994, Nov 17). *Silicon Wafer Fabrication Process*. Available: http://www.cleanroom.byu.edu/EW_formation.phtml

[5] (2010, Nov. 18). *Products*. Available: http://www.vacsol.com/en/products/

[6] A. Schönecker, L. J. Geerligs, and A. Müller, "Casting technologies for solar silicon wafers: block casting and ribbon-growth-on-substrate," *Solid State Phenomena,* vol. 95-96, pp. 149-158, 2004.

[7] K. Yoo, S. Johnson, and W. Regnault, "Lattice defects within grain volumes that affect the electrical quality of cast polycrystalline silicon solar-cell materials," *Journal of Applied Physics,* vol. 57, pp. 2258-2266, 1985.

[8] K. Skenes, "Characterization of residual stresses in birefringent materials applied to multicrystalline silicon wafers," Ph.D. Dissertation, Mechanical Engineering, Georgia Institute of Technology, Georgia Institute of Technology, 2014.

[9] W. S. Radeker and S. W. Cunningham, "A hierarchy of slurry reprocessing options," in *The Minerals, Metals & Materials Society (TMS) 139th Annual Meeting & Exhibition.*, Seattle, WA., 2010.

[10] Hali Forstner, S. Bandil, M. Zwegers, R. Bollen, Gianluca Coletti, Wim Sinke, *et al.* (2014). *International Technology Roadmap for Photovoltaic Results (ITRPV) (5th ed.)*. Available: http://www.itrpv.net/

[11] K. Tomono, S. Miyamoto, T. Ogawa, H. Furuya, Y. Okamura, M. Yoshimoto, *et al.*, "Recycling of kerf loss silicon derived from diamond-wire saw cutting process by chemical approach," *Separation and Purification Technology,* vol. 120, pp. 304-309, 2013.

[12] Y. Kondo, N. Watanabe, D. Ide, T. Matsuki, H. Takato, and I. Sakata, "Characterization of multicrystalline silicon wafers for solar cell applications

sliced with a fixed abrasive wire," in *23rd European Photovoltaic Solar Energy Conference and Exhibition*, Valencia, Spain, 2008, pp. 1297-1301.

[13] N. Watanabe, Y. Kondo, D. Ide, T. Matsuki, H. Takato, and I. Sakata, "Characterization of polycrystalline silicon wafers for solar cells sliced with novel fixed-abrasive wire," *Progress in Photovoltaics: Research and Applications,* vol. 18, pp. 485-490, 2010.

[14] F. Ferrazza, "Crystalline silicon: manufacture and properties," in *Solar Cells*, A. McEvoy, T. Markvart, and L. Casteñer, Eds., 2nd ed Oxford: Elsevier Science Ltd., 2013, pp. 69-86.

[15] A. Goetzberger, *Crystalline silicon solar cells*. Chichester New York: Wiley, 1998.

[16] Y. F. Kudryavtsev, "Residual Stress," in *Springer Handbook of Experimental Solid Mechanics*, J. Sharpe and N. William, Eds., ed Boston, MA: Springer US, 2008, pp. 371-388.

[17] J. W. Huang, W. S. Hwang, C. H. Hwang, and Y. W. Chang, "Residual thermal stresses simulation for multi-crystalline silicon casting," *IOP Conference Series: Materials Science and Engineering,* vol. 33, p. 012059, 2012.

[18] D. Echizenya, H. Sakamoto, and K. Sasaki, "Effect of mechanical surface damage on silicon wafer strength," *Procedia Engineering,* vol. 10, pp. 1440-1445, 2011.

[19] C. Funke, E. Kullig, M. Kuna, and H. Moller, "Biaxial fracture test of silicon wafers," *Advanced Engineering Materials,* vol. 6, pp. 594-598, 2004.

[20] V. A. Popovich, A. Yunus, M. Janssen, I. J. Bennett, and I. M. Richardson, "Effect of microstructure and processing parameters on mechanical strength of multicrystalline silicon solar cells," presented at the Photovoltaic Specialists Conference (PVSC), 2010 35th IEEE, Honolulu, HI, 2010.

[21] C. Yang, H. Wu, S. Melkote, and S. Danyluk, "Comparative analysis of fracture strength of slurry and diamond wire sawn multicrystalline silicon solar wafers," *Advanced Engineering Materials,* vol. 15, pp. 358-365, 2013.

[22] J. Chen, B. Chen, T. Sekiguchi, M. Fukuzawa, and M. Yamada, "Correlation between residual strain and electrically active grain boundaries in multicrystalline silicon," *Applied Physics Letters,* vol. 93, p. 112105, 2008.

[23] P. Gundel, M. C. Schubert, D. H. Friedemann, K. Wolfram, W. Wilhelm, M. C. Gema, *et al.*, "Impact of stress on the recombination at metal precipitates in silicon," *Journal of Applied Physics,* vol. 108, p. 103707, 2010.

[24] G. Sarau, M. Becker, S. Christiansen, M. Holla, and W. Seifert, "Micro-Raman mapping of residual stresses at grain boundaries in multicrystalline block cast silicon solar cell material: their relation to the grain boundary microstructure and recombination activity," presented at the 24th European Photovoltaic Solar Energy Conference, Hamburg, Germany, 2009.

[25] G. Sarau, S. Christiansen, M. Holla, and W. Seifert, "Correlating internal stresses, electrical activity and defect structure on the micrometer scale in EFG silicon ribbons," *Solar Energy Materials and Solar Cells,* vol. 95, pp. 2264-2271, 2011.

[26] S. He, "Near infrared photoelasticity of polycrystalline silicon and it's relation to in-plane residual stresses," Ph.D. Dissertation, Mech. Eng., Georgia Inst. of Techn., 2005.

[27] B. Meinel, T. Koschwitz, and J. Acker, "Textural development of SiC and diamond wire sawed sc-silicon wafer," *Energy Procedia,* vol. 27, pp. 330-336, 2012.

[28] M. Becker, H. Scheel, S. Christiansen, and H. P. Strunk, "Grain orientation, texture, and internal stress optically evaluated by micro-Raman spectroscopy," *Journal of Applied Physics,* vol. 101, p. 063531, 2007.

[29] X. F. Brun and S. N. Melkote, "Analysis of stresses and breakage of crystalline silicon wafers during handling and transport," *Solar Energy Materials and Solar Cells,* vol. 93, pp. 1238-1247, 2009.

[30] R. Buchwald, K. Fröhlich, S. Würzner, T. Lehmann, K. Sunder, and H. J. Möller, "Analysis of the sub-surface damage of mc- and cz-Si wafers sawn with diamond-plated wire," *Energy Procedia,* vol. 38, pp. 901-909, 2013.

[31] C. Funke, S. Wolf, and D. Stoyan, "Modeling the tensile strength and crack length of wire-sawn silicon wafers," *Journal of Solar Energy Engineering,* vol. 131, p. 011012, 2009.

[32] P. Rupnowski and B. Sopori, "Strength of Si wafers with microcracks: a theoretical model," presented at the 33rd IEEE Photovoltaic Specialists Conference, San Diego, CA, 2008.

[33] P. Rupnowski and B. Sopori, "Strength of silicon wafers: fracture mechanics approach," *International Journal of Fracture,* vol. 155, pp. 67-74, 2009.

[34] H. Wu, S. N. Melkote, and S. Danyluk, "Mechanical strength of silicon wafers cut by loose abrasive slurry and fixed abrasive diamond wire sawing," *Advanced Engineering Materials,* vol. 14, pp. 342-348, 2012.

[35] A. Bidiville, K. Wasmer, J. Michler, P. M. Nasch, M. Van Der Meer, and C. Ballif, "Mechanisms of wafer sawing and impact on wafer properties," *Progress in Photovoltaics: Research and Applications,* vol. 18, pp. 563-572, 2010.

[36] V.A. Popovich, J.M. Westra, Van Swaaij, M. Janssen, I.J. Bennett, and I. M. Richardson, "Raman spectroscopy characterization of residual stress in multicrystalline silicon solar wafers and solar cells; relation to microstructure, defects, and processing conditions," presented at the 37th IEEE Photovoltaic Specialists Conference, PVSC, Seattle, WA, 2011.

[37] S. Wurzner, R. Buchwald, S. Retsch, and H. Moller, "Investigation of the development of the microcrack structure in scratch tests with single diamond particles on monocrystalline silicon wafers," in *29th European Photovoltaic Solar Energy Conference and Exhibition*, 2013.

[38] C. Yang, F. Mess, K. Skenes, S. Melkote, and S. Danyluk, "On the residual stress and fracture strength of crystalline silicon wafers," *Applied Physics Letters,* vol. 102, p. 021909, 2013.

[39] M. Oswald, M. Turek, and J. Bagdahn, "Numerical simulations of thermo-mechanical stresses during the casting of multi-crystalline silicon ingots," in *11th International Conference on Thermal, Mechanical & Multi-Physics Simulation, and Experiments in Microelectronics and Microsystems (EuroSimE)*, Bordeaux, France, 2010.

[40] M. M'Hamdi, S. Gouttebroze, and H. G. Fjær, "3D modelling of stresses and deformations during crystallisation of silicon accounting for ingot-crucible interactions," *Journal of Crystal Growth,* vol. 362, pp. 83-87, 2013.

[41] G. Sarau, S. Christiansen, M. Holla, and W. Seifert, "The effect of internal stresses on the recombination activity of structural defects in mc-Si," presented at the Photovoltaic Specialists Conference (PVSC), 2011 37th IEEE, Seattle, WA, 2011.

[42] W. Rindner, "Resistance of elastically deformed shallow p-n junctions," *Journal of Applied Physics,* vol. 33, pp. 2479-2480, 1962.

[43] I. Goroff and L. Kleinman, "Deformation potentials in silicon. III. Effects of a general strain on conduction and valence levels," *Physical Review,* vol. 132, pp. 1080-1084, 1963.

[44] J. J. Wortman, J. R. Hauser, and R. M. Burger, "Effect of mechanical stress on p-n junction device characteristics," *Journal of Applied Physics,* vol. 35, pp. 2122-2131, 1964.

[45] *Solar cells materials, manufacture and operation*, 2nd ed. Amsterdam: Elsevier, Ltd., 2013.

[46] W. Paul and D. M. Warschauer, "Optical properties of semiconductors under hydrostatic pressure—II. Silicon," *Journal of Physics and Chemistry of Solids,* vol. 5, pp. 102-106, 1958.

[47] G. Sarau, A. Bochmann, R. Lewandowska, and S. Christiansen, "From micro– to macro–raman spectroscopy: solar silicon for a case study," in *Advanced Aspects of Spectroscopy*, D. M. a. Farrukh, Ed., ed, 2012.

[48] K. Ramesh, *Digital photoelasticity: advanced techniques and applications*. Berlin, Germany: Springer-Verlag, 2000.

[49] F. W. Sears, *University physics*, 2nd ed. Addison-Wesley: Cambridge, MA, 1955.

[50] F. Li, "Study of stress measurement using polariscope," Ph.D. Dissertation, Mech. Eng., Georgia Inst. of Techn., 2010.

[51] D. Brewster, "On the communication of the structure of doubly refracting crystals to glass, muriate of soda, fluor spar, and other substances, by mechanical compression and dilatation," *Philosophical Transactions of the Royal Society of London,* vol. 106, pp. 156-178, 1816.

[52] E. G. Coker, *A treatise on photoelasticity*, 2nd ed. Cambridge University Press: Cambridge, U.K., 1957.

[53] J. W. Dally, *Experimental stress analysis*, 4th ed. Knoxville, TN: College House Enterprises, 2005.

[54] J. Case, L. Chilver, and C. T. F. Ross, *Strength of materials and structures*, 4th ed. Oxford, U.K.: Butterworth-Heinemann, 1999.

[55] R. G. R. Prasath, K. Skenes, and S. Danyluk, "Comparison of phase shifting techniques for measuring in-plane residual stress in thin, flat silicon wafers," *Journal of Electronic Materials,* vol. 42, pp. 2478-2485, 2013.

[56] T. Zheng and S. Danyluk, "Study of stresses in thin silicon wafers with near-infrared phase stepping photoelasticity," *Journal of Materials Research,* vol. 17, pp. 36-42, 2002.

[57] T. Zheng and S. Danyluk, "Determination of stresses in thin silicon plates with near-infrared phase stepping photoelasticity," in *Proceedings of the 7th ASME NDE Tropical Conference*, San Antonio, TX, 2001, pp. 195-199.

[58] S. Danyluk and S. Ostapenko, "Full field birefringence measurement of grown-in stresses in thin silicon sheet," National Renewable Energy Laboratory, Golden, Co. NREL/SR-520-44237, November 2008.

[59] S. He, T. Zheng, and S. Danyluk, "Analysis and determination of the stress-optic coefficients of thin single crystal silicon samples," *Journal of Applied Physics*, vol. 96, pp. 3103-3109, 2004.

[60] K. Skenes, F. Li, and S. Danyluk, "Analysis of residual stress in thin silicon wafers with an NIR polariscope," in *Proceedings of the 26th European Photovoltaic Solar Energy Conference and Exhibition*, Hamburg, Germany, 2011.

[61] K. Skenes, R. G. R. Prasath, and S. Danyluk, "Polariscopy measurement of residual stress in thin silicon wafers," in *Conference Proceedings of the Society for Experimental Mechanics Series*, Lombard, IL., 2014, pp. 79-85.

[62] F. W. Hecker and B. Morche, "Computer-aided measurement of relative retardations in plane photoelasticity," in *Proceedings of the VIIIth International Conference on Experimental Stress Analysis*, Amsterdam, Netherlands, 1986, pp. 535-542.

[63] I. De Wolf, "Micro-Raman spectroscopy to study local mechanical stress in silicon integrated circuits," *Semiconductor Science and Technology*, vol. 11, pp. 139-154, 1996.

[64] M. Fukuzawa, R. Kashiwagi, and M. Yamada, "Computational imaging of defects in commercial substrates for electronic and photonic devices," in *Proc. SPIE 8296, Computational Imaging X*, Burlingame, CA, 2012, pp. 829616-1-829616-7.

[65] W. Hayes, *Scattering of light by crystals*. Wiley New York, NY., 1978.

[66] R. Loudon, "The Raman effect in crystals," *Advances in Physics*, vol. 13, pp. 423-482, 1964.

[67] M. A. Green and M. J. Keevers, "Optical properties of intrinsic silicon at 300 K," *Progress in Photovoltaics: Research and Applications*, vol. 3, pp. 189-192, 1995.

[68] J. B. Hopkins and L. A. Farrow, "Raman microprobe determination of local crystal orientation," *Journal of Applied Physics*, vol. 59, pp. 1103-1110, 1986.

[69] O. Engler, *Introduction to texture analysis macrotexture, microtexture, and orientation mapping*, 2nd ed. Hoboken, NJ.: Taylor and Francis, 2009.

[70] S. Ganesan, A. A. Maradudin, and J. Oitmaa, "A lattice theory of morphic effects in crystals of the diamond structure," *Annals of Physics*, vol. 56, pp. 556-594, 1970.

[71] R. W. D. Nickalls, "Viete, Descartes and the cubic equation," *The Mathematical Gazette,* vol. 90, pp. 203-208, 2006.

[72] M. J. Madou, *Fundamentals of microfabrication*. CRC Press: Boca Raton, FL., 1997.

[73] M. A. Hopcroft, W. D. Nix, and T. W. Kenny, "What is the young's modulus of silicon?," *Journal of Microelectromechanical Systems,* vol. 19, pp. 229-238, 2010.

[74] H. P. Zappe, *Fundamentals of micro-optics*. Cambridge, U.K.: Cambridge University Press, 2010.

[75] K. E. Bean, "Anisotropic etching of silicon," *IEEE Trans. Electron Devices* vol. 25, pp. 1185-1193, 1978.

[76] *CRC materials science and engineering handbook,* 3rd ed. Boca Raton, FL: CRC Press, 2000.

[77] B. Meinel, T. Koschwitz, R. Heinemann, and J. Acker, "The texturization process during horizontal acidic etching of multi-crystalline silicon wafers," *Materials Science in Semiconductor Processing,* vol. 26, pp. 695-703, 2014.

[78] J. M. Gere and B. J. Goodno, *Mechanics of materials*, 7th ed. United States: CL Engineering, 2008.

[79] W. Chen, X. Liu, M. Li, C. Yin, and L. Zhou, "On the nature and removal of saw marks on diamond wire sawn multicrystalline silicon wafers," *Materials Science in Semiconductor Processing,* vol. 27, pp. 220-227, 2014.

[80] J. Chu and A. Sher, *Device physics of narrow gap semiconductors*. New York, New York: Springer, 2009.

[81] T. Trupke, R. A. Bardos, M. C. Schubert, and W. Warta, "Photoluminescence imaging of silicon wafers," *Applied Physics Letters,* vol. 89, p. 044107, 2006.

[82] J. Haunschild, M. Glatthaar, M. Demant, J. Nievendick, M. Motzko, S. Rein, *et al.*, "Quality control of as-cut multicrystalline silicon wafers using photoluminescence imaging for solar cell production," *Solar Energy Materials and Solar Cells,* vol. 94, pp. 2007-2012, 2010.

[83] J. Tan, D. Macdonald, N. Bennett, D. Kong, A. Cuevas, and I. Romijn, "Dissolution of metal precipitates in multicrystalline silicon during annealing and the protective effect of phosphorus emitters," *Applied Physics Letters,* vol. 91, p. 043505, 2007.

[84] K. Hartman, M. Bertoni, J. Serdy, and T. Buonassisi, "Dislocation density reduction in multicrystalline silicon solar cell material by high temperature annealing," *Applied Physics Letters,* vol. 93, p. 122108, 2008.

[85] S. G. Roberts, A. S. Booth, and P. B. Hirsch, "Dislocation activity and brittle-ductile transitions in single crystals," *Materials Science and Engineering: A,* vol. 176, pp. 91-98, 1994.

[86] S. Takeuchi and A. Argon, "Steady-state creep of single-phase crystalline matter at high temperature," *Journal of Materials Science,* vol. 11, pp. 1542-1566, 1976.

[87] J.-S. Zhang, *High temperature deformation and fracture of materials*. Oxford, U.K.: Woodhead Publishing Limited, 2010.

[88] M. Pagani, R. J. Falster, G. R. Fisher, G. C. Ferrero, and M. Olmo, "Spatial variations in oxygen precipitation in silicon after high temperature rapid thermal annealing," *Applied Physics Letters,* vol. 70, pp. 1572-1574, 1997.

[89] E. Anastassakis and M. Cardona, "Phonons, strains, and pressure in semiconductors," in *Semiconductors and Semimetals*. vol. 55, ed, 1998, pp. 117-233.

[90] W. A. Brantley, "Calculated elastic constants for stress problems associated with semiconductor devices," *Journal of Applied Physics,* vol. 44, p. 534, 1973.